

DEPARTMENT OF PHYSICS, UNIVERSITY OF JYVÄSKYLÄ
RESEARCH REPORT No. ??/2019

**JET TRANSVERSE MOMENTUM DISTRIBUTIONS
FROM RECONSTRUCTED JETS
IN P+PB COLLISIONS AT $\sqrt{s_{\text{NN}}} = 5.02 \text{ TeV}$**

**BY
TOMAS SNELLMAN**

Academic Dissertation
for the Degree of
Doctor of Philosophy

Jyväskylä, Finland
June 2019

Author	Tomas Snellman University of Jyväskylä Finland
Supervisors	Dr. Kim Dong Jo University of Jyväskylä Finland
	Prof. Jan Rak University of Jyväskylä Finland
Reviewers	Prof. Stefan Bathe Baruch College, CUNY USA
	Prof. Marcin Chrząszcz Instytut Fizyki Jądrowej PAN Poland
Opponent	Prof. Jamie Nagle University of Colorado Boulder USA

*Acknowledgements

Contents

1	Introduction	3
1.1	Quantum chromodynamics	5
1.1.1	Foundation of QCD	5
1.1.2	Asymptotic Freedom	8
1.2	Heavy-ion physics	10
1.2.1	History	11
1.3	Features of Heavy-Ion Collisions	12
1.3.1	Collision Geometry	12
1.3.2	Collective motion	16
1.4	Hard processes	23
1.4.1	pQCD factorization	23
1.4.2	Jet showering	25
1.4.3	Soft gluon radiation and angular ordering	26
1.4.4	Jet hadronisation	28
1.4.5	Interactions between jet and medium	32
1.4.6	New paradigm of jet Quenching	36
1.5	QGP in Small systems	41
1.5.1	Collective phenomena	41
1.5.2	Absence of jet quenching	42
1.5.3	Centrality determination in small systems	45
2	Experimental Setup	48
2.1	CERN	48
2.2	Large Hadron Collider	49
2.2.1	LHC experiments	50
2.3	ALICE	51
2.3.1	Tracking	52
2.3.2	TPC	54
2.3.3	Particle identification	55
2.3.4	Electromagnetic Calorimeter	56
2.3.5	Forward and trigger detectors	57
2.3.6	Muon spectrometer	59
2.3.7	Triggers	59
2.4	TPC upgrade	61
2.4.1	ALICE upgrade during LS2	61
2.4.2	TPC upgrade	61

3	Event and track selection	65
3.1	Event selection	65
3.2	Track reconstruction	65
3.3	Cluster selection	69
4	Analysis method	71
4.1	Jet Finding	71
4.1.1	Anti k_T algorithm	71
4.2	Definition of j_T	72
4.3	Unfolding detector effects	74
4.3.1	Bayesian unfolding	75
4.3.2	Toy Monte Carlo	77
4.3.3	Pythia Response matrices	78
4.3.4	Unfolding closure test	79
4.4	Background	82
4.4.1	Perpendicular cone background	82
4.4.2	Random background	84
4.5	Fitting	85
5	Systematic errors	87
5.1	Background	87
5.2	Unfolding	87
5.2.1	Effect of number of iterations	88
5.2.2	Effect of different prior	88
5.2.3	Effect of p_T truncation	88
5.3	Tracking	91
5.4	EMCal clusters	92
5.5	Summary of systematic uncertainties	94
6	Results	95
6.1	High multiplicity events	97
7	Discussion	99
7.1	Comparing dihadron and jet j_T results	99
7.1.1	Different R parameters	100
7.1.2	Leading tracks versus jet	101
8	Summary	104

1 Introduction

This thesis focuses on studying Quantum Chromodynamics (QCD) [1], a part of the standard model of particle physics [2], which is the theory describing the strong interactions. Strong interaction is the force responsible for interactions that holds the nucleus of an atom together. Fundamentally it describes the interactions between quarks and gluons, the elementary constituents of the building blocks of the nucleus, protons and neutrons. Because of specifics of this interaction quarks and gluons, together dubbed partons, can never be seen free [3]. Under ordinary conditions they are confined into bound states called hadrons. In extreme conditions they can form a medium of asymptotically free quarks and gluons, quark-gluon plasma (QGP) [4].

Indirectly quarks can be seen in high energy particle collisions as jets, collimated streams of particles observed in high energy particle collisions [5]. The physics of these jets is the primary topic discussed in this thesis. Understanding jets is important when one is interested in the processes that produce the partons that eventually fragment into jets. By themselves jets can provide an insight into QCD when the fragmentation is studied. Jets can also be used as probes of the QGP medium.

Experimentally jets are often studied with a jet reconstruction algorithm which clusters observed tracks to find a reasonable estimate of the initial parton. That is also the case in this thesis. The main observable studied is the jet fragmentation transverse momentum j_T which is defined as the perpendicular component of the momentum of jet constituents with respect to the jet axis, the best estimate of the initial parton. j_T measures the transverse nudge that fragmentation products receive.

The analysis studies collisions between protons and lead nuclei. Originally meant as a reference for lead-lead collisions to rule out possible cold nuclear matter effects [6]; effects caused by the regular 'cold' nuclear matter of a nucleus as opposed to QGP. However, p-Pb collisions have provided interesting physics by themselves. Many of the collective phenomena that in Pb-Pb collisions were attributed to QGP have been observed also in high multiplicity p-Pb collisions [7] and even in ultra high multiplicity pp collisions [7]. However observables of jet modification show no conclusive signals in p-Pb collisions [6, 7].

This thesis is organised as follows: Section 1 first gives a general introduction into the history and properties of QCD and Heavy-Ion physics. It is followed by a description of hard processes, jet fragmentation and hadronisation and how these processes might look like in a Heavy-Ion environment. Finally there is a discussion on the physics of small systems.

The experimental setup that was used to collect the data in this thesis is described in Section 2. It starts by explaining the accelerator facilities at CERN

and LHC in more detail. This is followed by a description of the ALICE experiment and its sub-detectors. A part of Section 2 is dedicated to coming upgrades of ALICE as this is a timely topic. In 2019-2020 ALICE will be upgraded and I have made a personal contribution to the TPC upgrade.

Section 3 gives a description of the event, track and cluster selection criteria used in the analysis. This is followed in Section 4 by the specific analysis methods used in this thesis. First the jet reconstruction algorithm used, anti- k_T , is described. Section 4 continues by introducing the j_T observable, how it is obtained and what methods are used to estimate background contribution and correct for detector effects. Finally the fitting method used for the final results is described. Section 5 gives the different systematic uncertainties that arise from the analysis.

Finally the results from the analysis are presented in Section 6. The results are compared to PYTHIA and Herwig Monte Carlo generators. Further discussion of the results is given in Section 7 when the results are compared to j_T results obtained with a different analysis method. Section 8 summarises the main results and gives an outlook for future.

1.1 Quantum chromodynamics

1.1.1 Foundation of QCD

There are four known basic interactions in the universe: gravity, electromagnetic, weak and strong interactions. The standard model of particle physics [2] includes three of these, electromagnetic, weak and strong interactions. The fourth one, gravity, is described well in all but the most extreme of cases by the theory of general relativity [8]. The standard model is a quantum field theory where particle interactions are dictated by local gauge symmetries [5].

The first interaction included in the standard model was the electromagnetic interaction. The foundations of quantum field theory and Quantum Electrodynamics (QED) were already laid out by the work by Dirac in 1927 [9]. The full theory of QED was formulated in 1946-1949 by Tomonaga [10], Schwinger [11, 12], Feynman [13]

Motivated by the success of a quantum field theory approach for the electromagnetic interaction physicists started working on the remaining interactions. However, the weak and strong nuclear interactions proved more challenging to formulate [14]. In the end the weak interaction was unified with the electromagnetic interaction into the electroweak theory. The final theory was formulated by Glashow [15], Salam [16] and Weinberg [17].

The theory of strong interactions became to be known as Quantum Chromodynamics (QCD). The search for a theory of strong interactions began after the formulation of QED and drew further inspiration from the introduction of new powerful particle accelerators that were capable of particle physics research in the 1950s. Before this particles were mainly discovered from cosmic rays. Positrons, neutrons and muons were discovered in the 1930s and charged pions were discovered in 1947 [18, 19]. The neutral pion was discovered in 1950 [20].

The Lawrence Berkeley National Laboratory started the Bevalac accelerator in 1954, Super Proton Synchrotron (SPS) in CERN began operating in 1959 and the Alternating Gradient Synchrotron (AGS) at Brookhaven started in 1960. With an energy of 33 GeV AGS was the most powerful accelerator of that time. By the beginning of 1960s several new particles had been discovered. These included antiprotons [21], antineutrons [22], Δ -particles and the six hyperons (Ξ^0 [23], Ξ^- [24], Σ^\pm [25], Σ^0 [26] and Λ [27]).

Facing this avalanche of new particles, physicists started the search for symmetries within them. Already in 1932 Heisenberg [28] had proposed an isospin model to explain similarities between the proton and the neutron. In 1962 Gell-Mann and Ne'eman presented that particles sharing the same quantum numbers (spin, parity) could be organised using the symmetry of SU(3). [29] Heisenberg's Isospin model followed the symmetry of SU(2). Using the SU(3) model known baryons

and mesons could be presented as octets. This also lead to the discovery of the Ω^- [30] particle since this was missing from the SU(3) decouplet that included heavier baryons.

The most simple representation of SU(3) was a triplet. Inside this triplet particles would have electric charges $2/3$ or $-1/3$. However, these had not been detected. In 1964 Gell-Mann [31] and Zweig [32] proposed that baryons and mesons would be bound states of these three hypothetical triplet particles that Gell-Mann called quarks and Zweig called aces. Now we know that these are the u , d and s quarks. However, this original quark model without colour was violating the Pauli exclusion principle. For example the Ω^- particle is comprised of three s quarks, two of which would have exactly the same quantum states, since spin can only have two values.

The idea of colour had already been presented by Greenberg in 1964 [33]. In 1971 Gell-Mann and Fritzsch presented their model [34], which solved the antisymmetry problem. They added a colour quantum number to quarks, which separated quarks of the same species. In the new colour model the baryonic wave function became

$$(qqq) \rightarrow (q_r q_g q_b - q_g q_r q_b + q_b q_r q_g - q_r q_b q_g + q_g q_b q_r - q_b q_g q_r), \quad (1)$$

The colour model was also supported by experimental evidence. The decay rate of a neutral pion with the addition of colours is

$$\Lambda(\pi^0 \rightarrow \gamma\gamma) = \frac{\alpha^2}{2\pi} \frac{N_c^2}{3^2} \frac{m_\pi^3}{f_\pi^2}. \quad (2)$$

For $N_c = 3$ this gives 7.75 eV and the measured value is (7.86 ± 0.54) eV [35].

Another observable that combines the colour information also to the number of quark flavours is the Drell-Ratio R [36]

$$R = \frac{\sigma(e^+ + e^- \rightarrow \text{hadrons})}{\sigma(e^+ + e^- \rightarrow \mu^+ + \mu^-)} = N_c \sum_f Q_f^2. \quad (3)$$

This ratio has the numerical value 2 when including the three light quarks u , d and s . When the collision energy reaches the threshold of heavy quark (c and b) production processes this increases to $^{10}/3$ (for $f = u, d, s, c$) and $^{11}/3$ (for $f = u, d, s, c, b$). The energy threshold ($\sqrt{s} \approx 350$ GeV) of $t\bar{t}$ production, has not been reached so far by any e^+e^- colliders.

The colour model explained why no free quarks had been observed as only colour neutral states are possible. The simplest ways of producing a colour neutral object are the combination of three quarks, and the combination of a quark-antiquark pair. These are known as baryons and mesons.

First experimental indication of the existence of quarks came in 1969 when a series of experiments at the Stanford Linear Accelerator Center (SLAC) revealed that protons and neutrons appeared to have some substructure [37, 38]. For this discovery they eventually received the Nobel Prize in Physics in 1990 [39]. Bjorken demonstrated that these results could be explained if protons and neutrons were composed of virtually noninteracting pointlike particles [40, 41]. Feynman [42] interpreted these objects as real particles and suggested they would be the quarks of Gell-Mann's model. At the time, however, this seemed mysterious; if all strongly interacting particles, hadrons, were composed of quarks, then quarks should surely be strongly interacting themselves. Why would they appear to be almost free inside hadrons? This turned out to be a key clue in formulating the theory of strong interactions. [14]

After the addition of colour the main ingredients of QCD had been established. The final quantum field theory of Quantum Chromodynamics formed quickly between 1972 and 1974. Main part of this was the work by Gross, Wilczek, Politzer and George for non-abelian gauge field theories [1, 43–46]. The work showed that quarks would indeed be asymptotically free in a non-abelian theory, which explained the results from SLAC. Gross, Wilczek and Politzer received the Nobel Prize in Physics for their work [47]. The role of gluons as a colour octet was presented by Fritzsch, Gell-Mann and Leutwyler in 1973 [48]. The theory had now 8 massless gluons to mediate the strong interaction.

The quark model was extended in 1974 when the discovery of the charm quark and the first charmed hadron, J/Ψ , was simultaneously published by teams from the SLAC [49], from Brookhaven National Laboratory [50] and from the ADONE collider in Frascati, Italy [51]. In 1976 the Nobel Prize in Physics was awarded to Richter and Ting for the discovery of the charm quark [52]. The existence of a fourth quark had already been speculated in 1964 by Bjorken and Glashow [53], but a proper prediction was provided by Glashow, Iliopoulos and Maiani in 1970 [15] based on symmetries between leptons and quarks in weak interactions.

However, these gluons had not been discovered. Indirect evidence of the existence had been seen as it was observed that only about half of the momentum of protons was transported by the quarks [54]. Direct evidence should be seen in electron-electron collisions as a third, gluonic, jet in addition to two quark jets. Three jet events were first seen in 1979 at the PETRA accelerator at DESY [55–57].

The two remaining quarks, bottom and top, were introduced by Kobayashi and Maskawa to explain CP-violation [58]. For this they received the Nobel Prize in Physics in 2008 [59]. Bottom quark was discovered soon after, in 1977, at Fermilab [60]. The heaviest quark, top quark, would eventually be discovered in 1995 by the CDF [61] and DØ [62] experiments at Fermilab.

1.1.2 Asymptotic Freedom

In Quantum Electrodynamics (QED) the electric charge is screened. In the vicinity of a charge, the vacuum becomes polarized. Virtual charged particle-antiparticle pairs around the charge are arranged so that opposing charges face each other. Since the pairs also include an equal amount opposite charge compared to the original charge the average charge seen by an observer at a distance is smaller. When the distance to the charge increases the effective charge decreases until the coupling constant of QED reaches the fine-structure constant $\alpha = \frac{1}{137}$. [5]

Contrary to QED, QCD is a non-abelian theory. In other words the generators of the symmetry group of QCD, SU(3), do not commute. This has the practical consequence that gluons interact also with other gluons, whereas in QED the neutral carrier particles, photons, only interact with charged particles. There is screening also in QCD because of the colour charges, but in addition to that there is antiscreening because of the gluon interactions. In QCD the antiscreening effect dominates over screening. Thus for larger distances to the colour charge the coupling constant is larger. This explains why no free colour charges can be observed. When the distance between charges increases the interaction strengthens until it is strong enough to produce a new quark-antiquark pair. On the other hand, at very small distances the coupling constant approaches zero. This is called asymptotic freedom. [5]

In 1975 Collins [63] predicted a state where individual quarks and gluons are no longer confined into bound hadronic states. Instead they form a bulk QCD matter that Edward Shuryak called Quark-Gluon plasma in his 1980 review of QCD and the theory of superdense matter [4]. QGP can be seen as a separate state of matter. A schematic view of a phase diagram for QCD matter is shown in Figure 1.

In the early universe at the age of 10^{-6} s after the Big Bang the conditions preferred the existence of QGP instead of hadronic matter. Nowadays bulk QCD matter, its properties and its phase transitions between hadronic matter and the quark-gluon plasma (QGP) can be explored in the laboratory, through collisions of heavy atomic nuclei at ultra-relativistic energies. The study of QCD matter at high temperature is of fundamental and broad interest. The phase transition in QCD is the only phase transition in a quantum field theory that can be probed by any present or foreseeable technology.

One important property of the QGP is the shear viscosity to entropy ratio, η/s . It is believed that this ratio has an universal minimum value of $1/4\pi \approx 0.08$, among all substances in nature. This limit would be reached in the strong coupling limit of certain gauge theories [65]. The temperature dependance of the ratio is shown in Figure 2. The minimum value of η/s is found in the vicinity of the critical temperature, T_c [66]. Finding the η/s values in QGP matter would therefore also

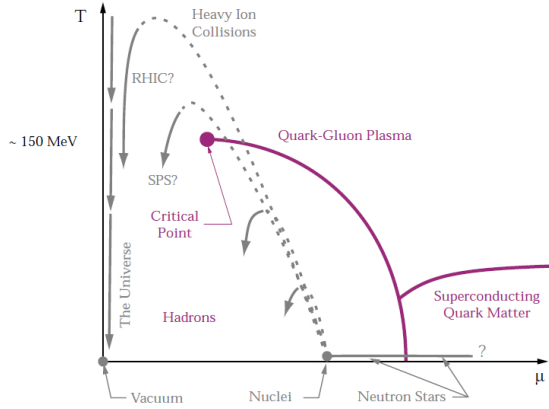


Figure 1: A schematic outline for the phase diagram of QCD matter at ultra-high density and temperature. The quark chemical potential μ that is on the x-axis represents the imbalance between quarks and antiquarks. At zero temperature this corresponds to the number of quarks but at higher temperatures there are also additional pairs of quarks and antiquarks. Along the horizontal axis the temperature is zero, and the density is zero up to the onset transition where it jumps to nuclear density, and then rises with increasing μ . Neutron stars are in this region of the phase diagram, although it is not known whether their cores are dense enough to reach the quark matter phase. Along the vertical axis the temperature rises, taking us through the crossover from a hadronic gas to the quark-gluon plasma. This is the regime explored by high-energy heavy-ion colliders. [64]

provide a way of determining the critical point of QCD matter.

The η/s value for the matter created in Au-Au collisions at RHIC ($\sqrt{s_{NN}} = 200 \text{ GeV}$) has been estimated to be 0.09 ± 0.015 [66], which is very close to the lowest value for a wide class of thermal quantum field theories [65] for all relativistic quantum field theories at finite temperature and zero chemical potential. This suggests that the matter created goes through a phase where it is close to the critical point of QCD.

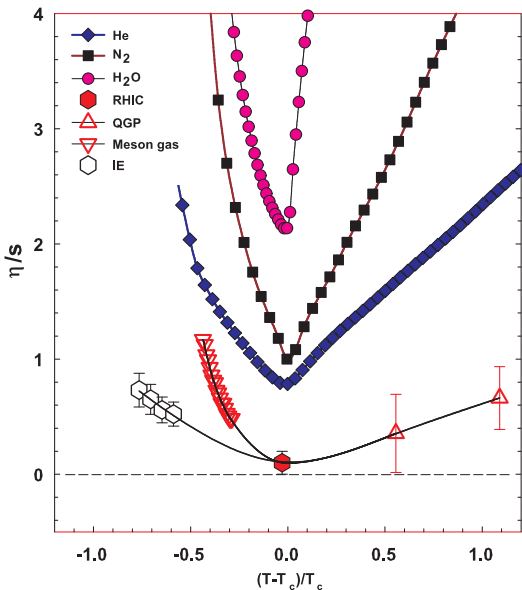


Figure 2: η/s as a function of $(T - T_c)/T_c$ for several substances as indicated. The $\eta/s = 0.09 \pm 0.015$ estimate at RHIC comes from Au-Au collisions at $\sqrt{s_{NN}} = 200$ GeV. The calculated values for the meson-gas have an associated error of $\sim 50\%$. The lattice QCD value $T_c = 170$ MeV is assumed for nuclear matter. The lines are drawn to guide the eye. [66]

1.2 Heavy-ion physics

The Quark Gluon Plasma (QGP) is experimentally accessible by colliding heavy-ions at high energies. Nowadays research of Heavy-Ion Collisions is mainly performed at two particle colliders; The Relativistic heavy-ion Collider (RHIC) at BNL in New York, USA and the Large Hadron Collider (LHC) at CERN in Switzerland. Energy densities at these colliders should be enough to produce QGP and convincing evidence of the creation has been seen at both colliders. Complementary research with heavy nuclei is also performed at the Super Proton Synchrotron (SPS) at CERN.

The development of heavy-ion physics is strongly connected to the development of particle colliders. Experimental study of relativistic heavy-ion collisions has been carried out for three decades, beginning with the Bevalac at Lawrence Berkeley National Laboratory (LBNL) [67], and continuing with the AGS at Brookhaven National Laboratory (BNL) [68], CERN SPS [69], RHIC at BNL and LHC at CERN.

1.2.1 History

The first heavy-ion collisions were performed at the Bevalac experiment at the Lawrence Berkeley National Laboratory [67] and at the Joint Institute for Nuclear Research in Dubna [70] at energies up to 1GeV per nucleon. In 1986 the Super Proton Synchrotron (SPS) at CERN started to look for QGP signatures in O+Pb collisions. The center-of-mass energy per colliding nucleon pair ($\sqrt{s_{NN}}$) was 19.4 GeV [69]. These experiments did not find any decisive evidence of the existence of QGP. In 1994 a heavier lead (Pb) beam was introduced for new experiments at $\sqrt{s_{NN}} \approx 17$ GeV. At the same time the Alternating Gradient Synchrotron (AGS) at BNL, Brookhaven collided ions up to ^{32}S with a fixed target at energies up to 28 GeV [68]. In 2000 CERN [71] presented compelling evidence for the existence of a new state of matter. Now SPS is used with 400 GeV proton beams for fixed-target experiments, such as the SPS heavy-ion and Neutrino Experiment (SHINE) [72], which tries to search for the critical point of strongly interacting matter.

The Relativistic heavy-ion Collider (RHIC) at BNL in New York, USA started its operation in 2000. The top center-of-mass energy per nucleon pair at RHIC, 200 GeV, was reached in the following years. The results from the experiments at RHIC have provided a lot of convincing evidences that QGP was created [73–76]. The newest addition to the group of accelerators capable of heavy-ion physics is the Large Hadron Collider (LHC) at CERN, Switzerland. LHC started operating in November 2009 with proton-proton collisions. First Pb-Pb heavy-ion runs started in November 2010 with $\sqrt{s_{NN}} = 2.76$ TeV, over ten times higher than at RHIC. Since then LHC has provided both Pb-Pb and p-Pb collisions and a short period of XeXe collisions. Table 1 shows a summary of these. Among the six experiments at LHC, the Large Ion Collider Experiment (ALICE) is dedicated to heavy-ion physics. Also CMS and ATLAS have active heavy-ion programs and LHCb uses its SMOG [77] to perform unique fixed target collisions with heavy ions.

Table 1: Summary of datasets. The integrated luminosities are from ALICE.

Run 1 (2009-2013)			Run 2 (2015-2018)			
	pp	p-Pb	Pb-Pb	pp	p-Pb	
pp	0.9 TeV	$\sim 200 \mu\text{b}^{-1}$		5.02 TeV	$\sim 1.3 \text{ pb}^{-1}$	
	2.76 TeV	$\sim 100 \text{ nb}^{-1}$		13.0 TeV	$\sim 25 \text{ pb}^{-1}$	
	7.0 TeV	$\sim 1.5 \text{ pb}^{-1}$		5.02 TeV	$\sim 3 \text{ nb}^{-1}$	
	8.0 TeV	$\sim 2.5 \text{ pb}^{-1}$		8.16 TeV	$\sim 25 \text{ nb}^{-1}$	
p-Pb		5.02 TeV	$\sim 15 \text{ nb}^{-1}$	XeXe	5.44 TeV	$\sim 0.3 \mu\text{b}^{-1}$
Pb-Pb		2.76 TeV	$\sim 75 \mu\text{b}^{-1}$	Pb-Pb	5.02 TeV	$\sim 1 \text{ nb}^{-1}$

1.3 Features of Heavy-Ion Collisions

1.3.1 Collision Geometry

In contrast to protons atomic nuclei are objects with considerable transverse size. The properties of a heavy-ion collision depend strongly on the impact parameter \vec{b} which is the vector connecting the centres of the two colliding nuclei at their closest approach. One illustration of a heavy-ion collision is shown in Figure 3.

Impact parameter defines the reaction plane which is the plane spanned by \vec{b} and the beam direction. Ψ_{RP} gives the angle between the reaction plane and some reference frame angle. Experimentally the reference frame is fixed by the detector setup. Reaction plane angle cannot be directly measured in high energy nuclear collisions, but it can be estimated with the event plane method [78].

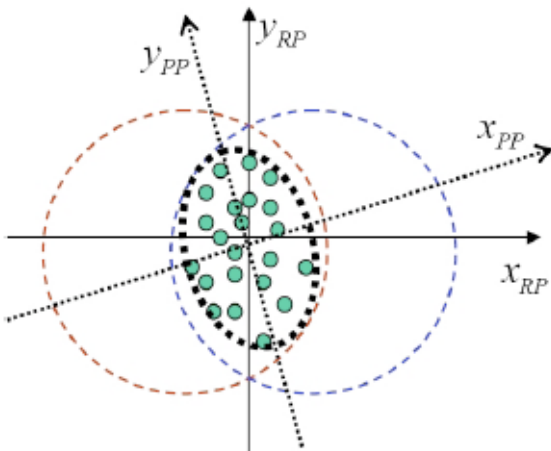


Figure 3: The definitions of the Reaction Plane and Participant Plane coordinate systems [79]. The dashed circles represent the two colliding nuclei and the green dots are partons that take part in the collision. x_{PP} and x_{RP} are the participant and reaction planes. The angle between x_{RP} and x_{PP} is given by Eq. (4). y_{PP} and y_{RP} are lines perpendicular to the participant and reaction planes.

Participant zone is the area containing the participants. The distribution of nucleons in the nucleus exhibits time-dependent fluctuations. Because the nucleon distribution at the time of the collision defines the participant zone, the axis of the participant zone fluctuates and can deviate from the reaction plane. The angle between the participant plane and the reaction plane is defined by [80]

$$\psi_{PP} = \arctan \frac{-2\sigma_{xy}}{\sigma_y^2 - \sigma_x^2 + \sqrt{(\sigma_y^2 - \sigma_x^2)^2 + 4\sigma_{xy}^2}}, \quad (4)$$

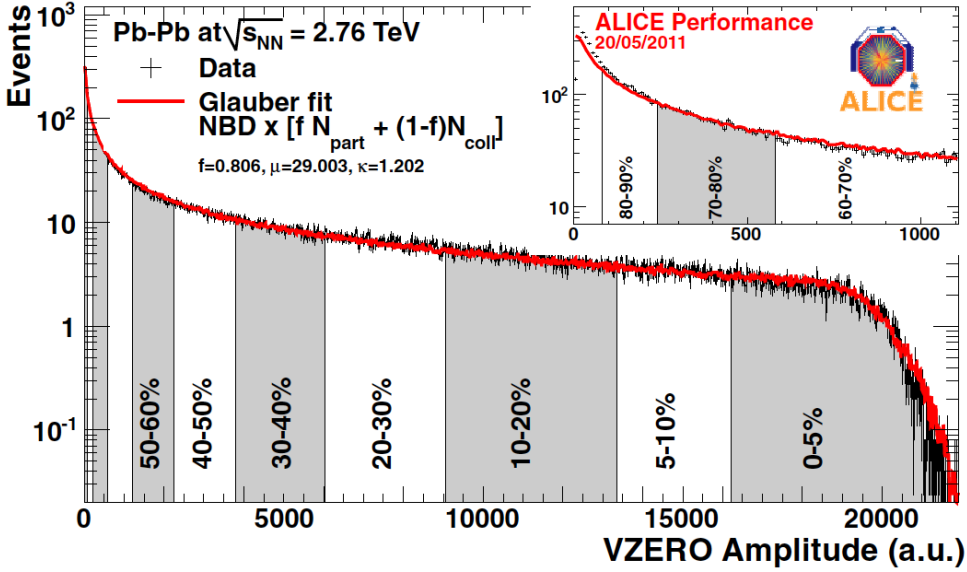


Figure 4: An illustration of the multiplicity distribution in ALICE measurements. The red line shows the fit of the Glauber calculation to the measurement. The data is divided into centrality bins [81]. The size of the bins corresponds to the indicated percentile.

where the σ -terms are averaged over the energy density.

$$\sigma_y^2 = \langle y^2 \rangle - \langle y \rangle^2, \sigma_x^2 = \langle x^2 \rangle - \langle x \rangle^2, \sigma_{xy} = \langle xy \rangle - \langle x \rangle \langle y \rangle \quad (5)$$

The impact parameter is one way to quantize the centrality of a heavy-ion collision but it is impossible to measure in a collision. It can be estimated from observed data using theoretical models, but this is always model-dependent and to compare results from different experiments one needs an universal definition for centrality.

Instead in practice centrality is defined by dividing collision events into percentile bins by the number participants or experimentally by the observed multiplicity. Centrality bin 0-5% corresponds to the most central collisions with the highest multiplicity and higher centrality percentages correspond to more peripheral collisions with lower multiplicities. A multiplicity distribution from ALICE measurements [81] illustrating the centrality division is shown in Figure 4. The distribution is fitted using a phenomenological approach based on a Glauber Monte Carlo [82] plus a convolution of a model for the particle production and a negative binomial distribution.

The Glauber Model is often used to model the nuclear geometry in a heavy-

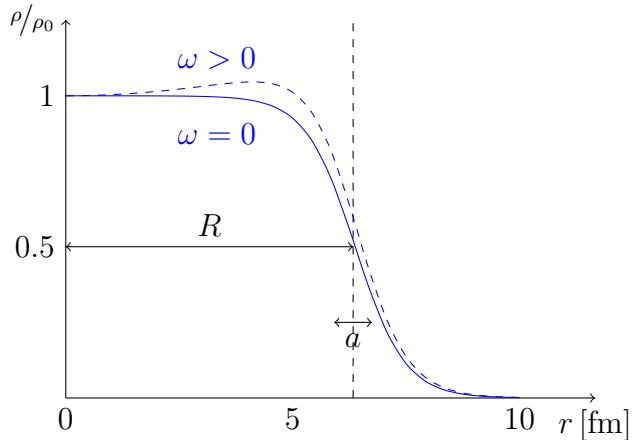


Figure 5: Woods-saxon distribution, with typical values for a Pb nucleus, $a = 0.55\text{fm}$ and $R = 6.6\text{fm}$.

ion collision. The model was originally introduced already in 1958 [83] and the modern terminology and tools were introduced in 1976 [84] by Białas, Bleszyński, and Czyż to model inelastic nuclear collisions.

The model starts by defining the thickness function which is the integral of the nuclear density over a line going through the nucleus with minimum distance s from its center

$$T_A(s) = \int_{-\infty}^{\infty} dz \rho(\sqrt{s^2 + z^2}), \quad (6)$$

where $\rho(\sqrt{s^2 + z^2})$ is the number density of nuclear matter. This can be experimentally determined by studying the nuclear charge distribution in low-energy electron-nucleus scattering experiments [82, 85]. For a spherically symmetric nucleus a good approximation is given by the Woods-Saxon potential [86].

$$\rho(r) = \frac{\rho_0(1 + \omega r^2/R^2)}{1 + \exp(\frac{r-R}{a})}, \quad (7)$$

where ρ_0 is the nucleon density in center of the nucleus, R is the nuclear radius, a parametrizes the depth of the skin and ω can be used to introduce a surface excess. Figure 5 shows how this distribution looks like. With $\omega = 0$ the density stays relatively constant as a function of r until around R where it drops to almost 0 within a distance given by a .

Overlap function is an integral of the thickness functions of two colliding nuclei over the overlap area. This can be seen as the material that takes part in the collision. It is given as a function of the impact parameter b

$$T_{AB}(\vec{b}) = \int d^2s T_A(\vec{s}) T_B(\vec{s} - \vec{b}) \quad (8)$$

The average overlap function, $\langle T_{AA} \rangle$, in an A-A collisions is given by [87]

$$\langle T_{AA} \rangle = \frac{\int T_{AA}(b) db}{\int (1 - e^{-\sigma_{pp}^{inel} T_{AA}(b)}) db}. \quad (9)$$

Using $\langle T_{AA} \rangle$ one can calculate the mean number of binary collisions

$$\langle N_{coll} \rangle = \sigma_{pp}^{inel} \langle T_{AA} \rangle, \quad (10)$$

where the total inelastic cross-section, σ_{pp}^{inel} , gives the probability of two nucleons interacting. As each binary collision has equal probability for direct production of high-momentum partons, the number of binary collisions is related to the hard processes in a heavy-ion collision. Thus the number of high momentum particles is proportional to $\langle N_{coll} \rangle$ [86, 88, 89]. This required knowledge of σ_{inel}^{NN} , which can be measured in proton-proton collisions at different energies. At the LHC the most precise cross section measurements come from TOTEM [90].

Soft production on the other hand is related to the number of participants [88]. It is assumed that in the binary interactions participants get excited and further interactions are not affected by previous interactions because the time scales are too short for any reaction to happen in the nucleons. After the interactions excited nucleons are transformed into soft particle production. The average number of participants, $\langle N_{part} \rangle$ can be calculated from the Glauber model

$$\begin{aligned} \langle N_{part}^{AB}(\vec{b}) \rangle &= \int d^2s T_A(\vec{s}) \left[1 - \left[1 - \sigma_{NN} \frac{T_B(\vec{s} - \vec{b})}{B} \right]^B \right] \\ &+ \int d^2s T_B(\vec{s}) \left[1 - \left[1 - \sigma_{NN} \frac{T_A(\vec{s} - \vec{b})}{A} \right]^A \right]. \end{aligned} \quad (11)$$

There are two often used approaches to Glauber calculations. The optical approximation is one way to get simple analytical expressions for the nucleus-nucleus interaction cross-section, the number of interacting nucleons and the number of nucleon-nucleon collisions. In the optical Glauber it is assumed that during the crossing of the nuclei the nucleons move independently and they will be essentially undeflected.

With increased appreciation of the physics emerging from fluctuations in the collision geometry the Glauber Monte Carlo (GMC) approach has emerged as a

method to get a more realistic description of the collisions. In GMC the nucleons are distributed randomly in a three-dimensional coordinate system according to the nuclear density distributions [86]. A heavy-ion collision is then treated as a series of independent nucleon-nucleon collisions, where in the simplest model nucleons interact if their distance in the plane orthogonal to the beam axis, d , satisfies

$$d < \sqrt{\sigma_{\text{inel}}^{\text{NN}}} \quad (12)$$

The average number of participants and binary collisions can then be determined by simulating many nucleus-nucleus collisions. The results of one GMC Pb-Pb event with impact parameter $b = 9.8$ fm is shown in Figure 6

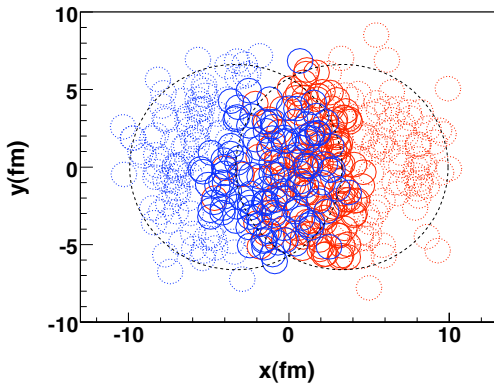


Figure 6: The results of one Glauber Monte Carlo simulation for a Pb–Pb collision. Big circles with black dotted boundaries represent the two colliding nuclei. The participant zone is highlighted with the solid red line. Small red and blue circles represent nucleons. Circles with solid boundaries are participants i.e. they interact with at least one nucleon from the other nucleus. Circles with dotted boundaries are spectators which do not take part in the collision. Figure from [91]

1.3.2 Collective motion

Quite often the evolution of a heavy-ion event can be divided into four stages. A schematic representation of the evolution of the collisions is shown in Figure 7. Stage 1 follows immediately the collision. This is known as the pre-equilibrium stage. The length of this stage is not known but it is assumed to last about $1 \text{ fm}/c$ in proper time τ .

The second stage is the regime where thermal equilibrium or at least near-equilibrium is reached. This lasts about $5 - 10 \text{ fm}/c$ until the temperature of

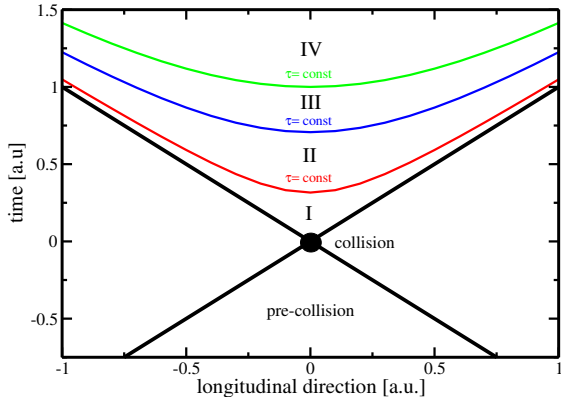


Figure 7: Schematic representation [92] of a heavy-ion collision as the function of time and longitudinal coordinates z . The various stages of the evolution correspond to proper time $\tau = \sqrt{t^2 - z^2}$ which is shown as hyperbolic curves separating the different stages.

the system sinks low enough for hadronization to occur and the system loses its deconfined, strongly coupled state. The third stage is the hadron gas stage where the hadrons still interact with each other. This ends when hadron scattering becomes rare and they no longer interact. In the final stage hadrons are free streaming and they fly in straight lines until they reach the detector.

In a heavy-ion collision the bulk collective particle production that is emitted from the QGP medium is referred to as flow. After the formation of the QGP, the matter begins to expand as it is driven outwards by the strong pressure difference between the center of the collision zone and the vacuum outside the collision volume. The pressure-driven expansion is transformed into flow of low-momentum particles in the hadronization phase. Since the expansion is mainly isotropic the resulting particle flow is isotropic with small anisotropic corrections that are of the order of 10% at most. The isotropic part of flow is referred to as radial flow.

The transverse momentum spectra dN/dp_T in heavy-ion collisions is shown in Figure 8. The vast majority of produced particles have small p_T . The difference between the yield of 1 GeV/c and 4 GeV/c particles is already 2-3 orders of magnitude. Any observables that are integrated over p_T are therefore dominated by the small momentum particles.

The geometry of the heavy-ion collision produces an anisotropic component to the collective motion. In a non-central heavy-ion collision, with a large impact parameter, the shape of the impact zone is almond-like. In a central collision the overlap region is almost symmetric in the transverse plane. In this case the impact parameter is small. Collisions with different impact parameters are shown in Figure 9.

The pressure gradient is largest in-plane, in the direction of the impact parameter b , where the distance from high pressure, at the collision center, to low pressure, outside the overlap zone, is smallest. This leads to stronger collective flow along the direction of b , which in turn results in enhanced thermal emission through a larger effective temperature into this direction, as compared to out-of-plane [94–96]. The resulting flow is illustrated in Figure 9.

Flow is typically quantified in the form of a Fourier composition

$$E \frac{d^3N}{dp^3} = \frac{1}{2\pi p_T} \frac{d^2N}{dp_T d\eta} \left(1 + \sum_{n=1}^{\infty} 2v_n(p_T, \eta) \cos(n(\phi - \Psi_n)) \right), \quad (13)$$

where the coefficients v_n give the relative strengths of different anisotropic flow

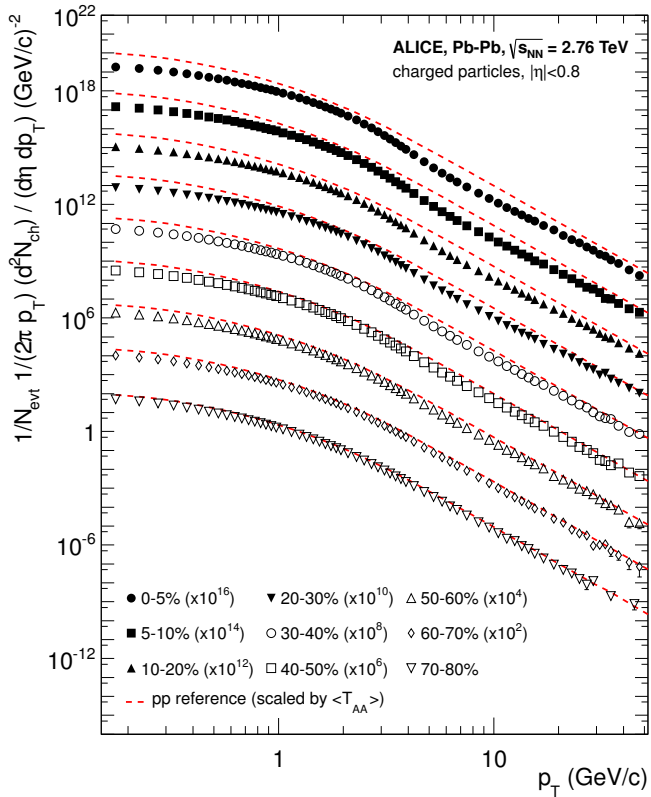


Figure 8: Charged particle spectra measured by ALICE [93] for the 9 centrality classes given in the legend. The distributions are offset by arbitrary factors given in the legend for clarity. The distributions are offset by arbitrary factors given in the legend for clarity. The dashed lines show the proton-proton reference spectra scaled by the nuclear overlap function determined for each centrality class and by the Pb-Pb spectra scaling factors [93].

components and the overall normalisation gives the strength of radial flow. Elliptic flow, i.e. flow with two maxima, is represented by v_2 and v_3 represents triangular flow. The first coefficient, v_1 , is connected to directed flow [97]. This will however in total be zero because of momentum conservation. It can be nonzero in some rapidity or momentum regions but it must be canceled by other regions.

In a peripheral collision v_2 is the dominant part of anisotropic flow as it arises from the asymmetric geometry of the collision region. Higher harmonics, the most notable of which is the triangular flow, come from fluctuations in the initial conditions [98]. As the colliding nuclei are not static objects, the arrangement of the nucleons at the time of the collision is random. The shape of the collision zone is not a perfect almond. Instead it can have a more complex shape. Also inside the collision zone the density of the created medium is not homogenous but it can have denser hot spots

It has been noted that higher harmonics of v_n would be suppressed by viscous effects and that the shape of v_n as a function of n would provide another valuable tool for studying η/s [99]. For a long time it was believed that the odd harmonics would be negligible. In 2007 Mishra et al. [100] argued that density inhomogeneities in the initial state would lead to non-zero v_n values for higher harmonics including v_3 .

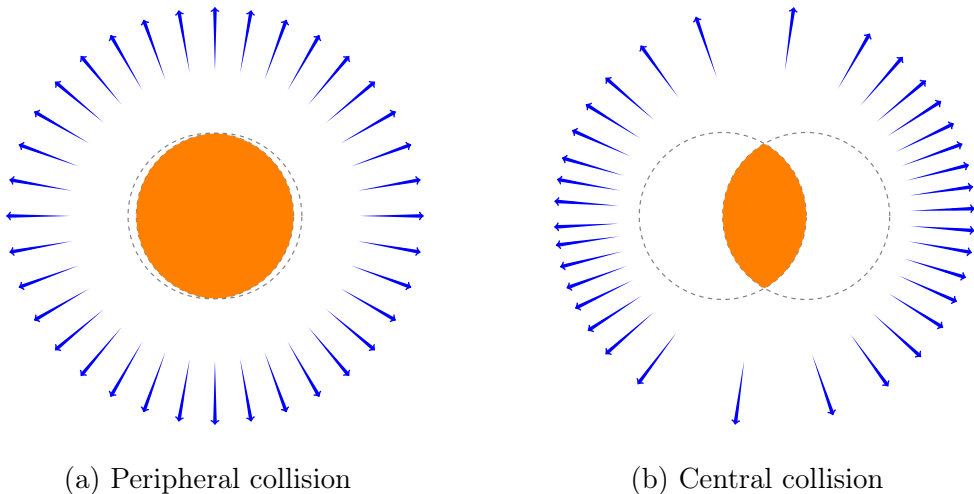
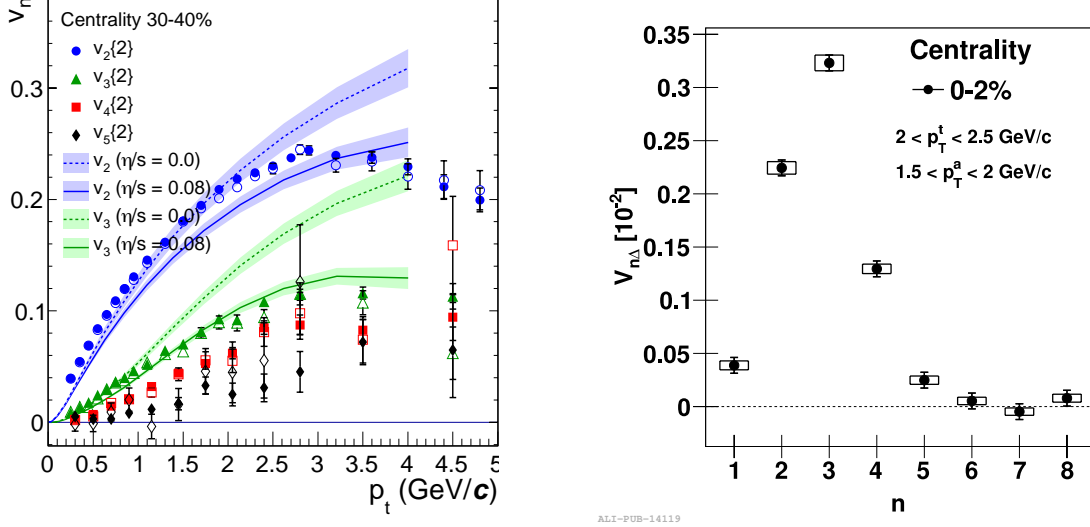


Figure 9: Illustration of flow in momentum space in central and peripheral collisions. The density of the arrows represent the magnitude of flow seen at a large distance from the collision in the corresponding azimuthal direction. In a peripheral collision momentum flow into in-plane direction is strong and flow into out-of-plane direction is weak. In a central collision anisotropy in flow is smaller, but the total yield of particles is larger.



(a) ALICE measurement of v_2, v_3, v_4, v_5 as a function of transverse momentum. The flow coefficients are determined by two-particle correlations using different rapidity separations. The full and open symbols are for $\Delta\eta > 0.2$ and $\Delta\eta > 1.0$. The results are compared to hydrodynamic predictions [102] with different values of η/s [103].

(b) Amplitude of v_n harmonics as a function of n for the 2% most central collisions as measured by ALICE [104].

Figure 10: Flow measurements of higher harmonics

The first one to predict anisotropic flow in heavy-ion collisions was Ollitrault in 1992 [94]. However, the first papers on anisotropy did not discuss the Fourier composition. Instead they approached the problem with a classic event shape analysis. (sphericity) The first experimental studies of anisotropy were performed at the AGS [101] in 1993, where it was noted that the anisotropy of particle production in one rapidity region correlates with the reaction plane angle defined in another rapidity region. The first ones to present the Fourier decomposition were Voloshin and Zhang in 1996 [97]

Measurements of different flow harmonics are shown in Figure 10. The left panel shows different flow harmonics as a function of p_T as measured by ALICE [103] in peripheral collisions. In general flow coefficients decrease as a function of n after $n = 2$. Central collisions are an exception. The right panel of Figure 10 shows v_n as a function of n in central collisions as measured by ALICE [104]. The results are compared to hydrodynamic predictions [102].

The measured collective flow in heavy-ion collisions has been successfully modelled with the relativistic version of hydrodynamics. The power of relativistic hydrodynamics lies in its simplicity and generality. Hydrodynamics only requires that there is local thermal equilibrium in the system. In order to reach thermal equilibrium the system must be strongly coupled so that the mean free path is shorter than the length scales of interest, which is assumed to hold for QGP phase of a heavy-ion collision [92].

The use of relativistic hydrodynamics in high-energy physics dates back to Landau [105] and the 1950's, before QCD was discovered. Back then it was used in proton-proton collisions. Development of hydrodynamics for the use of heavy-ion physics has been active since the 1980's, including Bjorken's study of boost-invariant longitudinal expansion and infinite transverse flow [106]. Major steps were taken later with the inclusion of finite size and and dynamically generated transverse size [107, 108], a part of which was done at the University of Jyväskylä.

Understanding of the properties of the QGP has been improved with the help of new data from LHC and RHIC and theoretical developments over the years. For example, as shown in Figure 11(a), the quantification of the temperature dependence shear viscosity over entropy ratio has been tested with event-by-event Eskola-Kajantie-Ruuskanen-Tuominen (EKRT) + viscous hydrodynamic calculations [109], where the first qualitative possibilities were investigated. In this hydrodynamic calculations, the initial energy density profiles are calculated using a next-to-leading order perturbative-QCD + saturation model (EKRT) [110, 111]. The subsequent space-time evolution is described by relativistic dissipative fluid dynamics with different parametrisations for the temperature dependence of the shear viscosity to entropy density ratio $\eta/s(T)$. This model gives a good description of the charged hadron multiplicity and the low- p_T region of the charged hadron spectra at RHIC and the LHC [109]. Each of the $\eta/s(T)$ parametrisations have been adjusted to reproduce the measured v_n from central to mid-peripheral collisions. The model calculations in which the temperature of the phase transition is larger than for "param1" are ruled out by the previous measurements [112] and their studies. The remaining two sets of parameters which described most of data is labeled as "best fits" in Figure 11(a). For the "param1" parametrisation the phase transition from the hadronic to the QGP phase occurs at the lowest temperature, around 150 MeV. This parametrisation is also characterised by a moderate slope in $\eta/s(T)$ which decreases (increases) in the hadronic (QGP) phase.

The estimation of the η/s has been also established with Bayesian analysis, which is applied to form the initial conditions with no assumptions on the physical mechanisms of the entropy production [113]. The robust statistical analytical methods allows performing the model to data calibration in a multi-dimensional parameter space. In addition to finding the most likely combination of input pa-

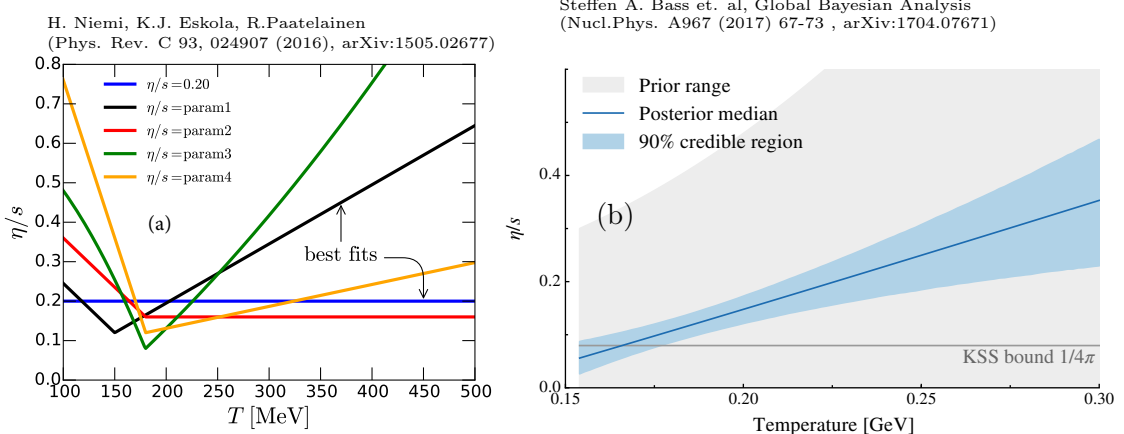


Figure 11: Temperature dependence of η/s . *left:* Different parametrisations of $\eta/s(T)$ that have been tested in hydrodynamical simulations. *right:* Result of a global Bayesian analysis narrowing down the possible $\eta/s(T)$ behaviour [113]

rameters, the Bayesian statistical method also provides the full uncertainty quantification in the form of posterior probability distributions for all the parameters. The resulting $\eta/s(T)$ parametrisation is shown in Figure 11(b).

Based on the aforementioned model calculations, the phase transition from the hadronic to the QGP phase occurs at the lowest temperature, around 150 MeV. Although the temperature dependence of the η/s is currently not well known, the calculations generally suggest a minimum value of η/s from 0.08 to 0.12, close to the universal limit $1/(4\pi)$ [65].

Recently, several advancements have been made in order to further constrain the temperature dependence of η/s . New observables, such as the symmetric cumulants [112, 114], have provided detailed information on the temperature dependence over the evolution of the QGP. Furthermore, the non-linear formalism has resulted in remarkable new constraints on the initial conditions [115], and the η/s at the freeze-out conditions, for which is among the least understood parts of hydrodynamic calculations.

1.4 Hard processes

1.4.1 pQCD factorization

The term Hard Scattering is used in connection with the scattering of two point-like constituents (partons) of colliding nucleons, when the momentum transfer Q^2 is large ($Q \gg \Lambda_{\text{QCD}}$). Figure 12 shows the incoming partons, quarks or gluons, as they exchange a space-like virtual gluon and produce two highly virtual outgoing partons. The outgoing partons will eventually fragment into collimated showers of partons, referred to as jets.

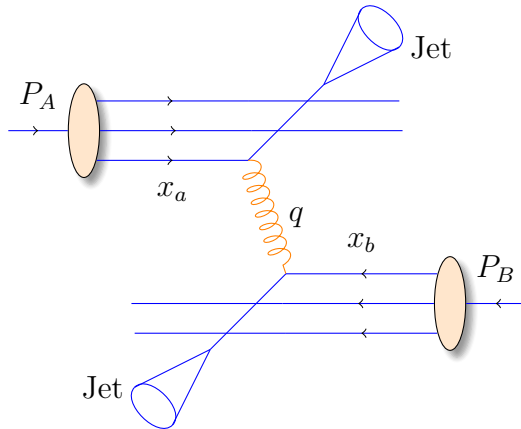


Figure 12: Schematic view of hard scattering process between 2 protons, producing 2 jets

Historically one would study hard scatterings foremost with inclusive hadron spectra. In this context hadron production from hard scatterings can be factorised into three components; the parton distribution functions f_a, f_b that give the probability of getting a parton with momentum fraction x of the proton, the cross section of the elementary scattering $ab \rightarrow cd$, and the fragmentation functions that give the probability of getting hadron h from the parton.

$$\frac{d\sigma_{pp}^h}{dy d^2p_T} = K \Sigma_{abcd} \int dx_a dx_b f_a(x_a, Q^2) f_b(x_b, Q^2) \frac{d\sigma}{dt} (ab \rightarrow cd) \frac{D_{h/c}^0}{\pi z_c}, \quad (14)$$

where

$$x_{a,b} = \frac{|p_{a,b}|}{|p_{\text{proton}}|}. \quad (15)$$

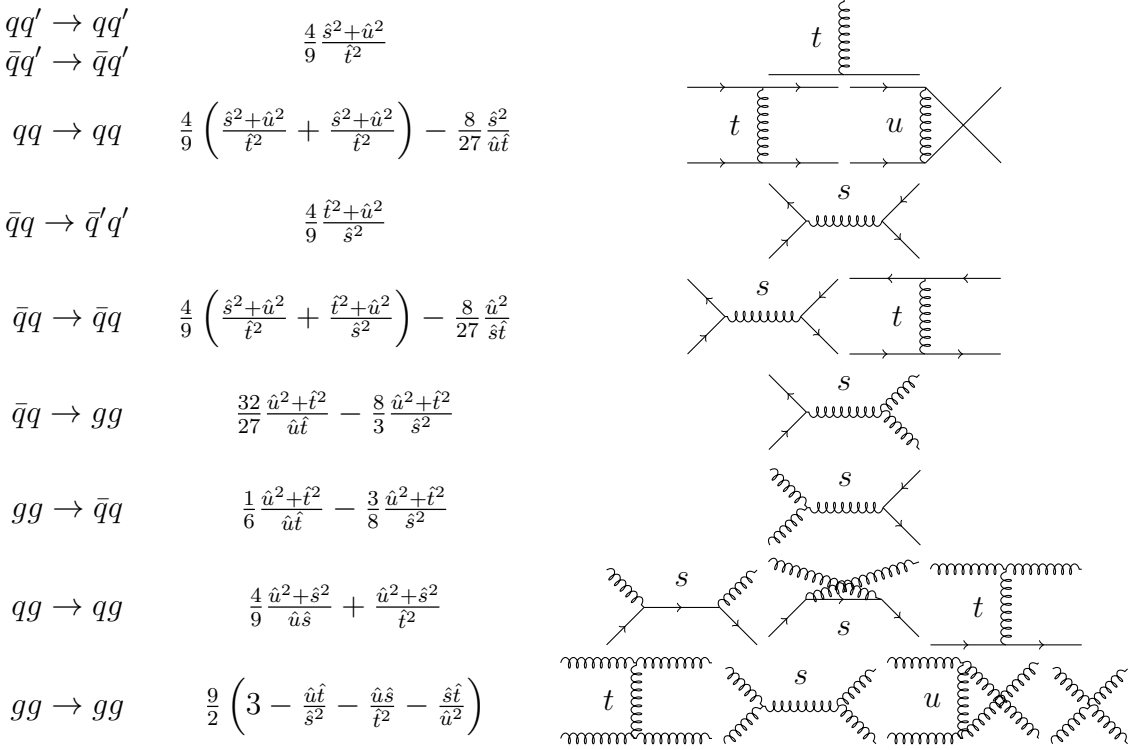


Figure 13: The basic pQCD processes and their quadratic matrix elements

Parton distribution functions will be discussed further in the following section. The elementary cross section $ab \rightarrow cd$ can be calculated from QCD. A summary of the first order $2 \rightarrow 2$ processes in QCD is shown in Figure 13.

The final component in the factorization, fragmentation functions, describe the distribution of the fractional momenta of fragments radiated from the outgoing parton. In a leading order picture, it can be interpreted as the probability that the observed final state originates from a given parton [116]. Like the PDFs they are non-perturbative and must be determined experimentally. The measurement is usually performed in e^+e^- collisions where the kinematics are better controlled.

Parton Distribution Function

Parton Distribution Functions (PDFs) $f_a(x)$ give the differential probability for parton a to carry momentum fraction x of the proton momentum. As the PDFs cannot be calculated from first principles they are measured in Deeply Inelastic Scattering (DIS) experiments [117] and are extrapolated to the relevant momentum scales using the Dokshitzer-Gribov-Lipatov-Altarelli-Parisi (DGLAP) evolution scheme [118–120]

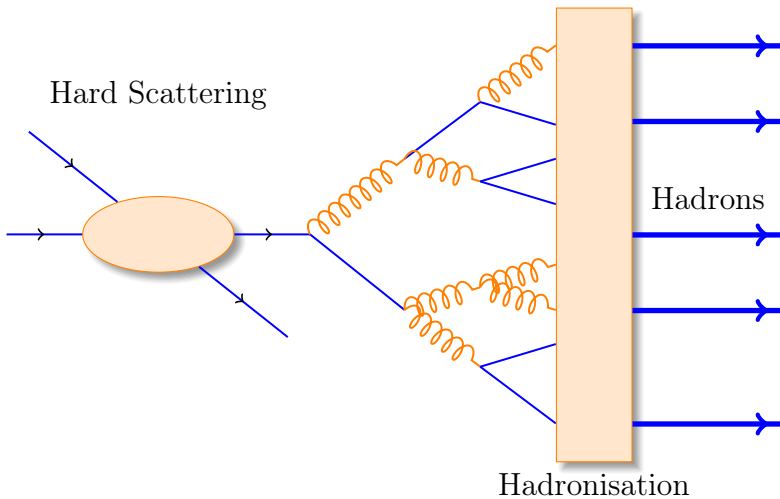


Figure 14: An illustration of jet showering. The highly virtual parton from the hard scattering will produce a shower of softer partons. When the virtuality is low enough the shower will go through a hadronisation process that produces the hadrons, which will be eventually observed in the detector.

$$\mu_F^2 \frac{\partial f_i(x, \mu_F^2)}{\partial \mu_F^2} = \sum_j \frac{\alpha_s(\mu_F)}{2\pi i} \int_x^1 \frac{dz}{z} P_{ij}(z) f_j\left(\frac{x}{z}, \mu_F^2\right), \quad (16)$$

where μ_F is a factorization scale. The splitting functions P_{ij} describe a probability to radiate parton i from parton j as a function of the momentum fraction z carried away by the offspring parton. Different theory interpretation and experimental data gives rise to different PDF's. Thus there are several commonly used PDF sets: CTEQ [121], HERAPDF [122], PDF4LHC [123], etc.

1.4.2 Jet showering

More detailed studies of the hard processes require a formulation of the showering process. The full picture is a complicated $2 \rightarrow n$ scattering, but it is typically seen as a series of $1 \rightarrow 2$ splittings with decreasing virtuality following the initial $2 \rightarrow 2$ scattering [124].

To first order the cascade is governed by the DGLAP evolution equation [118–120]

$$dP_a(z, Q^2) = \frac{dQ^2}{Q^2} \frac{\alpha_s}{2\pi} P_{a \rightarrow bc}(z) dz, \quad (17)$$

which gives the differential probability that parton a (mother) will branch to two partons b and c (daughters), at a virtuality scale Q^2 . Daughter b takes a fraction

z of the parton a energy and daughter c takes energy fraction $1 - z$. The splittings kernels $P_{a \rightarrow bc}(z)$ are

$$P_{q \rightarrow qg}(z) = \frac{4}{3} \frac{1+z^2}{1-z} \quad (18)$$

$$P_{g \rightarrow gg}(z) = 3 \frac{(1-z)(1-z)^2}{z(1-z)} \quad (19)$$

$$P_{g \rightarrow q\bar{q}}(z) = \frac{n_f}{2} (z^2 + (1-z)^2), \quad (20)$$

where n_f is the kinematically allowed number of quark flavours. There is some freedom in how the evolution variable Q^2 is chosen. If $Q^2 = f(z)m^2$ and $f(z)$ is a positive and a smooth function it holds that

$$\frac{dQ^2}{Q^2} dz = \frac{dm^2}{m^2} dz. \quad (21)$$

Of the Monte Carlo generators used in this thesis PYTHIA uses m^2 as the evolution variable [125], while HERWIG uses an energy-weighted emission angle $E^2(1 - \cos \theta) \approx m^2/z(1-z)$ [126].

Formally eq 17 corresponds to the emission of an infinite number of partons. However very soft and collinear gluons need not be considered and one can introduce an effective cut-off scale Q_0 , usually taken to be of the order of 1 GeV.

Going further one approach is to introduce time ordering, i.e. to decide which of the emissions occurs first. This is done in the form of a Sudakov form factor [127]

$$P_a^{no}(Q_{\max}^2, Q^2) = \exp \left(- \int_{Q^2}^{Q_{\max}^2} \int_{z_{\min}}^{z_{\max}} dP_a(z', Q'^2) \right), \quad (22)$$

which gives the probability that no emissions occur between the initial maximum scale Q_{\max}^2 and a given Q^2 and within limits $z_{\min} < z < z_{\max}$. Thus the probability for the first branching to occur at $Q^2 = Q_a^2$ is given by

$$d\Delta_a(z, Q_a^2, Q_{\max}^2) = dP_a(z, Q_a^2) P_a^{no}(Q_{\max}^2, Q_a^2). \quad (23)$$

Partons b and c that were produced will further branch with maximum virtuality scale Q_{\max}^2 given by Q_a^2 . Similarly their daughters will continue branching until the cutoff scale is reached, thus producing a shower.

1.4.3 Soft gluon radiation and angular ordering

Let us now consider a case where a gluon splits into two quarks, and one of the created quarks emits a soft gluon as seen in Figure 15. In the laboratory frame the time it takes for a gluon to be emitted from a quark can be estimated to be [128]

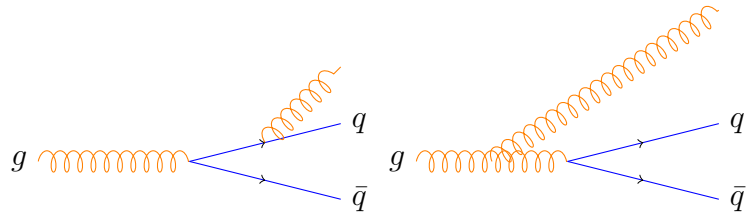


Figure 15: Soft gluon production

$$t_{\text{emit}} \approx \frac{1}{E_q}, \quad (24)$$

where the energy of the quark is given by E_q . In the rest frame of the quark its energy is given by its virtuality M_{virt} and assuming the quark is massless the Lorentz factor between the rest frame the laboratory frame is

$$\gamma = \frac{E_q}{M_{\text{virt}}}. \quad (25)$$

Thus the emission time can be written as

$$t_{\text{emit}} \approx \frac{E_q}{M_{\text{virt}}^2} = \frac{E_q}{(k + p)^2}, \quad (26)$$

where k and p are the four-momenta of the gluon and the quark after the gluon emission. This can be written open in the laboratory frame. Through assuming that the end products are massless and Taylor-expanding the resulting cosine term gives a form that expresses the emission time using the opening angle θ_{kq} between the quark and the gluon

$$t_{\text{emit}} \approx \frac{1}{k\theta_{kq}^2}. \quad (27)$$

The transverse wavelength of the emitted gluon is $\lambda_{\perp}^{-1} = k_{\perp} \approx k\theta_{kq}$. Thus we get

$$t_{\text{emit}} \approx \frac{\lambda_{\perp}}{\theta_{kq}}. \quad (28)$$

The secondary gluon can only probe the quark of the earlier splitting if the transverse wavelength is smaller than the transverse separation of the produced $q\bar{q}$ pair. The transverse separation is given by

$$r_{\perp}^{q\bar{q}} \approx \theta_{q\bar{q}} t_{\text{emit}} \approx \lambda_{\perp} \frac{\theta_{q\bar{q}}}{\theta_{kq}}. \quad (29)$$

Thus in order for the emission to probe the individual quark, the opening angle of the $q\bar{q}$ splitting, $\theta_{q\bar{q}}$, must be larger than θ_{kq} . If the opening angle θ_{kq} is larger, the gluon can't distinguish between the quark and the antiquark, so it probes the state of the system before the splitting, i.e. it can be treated like it was emitted from the primary gluon.

This leads to the angular ordering of soft gluon radiation. Each successive angle must be smaller than the previous one. The effect can be calculated in all orders [128] and in the DGLAP formalism one can select the evolution variable Q^2 in a way that ensures angular ordering as is done in the Herwig MC generator [126]. In PYTHIA 8 this is strictly not included, but the transverse momentum ordered showers are as accurate in describing the soft gluon emissions as the angular ordered showers [127].

1.4.4 Jet hadronisation

When the virtuality of the shower is low enough, the shower starts to hadronise. In this regime the parton shower reaches a scale close to Λ_{QCD} and the perturbative description is no longer valid. Thus the hadronisation stage must be described in a non-perturbative manner. In general hadronisation is assumed to be universal, i.e. it shouldn't depend on the collision energy or system. The most simple scenario that is used in several theory calculations is the so-called local parton-hadron duality [129]. In the local parton-hadron duality hypothesis it is assumed that there exists a low virtuality scale Q_0 in which the hadronisation happens, that is independent of the scale of the primary hard process. At this scale the partons are transformed into hadrons, assuming that the flow of momentum and quantum numbers for the hadrons can be directly obtained from those of partons introducing only small normalising constants.

The next sections will present more complicated hadronisation models used in Monte Carlo generators, PYTHIA and Herwig.

Lund string model

One common implementation in MC generators is the Lund string fragmentation algorithm [130]. The string model is based on the fact that in QCD linear confinement is expected over large distances [127]. This can be modelled by imagining a colour flux tube being stretched between the outgoing partons. The left side of Figure 16 illustrates this point for a $q\bar{q}$ -pair. The tube is assumed to have a uniform fixed transverse size of about 1 fm along its length, which leads to a linearly rising potential $V(r) = \kappa r$, where the string constant κ describes the amount of energy per unit length. A value of $\kappa \approx 1 \text{ GeV/fm} \approx 0.2 \text{ GeV}^2$ can be obtained from hadron mass spectroscopy [127].

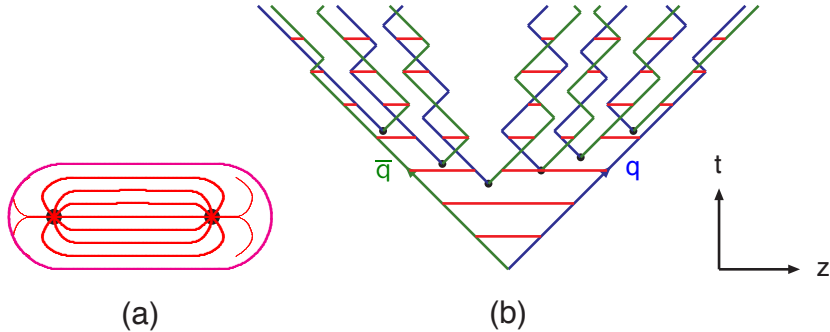


Figure 16: (a) A flux tube spanned between a quark and an antiquark. (b) The motion and breakup of a string system, with the two transverse degrees of freedom suppressed (diagonal lines are (anti)quarks, horizontal ones snapshots of the string field) [127].

The evolution of string fragmentation is illustrated schematically on the right side of Figure 16. This figure is drawn in a light cone presentation, so the initial quark and antiquark are going to separate directions at the speed of light. The string between them, illustrated in the figure by the red line, stretches until its potential energy becomes high enough that it can break, forming a new quark-antiquark pair. If the original pair was $q\bar{q}$ and the new pair $q'\bar{q}'$, now two new pairs $q\bar{q}'$ and $q'\bar{q}$ have formed. As these particles are also moving away from each other, the strings between them can stretch and break, creating yet more pairs. The process continues until the invariant mass of the system connected by the string becomes small enough and a final state meson is formed.

To mathematically model the string one can use a massless relativistic string with no transverse degrees of freedom. The gluons are represented as energy and momentum carrying kinks on the string with incoherent sums of one colour charge and one anticolour charge. When this string breaks, it is classically required that the created quark and antiquark are produced at a certain distance if they are to have any mass or transverse momentum. However, taking into account quantum mechanics, the pair must be created at one point and then tunnel out to the classically allowed region. Thus the probability to create a new quark-antiquark pair becomes proportional to the tunnelling probability [130].

$$P_{\text{tunnelling}} \propto \exp\left(\frac{-\pi m_\perp^2}{\kappa}\right) = \exp\left(\frac{-\pi m^2}{\kappa}\right) \left(\frac{-\pi p_\perp^2}{\kappa}\right), \quad (30)$$

where the transverse mass m_\perp is defined as $m_\perp^2 = m^2 + p_\perp^2$. The transverse momentum is now defined to be transverse to the string axis. This formula gives flavour-independent Gaussian p_\perp -distribution for the created $q\bar{q}$ pairs.

As explained above the string fragmentation would only produce mesons in the final state, but we know that also baryons are created in the process. In the string fragmentation model baryon production is included by adding a probability that a diquark-antidiquark pair is created instead of a quark-antiquark pair when a string breaks.

The kinematics of each string breaking are determined iteratively. Since there is no natural ordering, the string breaking can be considered in any order and the answer obtained must be the same. One can start from the q leg and work one's way to the \bar{q} leg, or vice versa. This give a left-right symmetry of the string fragmentation. In the Lund model this is taken into account by defining a symmetric fragmentation function

$$f(z) \propto \frac{1}{z} (1-z)^a \exp\left(-\frac{bm_\perp^2}{z}\right) \quad (31)$$

to break the string into a hadron and a remainder system. Here z is the fraction of light-cone momentum p^+ given to the hadron in the string breaking, m_\perp is the transverse mass of the hadron and a and b are tuneable parameters of the model. For heavy quarks this is modified as

$$f(z) \propto \frac{1}{z^{1+bm_Q^2}} (1-z)^a \exp\left(-\frac{bm_\perp^2}{z}\right). \quad (32)$$

The process can be thought as follows: first start from the q -leg of a $q\bar{q}$ system and choose to consider the breaking to new $q'\bar{q}'$ pair closest to this leg. Now the breaking will produce a hadron $q\bar{q}'$ and a remainder system spanning from $q'\bar{q}$. Then the process is continued until the \bar{q} -leg is reached. A small detail here is that in equation (31) it is assumed that the mass of the remainder system is large. Thus some patching up is needed for the last two hadrons coming from a string. The patching up is done such that the place where it happens looks as closely like any other string break as possible.

One additional possibility one must consider is that a string can have such a low mass that it cannot break at all. In this case a single hadron is generated out of the string and if necessary energy and momentum are exchanged with other partons in the event.

After all the hadrons are produced, the short-lived ones can still decay before the set of final state particles in the simulation is obtained [125]

Cluster model

Instead of a string model HERWIG [126] uses a cluster model for hadronisation. The advantage of cluster models is that they require a smaller number of parameters than string models. The model is based on the preconfinement property of

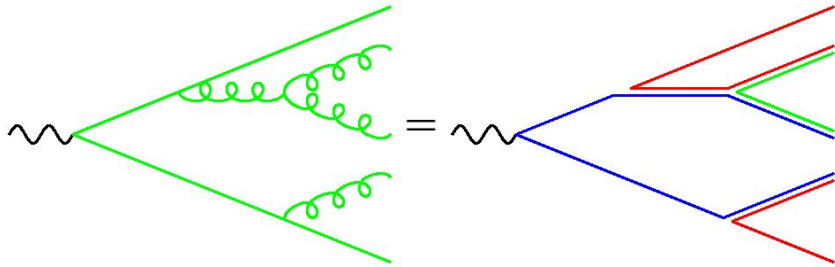


Figure 17: Colour structure of a parton shower to leading order in N_c . [127]

parton showers, i.e. the colour structure of the shower at any evolution scale Q_0 is such that colour singlet combinations of partons can be formed with an asymptotically universal invariant mass distribution. The invariant mass does not depend on the initial hard process scale Q , but only on Q_0 and the QCD scale Λ_{QCD} , when $Q \gg Q_0$ [127].

The cluster model starts from transforming all gluons non-perturbatively into $q\bar{q}$ pairs, which requires that the gluons get a mass, which must be at least twice the lightest quark mass. After the gluons are transformed into quarks, the adjacent colour lines can be clustered together to colour singlet states with mesonic quantum numbers. The momentum of these clusters is defined to be the sum of the momenta of the clustering partons. The principle of colour-preconfinement states that the mass distribution of these clusters is independent of the hard scattering process and its centre-of-mass energy [126].

Some of these initial clusters are too heavy to reasonably describe an excited state of a hadron. These must be split before they are allowed to decay. The cluster C is split if its mass fulfills the condition [126]

$$M_C^p \geq M_{\max}^p + (m_1 + m_2)^p, \quad (33)$$

where $m_{1,2}$ are the masses of the constituents partons of the cluster. M_{\max} and p are parameters given defined the model. These have to be chosen separately for clusters containing light, charmed and bottom quarks. When a cluster splits, a pair of light quarks is generated from the vacuum, which form two new clusters, both containing one quark from the original cluster and one from the newly generated pair. The splitting continues until no clusters with masses fulfilling the equation 33 remains.

When the clusters are light enough, they decay into final state hadrons. If the cluster mass is high enough for decaying into a baryon-antibaryon pair, it can undergo either a mesonic or a baryonic decay. The probabilities of mesonic and baryonic decays are parameters in the model [126] For a mesonic decay a quark-antiquark pair is created from the vacuum and for the baryonic decay a

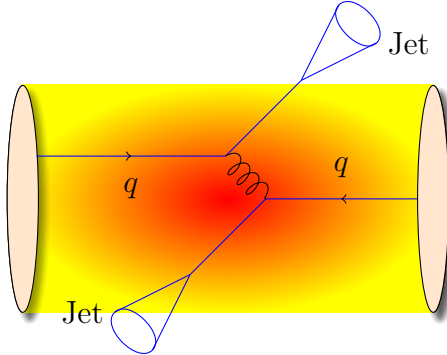


Figure 18: If hard scatterings happen in conjunction with QGP medium the produced jets must traverse the medium. Thus they are subject to interactions with the medium. Note that the dijet pair can be created anywhere within the medium volume and thus the two jets will have differing path lengths through the medium.

diquark-antidiquark pair is made. Then the exact decay products are chosen and the cluster decays isotropically in the rest frame of the cluster. If there are partons produced in the perturbative phase involved in the decay, they retain their original direction in the cluster rest frame, up to some Gaussian smearing. If the cluster mass is too low to decay into a pair of mesons, it decays into the lightest possible hadron and some energy and momentum is exchanged with the adjacent clusters. At the end we are left with the final state hadrons, some of which might still decay until the end of the simulation if they are very short-lived. [126]

1.4.5 Interactions between jet and medium

Let us now look at what happens to jet production in heavy-ion collisions. Figure 18 shows a dijet produced inside QGP medium. High momentum particles are very rare and they are only produced in the initial collisions. In a heavy ion collision, where a QGP medium is formed, the hard scattered quarks and gluons are expected to interact strongly with the medium due to their colour charges and thus lose energy, either through collisions with medium partons, or through gluon bremsstrahlung [6]. This is referred to as jet quenching. Studying the modification of jets inside the medium gives another key approach to constraining the properties of QGP. Modification can be also observed in jet shapes, particle composition, fragmentation, splitting functions and many others.

Discovery of jet quenching via leading hadron suppression

First evidence of jet quenching comes from observing high p_T tracks, i.e. the leading hadrons of jets. In this picture jet quenching in heavy-ion collisions is usually quantified with the nuclear modification factor R_{AA} , which is defined as

$$R_{AA}(p_T) = \frac{(1/N_{AA}^{evt}) dN^{AA}/dp_T}{\langle N_{coll} \rangle (1/N_{pp}^{evt}) dN^{pp}/dp_T} \quad (34)$$

where dN^{AA}/dp_T and dN^{pp}/dp_T are the yields in heavy-ion and proton-proton collisions, respectively and $\langle N_{coll} \rangle$ is the average number of binary nucleon-nucleon collisions in one heavy-ion event. The number of binary collisions can be calculated from the Glauber model as shown in Section 1.3.1. From the point of view of direct production at high p_T a heavy-ion collision can be estimated relatively well to be only a series of proton-proton collisions. At low p_T this scaling breaks down as the determining factor in direct production is the number of participants.

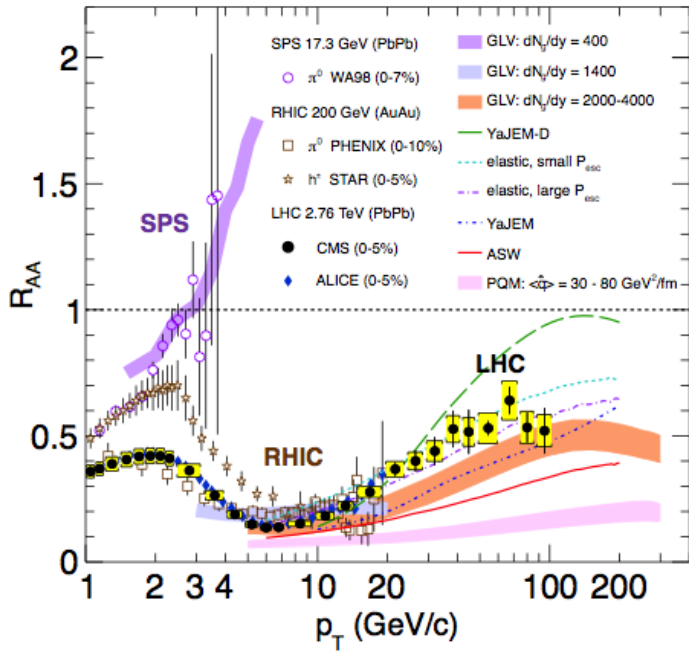


Figure 19: Measurements of the nuclear modification factor R_{AA} in central heavy-ion collisions at three different center-of-mass energies, as a function of p_T , for neutral pions (π^0), charged hadrons (h^\pm), and charged particles [131–135], compared to several theoretical predictions [69, 136–140]. The error bars on the points are the statistical uncertainties, and the yellow boxes around the CMS points are the systematic uncertainties. The bands for some of the theoretical calculations represent their uncertainties [141].

If the medium has no effect on high p_T particles the nuclear modification factor should be 1. As seen in Figure 19 R_{AA} at RHIC and LHC has been observed to be as low as 0.2, which is a clear signal that jet quenching is happening. However, the physical interpretation is not that 80 % of high momentum tracks disappear, rather they are shifted to smaller momenta. The relation between the shift in momentum and R_{AA} depends on the steepness of the dN/dp_T spectra. At LHC energies the spectrum is flatter and thus the same R_{AA} value as in RHIC requires a larger momentum shift, which results from the larger temperature of the medium at LHC.

The reaction plane dependence of inclusive particle R_{AA} demonstrates that energy loss is path length dependent [142], as expected from models. The path length can be affected by collisions centrality and system size. However, the temperature and lifetime of the QGP also changes with changing centrality and system size. Thus to study different path lengths the angle relative to the reaction plane gives the cleanest signal, as the properties of medium remain the same. Additionally it was concluded that there is no suppression for path lengths below $L = 2 \text{ fm}$. Similar indications about path length dependence are given by jet v_2 both at RHIC [143] and at LHC [144, 145].

QED Bremsstrahlung

Many of the energy loss models exploit the analogy between the QCD interaction of parton propagating through the coloured medium and the QED energy loss of electron propagating through material. An electron propagating through matter loses its energy by photon Bremsstrahlung radiation. In the simplest case, each individual scattering center results in a single emission of a photon. This is known as the Bethe-Heitler regime [146]. The energy spectrum of radiated photons dN/dE is, in this case, proportional to $1/E$. However, the Bremsstrahlung photon, can be radiated only when the distance between the scattering centers is larger than the formation length. In the limit, when the scattering centers are closer than the formation length, the Bremsstrahlung process is suppressed. This phenomenon is known as the Landau-Pomeranchuk-Migdal (LPM) [147, 148] suppression. The radiated spectrum in this regime is proportional to $1/\sqrt{E}$.

Lower energy photons are further suppressed by the destructive interference leading to the suppression of Bremsstrahlung photons of $E < \gamma\omega_p$, where ω_p is the plasma frequency of the radiator. This is known as Dielectric suppression. The photon energy distribution in this regime is proportional to the energy of the photon. A schematic view of the effect of these three regimes is shown in Figure 20.

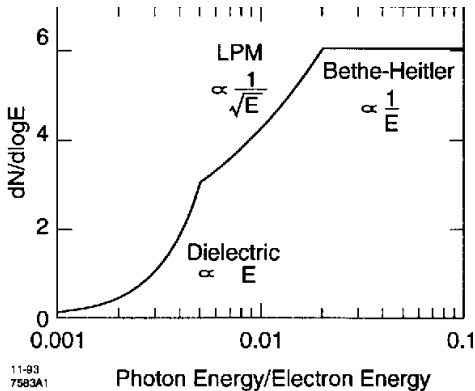


Figure 20: The expected bremsstrahlung spectrum for an electron propagating through material. [149].

QCD

In QCD the radiative energy loss mechanism is given in terms of the transport coefficient $\langle \hat{q} \rangle$, which describes the average momentum transfer between the medium and parton [150]. The exact definition of this depends on the theoretical formalism used to describe the energy loss mechanism.

The simplest energy loss process is elastic QCD scattering off the medium partons. In elastic scatterings the recoil energy of the scattered partons are absorbed by the thermal medium, which reduces the energy of the initial parton. The mean energy loss from elastic scatterings can be estimated by

$$\langle \Delta E \rangle_{\text{el}} = \sigma \rho L \langle E \rangle_{\text{1scatt}} \propto L, \quad (35)$$

where σ is the interaction cross section and $\langle E \rangle_{\text{1scatt}}$ is the mean energy transfer of one individual scattering [151]. This assumption holds if the mean energy is independent of the total energy of the parton (E). The transport coefficient of elastic scattering, $\langle \hat{q}_{\text{el}} \rangle = \langle \Delta E \rangle / L$, is defined as the mean energy loss per unit path length.

Another energy loss mechanism is medium-induced radiation. In QCD this radiation is mainly due to the elementary splitting processes, $q \rightarrow qg_r$ and $g \rightarrow gg_r$. Assuming that the parton is moving with the speed of light radiation energy loss can be estimated by

$$\langle \Delta E \rangle_{\text{rad}} \propto T^3 L^2, \quad (36)$$

where L is the length of the medium and T is its temperature [152]. The different exponents of L in equations 35 and 36 indicate that radiative energy loss is dominant over elastic energy loss.

There are several models that attempt to describe the nature of the energy loss mechanism. The most used models can be divided into four formalisms.

In the Gyulassy-Levai-Vitev (GLV) [153] opacity expansion model the radiative energy loss is considered on a few scattering centers N_{scatt} . The radiated gluon is constructed by pQCD calculation as summing up the relevant scattering amplitudes in terms of the number of scatterings. Another approach into opacity expansion is the ASW model by Armesto, Salgado and Wiedermann [154].

Thermal effective theory formulation by Arnold, Moore and Yaffe (AMY) [155] uses dynamical scattering centers. It is based on leading order pQCD hard thermal loop effective field theory. This model assumes that because of the high temperature of the plasma the strong coupling constant can be treated as small. The parton propagating through the medium will lose energy from soft scatterings and hard scatterings.

The above models calculate the energy loss while the parton propagates through the medium, focusing on the pQCD part. The higher twist (HT) approach by Wang and Guo [156] implements the energy loss mechanism in the energy scale evolution of the fragmentation functions.

The last category is formed by the Monte Carlo methods. The PYTHIA event generator [157] is widely used in high-energy particle physics. Two Monte Carlo models based on PYTHIA describing the energy loss mechanism are PYQUEN [158] and Q-Pythia [159]. Other Monte Carlo models include JEWEL [160] and YaJEM [161].

1.4.6 New paradigm of jet Quenching

As described in the previous sections the first indications of jet quenching, such as R_{AA} , looked essentially at the leading hadrons of jets, the hard part, ignoring the soft scale part of jet phenomena. However, experimental methods have since improved; jet reconstruction algorithms have become reliable in the LHC era. Instead of the leading hadron we can study the entire jet shower and its structure. In jet observables one must consider what happens to the lost energy. Radiated gluons may end up being clustered with the jet, depending on the radiation angle, the parameters of jet reconstruction and whether the gluon reaches equilibrium with the medium or not. Thus the suppression on the jet level is expected to be smaller. Figure 21 shows jet R_{AA} in central Pb–Pb collisions measured by ALICE,ATLAS and CMS and indeed jet R_{AA} is about 0.5 instead of 0.2.

Thus, on the level of the reconstructed jet, energy loss manifests itself as broadening and softening of the jet. This is seen for example in jet-hadron correlations. Figure 22 shows $\Delta\eta$ correlations with the leading jet. $\Delta\phi$ correlations have similar trends. Jets in Pb–Pb are observed to be broader, with the greatest increase in the width for low momentum associated particles. This is consistent with expec-

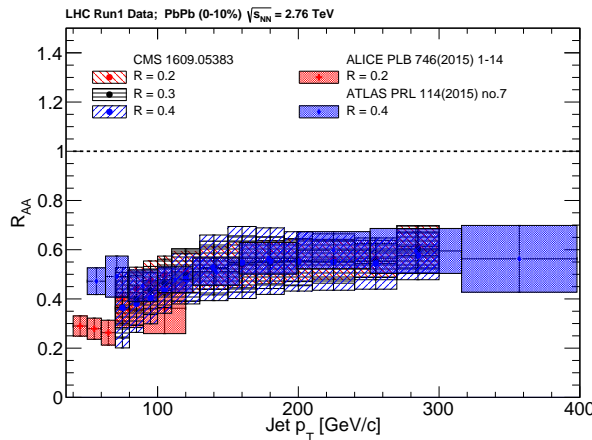


Figure 21: Reconstructed anti- k_T jet R_{AA} from ALICE [162] with $R = 0.2$ for $|\eta| < 0.5$, ATLAS [163] with $R = 0.4$ for $|\eta| < 2.1$, and CMS [164] with $R = 0.2, 0.3$ and 0.4 for $|\eta| < 2.0$. The ALICE and CMS data are consistent within uncertainties while the ATLAS data are higher. The experiments use slightly different methods in selecting jets and subtracting the underlying event contribution. Compared to ALICE and CMS the ATLAS technique could impose a survivor bias and lead to a higher jet RAA at low momenta. Figure from [6]

tations from partonic energy loss. These studies found that the subleading jet was broadened even more than the leading jet, indicating a bias towards selecting less modified jets as the leading jet. Jet hadron correlations have also been studied at RHIC with similar conclusion [165].

Phase-space view of the medium modified parton cascade

The new paradigm in jet quenching in heavy-ion collisions involves multi-scale problems [167, 168]. The elementary scattering and the subsequent branching process down to non-perturbative scales are dominated by hard scales in the vacuum as well as in the medium. Soft scales, of the order of the temperature of the medium, characterise the interactions of soft partons produced in the shower with the QGP. Soft scales also rule hadronisation, which is expected to take place in vacuum for sufficiently energetic probes, even though some modifications can persist from modifications of colour flow [169–171]. Understanding the contributions from the different processes to the jet shower evolution in medium and their scale dependence is crucial to constrain the dynamics of jet energy loss in the expanding medium, the role of colour coherence [172], and fundamental medium properties like temperature dependent transport coefficient [173, 174].

Let us now look at medium modification of jets in a $\log(p) - \log(\theta)$ plane

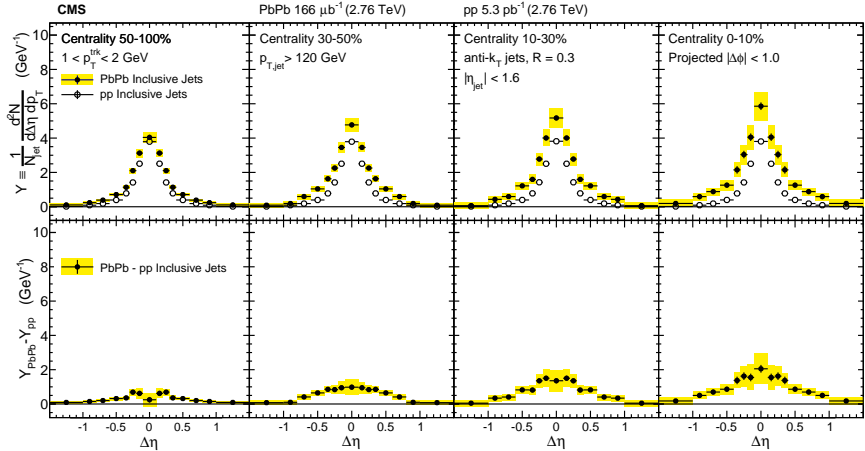


Figure 22: Measurement by CMS [166]. Symmetrized $\Delta\eta$ distributions correlated with Pb–Pb and pp inclusive jets with $p_T > 120$ GeV are shown in the top panels for tracks with $1 < p_T < 2$ GeV. The difference between per-jet yields in Pb–Pb and pp collisions is shown in the bottom panels. These measurements indicate that the jet is broadened and softened, as expected. The effect is stronger in more central collisions. $\Delta\phi$ correlations have similar trends.

as shown in [167]. The different momentum and angular scales are subject to different physical phenomena. Figure 23 shows the relevant medium modification phenomena for different regions of the phase space at time t , when a jet propagates through a thermal cloud of temperature T . As in practice jets propagate over a finite path-length L in QCD matter, Figure 23 can be taken as a representation of the distribution of partonic jet fragments at moment $t \approx L$, when the jet escapes the medium. [167]

The region marked as DGLAP is dominated by the primary vacuum splittings explained in section 1.4.2. This region is determined by $\theta > \theta_{\text{vac}}$ with

$$\theta_{\text{vac}} \propto 1/\sqrt{p_T}. \quad (37)$$

Medium-induced parton branching fills the $\log p$ - $\log \theta$ -plane from the bottom up (in p) and from the inside out (in θ). This is because transverse momentum is acquired by Brownian motion in the medium, $k_\perp^2 \propto \hat{q}t$. The formation time constraint $t \geq p/k_\perp^2 \approx p/\hat{q}t$ implies that medium-induced quanta can be formed in the region $p \leq k_{\text{form}}$ where

$$k_{\text{form}}(t) = \hat{q}t^2. \quad (38)$$

For these splittees to survive without further splittings they must have

$$p \geq k_{\text{split}} \approx \alpha_s^2 k_{\text{form}}(t) \approx \alpha_s^2 \hat{q}t^2. \quad (39)$$

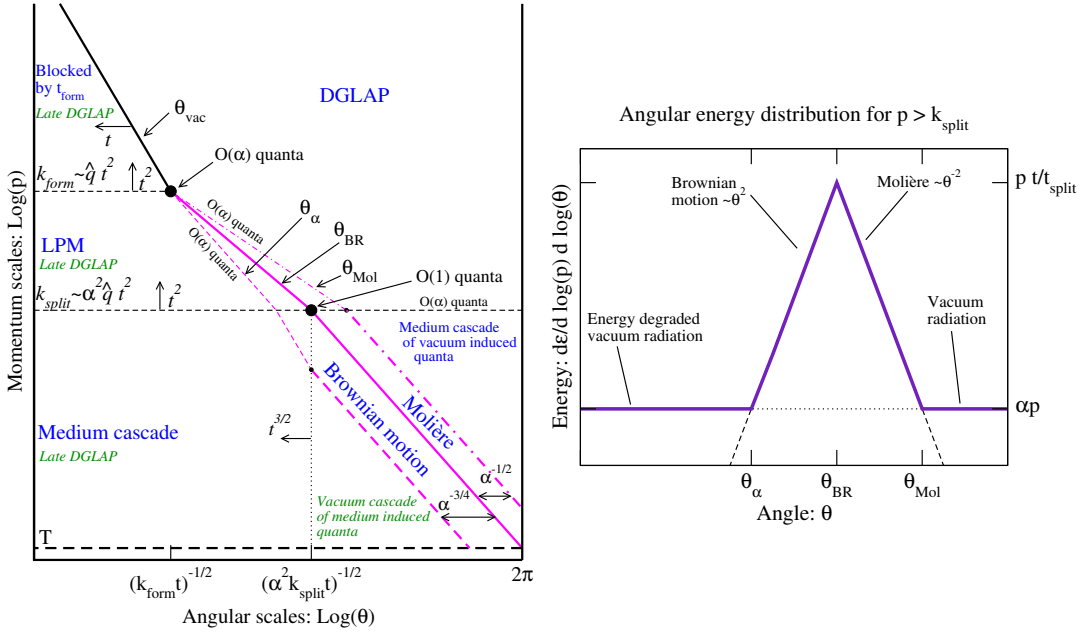


Figure 23: *Left:* Phase space view of dominant contributions in a medium-modified parton cascade. *Right* The distribution of energy as a function of angle for a fixed momentum with $p > k_{\text{split}}$. Large angular scales $\theta > \theta_{\text{Mol}}$ are dominated by DGLAP vacuum radiation from the leading parton at the scale Q . At $\theta < \theta_\alpha$ the energy density is dominated by vacuum radiation of the leading parton after it has degraded its energy propagating through the medium. Areas $\theta_\alpha < \theta < \theta_{\text{BR}}$ and $\theta_{\text{BR}} < \theta < \theta_{\text{Mol}}$ are dominated by Brownian motion and rare large angle (Molière) scatterings with medium partons [167].

Thus the region marked as LPM in Figure 23 is filled by the primary medium-induced branchings. Fragments with $p \leq k_{\text{split}}$ will have time to split further. An approximately equal splitting where both splittees get momentum $p/2$ from the parent will degrade energy the most. These splittees will undergo the next splitting in an even shorter time scale producing even softer fragments. Momenta can continue cascading all the way to the thermal scale T of the medium within the same time scale within which the first splitting occurred. Thus filling the region marked as Medium cascade in Figure 23. Similarly splittees from vacuum radiation can cascade inside the medium when they have $p \leq k_{\text{split}}$, filling the bottom right corner of the $\log p$ - $\log \theta$ -plane.

The angular distribution of the medium-induced radiation is driven by two mechanisms; Multiple soft scatterings give rise to transverse Brownian motion, which determines the distribution at small angles. The typical angle reached in the LPM region is

$$\theta_{\text{BR}}(p) \approx \frac{\sqrt{\hat{q}t}}{p}, \text{ for } k_{\text{form}} > p > k_{\text{split}}, \quad (40)$$

while in the medium cascade region of the phase space this becomes

$$\theta_{\text{BR}}(p) \approx \left(\frac{T}{p}\right)^{\frac{3}{4}} \quad (41)$$

Large angular scales cannot be reached by Brownian motion, but can arise from rare large angle scatterings with partons in the medium, described first by Molière [175]. The result is that medium-induced radiation is predominantly located in the bands marked as Brownian motion, where $\theta_\alpha < \theta < \theta_{\text{BR}}$, and Molière, where $\theta_{\text{BR}} < \theta < \theta_{\text{Mol}}$ in Figure 23.

The hard parton will naturally continue radiating after it leaves the medium. As there is no longer kinematic limits set by the time scale, the vacuum radiation can extend to smaller angular scales in the phase space. The results is that the regions, where $\theta < \theta_\alpha$, marked as Late DGLAP in Figure 23 will be dominated by the late time vacuum radiation. Naturally also the splittees from medium-induced radiation will undergo the late stage vacuum radiation phase, filling the triangular region with small p and $\theta < \theta_\alpha$.

Influence of jet on medium

Energy loss of hard partons is well established by experimental observations. Naturally energy can't just disappear, but is transferred to daughter partons or the medium. For radiation that stays inside the jet cone energy loss manifests itself as softening and broadening. If a daughter parton loses energy and becomes equilibrated with the medium it may no longer be correlated with the parent parton. This energy would then be distributed at distances far from the jet cone. There is some evidence for out-of-cone radiation by CMS [176], but the interpretation is not clear. Other possible phenomena include the mach cone and Molière scattering, but there is no experimental evidence for these. Evidence for all of these effects is difficult to find as the underlying event gives already a large and fluctuating background. Additionally its unclear how this energy would be different from the underlying event [6].

1.5 QGP in Small systems

After the existence of QGP in heavy-ion collisions has been established, attention has been turned to small systems. Proton-proton (pp) and proton-Lead ($p\text{-Pb}$) collisions have been studied at LHC and RHIC has studied a host of different collision systems; namely proton-gold ($p\text{Au}$) [177], deuteron-gold ($d\text{Au}$) [178–181] and helium³-gold (He^3Au) [182] collisions starting from 2000.

Already before the era of modern colliders, collective behaviour in proton-proton collisions was considered by names like Heisenberg, Fermi and Bjorken [7]. Eventually there were some experimental searches of QGP in pp and $p\bar{p}$ collisions in E735 at Tevatron [183] and MiniMAX [184]. However no conclusive evidence was found.

In the early years of RHIC these small systems were mostly considered as control measurement, for example in constraining nuclear modified parton distribution functions (nPDFs) that determine the initial gluon distributions that determine the first epoch of heavy-ion collisions [185, 186].

In 2010 ultrahigh-multiplicity pp collisions were studied at CMS [187]. The study found that particles had a weak but clear preference to be emitted along a common transverse ϕ angle across all rapidities [188]. This seemed like behaviour were similar to AA collisions, but it was argued that it could as well come from momentum correlations present in the earliest moments of the collision.

In 2012 LHC ran its first $p\text{-Pb}$ data taking period. Around the same time $d\text{Au}$ data was re-examined at RHIC. Now it was revealed that most of the flow signatures attributed to hydrodynamic expansion in AA collisions also existed in smaller systems.

1.5.1 Collective phenomena

The most rugged analysis of collective behaviour concerns the two (or more) particle correlations, often parametrised via the relative azimuthal angle and pseudorapidity differences, $\Delta\phi$ and $\Delta\eta$ respectively. Figure 24 shows two-particle correlations measurements in Pb-Pb , $p\text{-Pb}$ and pp collisions at the LHC [189]. In Pb-Pb collisions long-range correlations dominate over short-range phenomena. This shows in the two ridges at $\Delta\phi = 0$ and $\Delta\phi = \pi$. At $\Delta\phi \approx \Delta\eta \approx 0$, there is a peak coming from single jet fragmentation. Since the away-side jet can be spread out in $\Delta\eta$, this contribution disappears when compared to the flow contribution at the away side ridge. In $p\text{Pb}$, and pp the near side peak is more distinguished and the away-side jet contribution starts to show. Still, one can see long-range correlations that seem like flow-like collective behaviour in both systems.

In addition to the two particle correlations, correlations have been observed in the form of v_n coefficients both at LHC [190] and at RHIC [177]. The results have

also been described with hydrodynamical models, although the applicability of said models might be questionable, because of the large Reynolds numbers in small systems [191, 192]. Figure 25 shows results for v_2 in different collisions systems at RHIC as measured by PHENIX and Figure 26 shows the eccentricities and the resulting hydrodynamic evolution in the systems. These different systems provide also different initial geometries. dAu collisions naturally have an ellipsoidal form, while a He³ collision has a triangular form and thus produces larger triangular flow, v_3 components.

Other observations that produce flow-like results include mass ordered v_2 coefficients [194] and higher order harmonics coming from fluctuations in the initial geometry [190]. Thus all the major collective flow phenomena observed in heavy-ion collisions have been also identified in small systems.

One open question is identifying the point the point, where flow-like correlations end. The question has proved challenging since low multiplicity events are dominated by non-flow phenomena. This makes observations in low multiplicity events model/method dependant. Different methods assess non-flow contributions differently. Thus some methods fail to observe a signal in cases, where others do and it is unclear whether this is true collective motion or it comes from non-flow contributions.

1.5.2 Absence of jet quenching

In A+A collisions, an important confirmation of the standard model comes from the energy loss of high p_T partons traversing the medium, as discussed in Section 1.4.5. Originally the interest in small systems was due to ruling out possible cold nuclear matter effects that might affect the results also in Pb-Pb. In 2003 the jet quenching effect was observed to disappear in d+Au collisions at RHIC [178–181]. This was taken as an indication that no QGP was created. Similarly at LHC no jet modification has been observed in pPb collisions. Figure 27

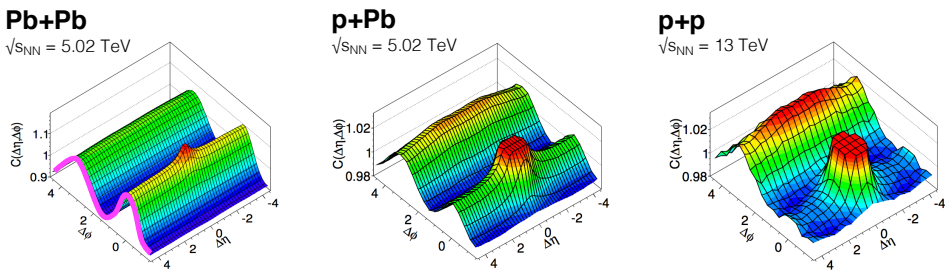


Figure 24: Two-particle correlation results in PbPb, pPb, and pp collisions at the LHC [189].

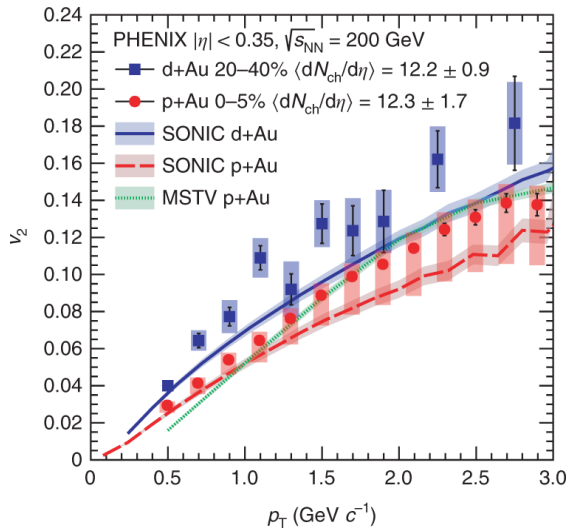


Figure 25: Comparison between hydrodynamic calculations and data from $p + \text{Au}$, $d + \text{Au}$ and ${}^3\text{He} + \text{Au}$ collisions [193]

shows the nuclear modification factor R_{pA} and v_2 in pPb collisions as measured at the LHC [195, 196].

Now the lack of jet modification seems surprising considering the multitude of flow observations supporting the existence of QGP in small systems. One possible

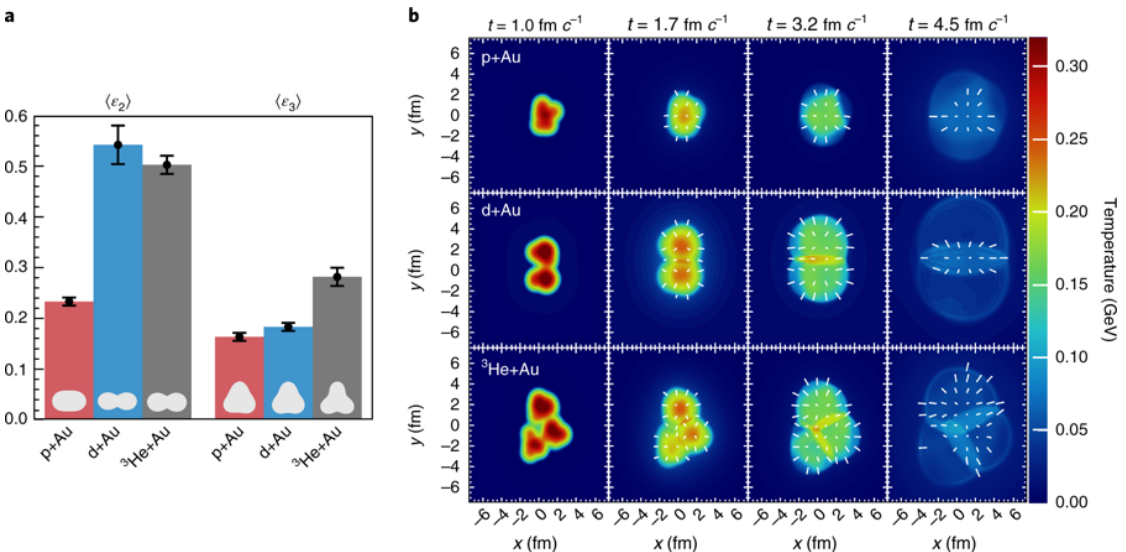


Figure 26: *left* Eccentricities in different systems. *right* Calculations of the initial energy density in small collision systems at RHIC and the resulting hydrodynamic evolution [193].

explanation is simply the size of medium. In PbPb collision partons traversing through the medium lose energy to the medium. If the medium is very small there is limited time for interaction with the medium. Reaction plane dependent R_{AA} measurements [142] in Pb–Pb collisions indicated that 2 fm could be the minimum path length required for energy loss.

Some calculations [197–199] indicate that there should be modification in the most central p–Pb collisions, but selecting these in the analysis is complicated [7]. In Pb–Pb collisions most of the particle production comes from the medium and thus the total multiplicity is a good indicator of centrality. However in p–Pb collisions the total multiplicity is smaller and is more strongly influenced by jet phenomena. Events with jets have naturally larger multiplicities and are more likely to be classified as central events.

So far the only observable indicative of jet quenching in pPb collisions is the high $p_T v_2$. In heavy-ion collisions this is not explained by hydrodynamics. Instead it is assumed to come from jet quenching with different path lengths through the medium in different directions. In Figure 27 ATLAS [196] and CMS [200] measurements of v_2 in pPb and PbPb collisions are shown. The pPb results seem to follow a very similar pattern. However, the non-flow effects in this high- p_T region are not fully under control, so the physical interpretation is still under debate.

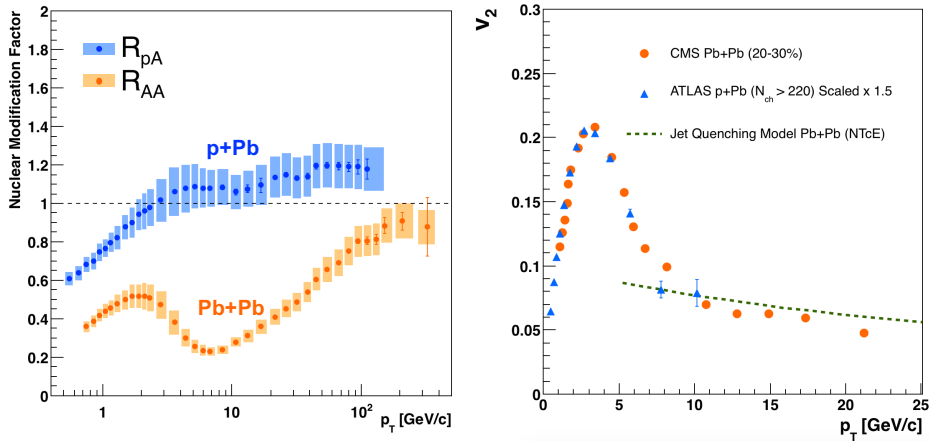


Figure 27: The nuclear modification factor R_{pA} in p–Pb collisions [195]. Compared to R_{AA} R_{pA} shows no sign of modification. *right* The v_2 coefficient as a function of p_T in Pb–Pb and p–Pb at the LHC [196, 200]. For shape comparison the p–Pb results have been scaled up by a factor 1.5. The green dotted curve [197] is from a jet quenching calculation where the anisotropy results from the directional dependence of the energy loss, rather than hydrodynamic flow.

1.5.3 Centrality determination in small systems

In lead-lead collisions the total multiplicity of the event is a good indicator of the geometric centrality of the collision [86]. In proton-lead collisions the connection between multiplicity and centrality is less clear [201]. In p-Pb collisions the impact parameter is only loosely correlated to N_{part} or N_{coll} . Hence, although one uses traditionally the term centrality to refer to these measurements, the relevant parameters are N_{part} and N_{coll} [201].

As in Pb–Pb collisions the Glauber model [82] is generally used to calculate geometrical quantities of p–Pb collisions. In this model, the impact parameter b controls the average number of participating nucleons N_{part} and the corresponding number of collisions N_{coll} . It is expected that variations of the amount of matter overlapping in the collision region will change the number of produced particles, and parameters such as N_{part} and N_{coll} have traditionally been used to describe those changes quantitatively, and to relate them to pp collisions. Figure 28 shows the measured V0A amplitude distribution in ALICE and the best NBD Glauber fit to the distribution [201].

The problem in p–Pb collisions is that fluctuations in multiplicity coming from for example hard scatterings are of the same order as the differences in multiplicity between centrality classes. In Pb–Pb collisions these multiplicity fluctuations have little influence on the centrality determination as the range of N_{part} or N_{coll} is large and both $P(M|N_{\text{part}})$ and $P(M|N_{\text{coll}})$ converge quickly to a Gaussian with

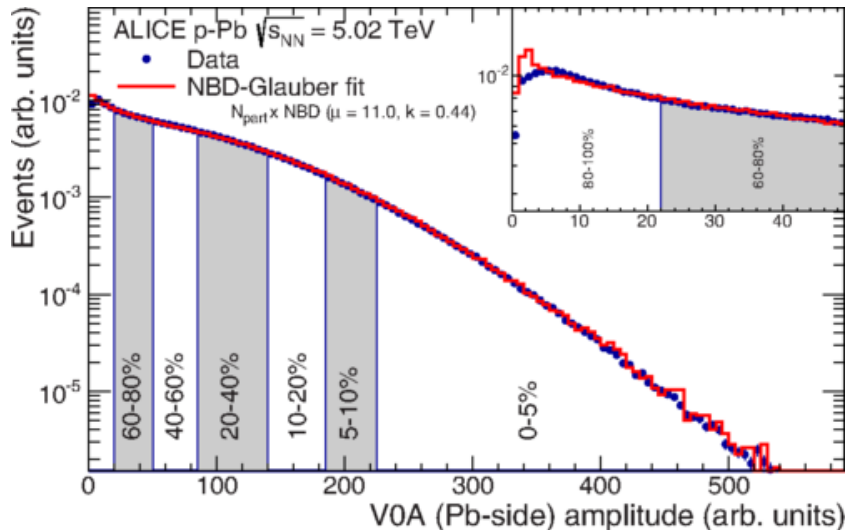


Figure 28: Distribution of the sum of amplitudes in the V0A hodoscopes (Pb-going), as well as the NBD-Glauber fit. Centrality classes are indicated by vertical lines. The inset shows a zoom-in on the most peripheral events. [201]

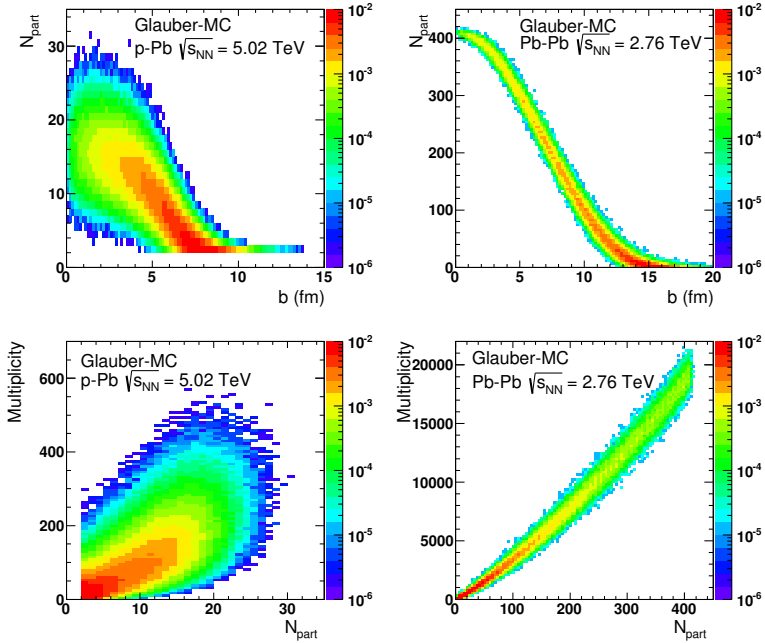


Figure 29: Top: Scatter plot of number of participating nucleons versus impact parameter; Bottom: Scatter plot of multiplicity versus the number of participating nucleons from the Glauber fit for V0A. The quantities are calculated with a Glauber Monte Carlo of p-Pb (left) and Pb-Pb (right) collisions. [201]

a small width relative to the range of $N_{\text{part}}/N_{\text{coll}}$. This is illustrated in Figure 29. In practice selecting high multiplicity in p-Pb one chooses not only large average N_{part} , but also positive multiplicity fluctuations leading to deviations from the binary scaling of hard processes. These fluctuations are partly related to qualitatively different types of collisions. High multiplicity nucleon-nucleon collisions show a significantly higher mean transverse momentum. They can be understood either as harder collisions with larger momentum transfer Q^2 or as nucleon-nucleon collisions where multiple parton-parton interactions (MPI) take place.

Of particular interest are estimators from kinematic regions that are causally disconnected after the collision. The measurement of a finite correlation between them unambiguously establishes their connection to the common collision geometry. Typically these studies are performed with observables from well separated pseudorapidity (η) intervals, e.g. at zero-degree (spectators, slow-nucleons, deuteron break-up probability) and multiplicity in the rapidity plateau.

One centrality selection that is argued not to induce a bias on the binary scaling of hard processes is provided by the energy measurement with the Zero Degree Calorimeters (ZDC) in ALICE, due to their large η -separation from the central

barrel detectors. They detect the "slow" nucleons produced in the interaction by nuclear de-excitation processes or knocked out by wounded nucleons [202].

Additional kinematic biases exist for events containing high- p_T particles, which arise from the fragmentation of partons produced in parton-parton scattering with large momentum transfer. Their contribution to the overall multiplicity increases with increasing parton energy and thus can introduce a trivial correlation between the centrality estimator and the presence of a high- p_T particle in the event. For very peripheral collisions, the multiplicity range that governs the centrality for the bulk of soft collisions can represent an effective veto on hard processes. For the nuclear modification factor this would lead to $R_{\text{pPb}} < 1$ [201].

2 Experimental Setup

2.1 CERN

The European Organization for Nuclear Research (CERN), established in 1954, operates the largest particle physics laboratory in the world. In 2019 CERN consists of 22 member states. Additionally CERN has contacts with a number of associate member states and various individual institutions. The laboratory, also referred to as CERN, itself is located near Geneva at the border of France and Switzerland employs about 2500 people. Additionally some 12000 visiting scientists from over 600 institutions in over 70 countries come to CERN for their research. [203]

The laboratory includes a series of accelerators, which are used to accelerate the particle beams used. A schematic view of the complex as of 2019 is shown in Figure 30. In the framework of this thesis the most important component is the Large Hadron Collider (LHC), the largest collider in the world. LHC will be discussed in more detail in Section 2.2. Other accelerators in the series are used to inject the particle beams into LHC, but they are also used in itself for various experimental studies.

The second largest accelerator is the super proton synchrotron (SPS). It is the final step before the particle beam is injected into LHC. Commissioned in 1976, it was the largest accelerator at CERN until the the Large Electron-Positron Collider (LEP) was finished in 1989. Originally it was used as a proton-antiproton collider and as such provided the data for the UA1 and UA2 experiments, which resulted in the discovery of the W and Z bosons [205]. At the moment there are several fixed target experiments utilising the beam from the SPS. These study the structure (COMPASS citeCOMPASS) and properties (NA61/SHINE [206]) of hadrons, rare decays of kaons (NA62 [207]) and radiation processes in strong electromagnetic fields (NA63 [208]). Additionally the AWAKE [209] and UA9 [210] experiments are used for accelerator research and development.

The third largest accelerator in CERN is the proton synchrotron (PS). Capable of accelerating beams up to an energy of 25 GeV PS provides the beam to SPS. Additionally PS has experiments for studying strong force (DIRAC [211]), the effect of cosmic rays on cloud formation (CLOUD [212]) and neutron-nucleus interactions (nTOF [213]).

Additionally PS provides the beam to the antiproton decelerator (AD), which uses the beam and a block of metal to produce antiprotons. These are then decelerated in AD into a useful low-energy beam, which is provided to a host of experiments studying the properties of antimatter.

PS gets proton beams from LINAC2 through BOOSTER and ion beams from LINAC3 through LEIR. From BOOSTER beams are also provided to the On-Line Isotope Mass Separator (ISOLDE). ISOLDE directs the beam into thick targets

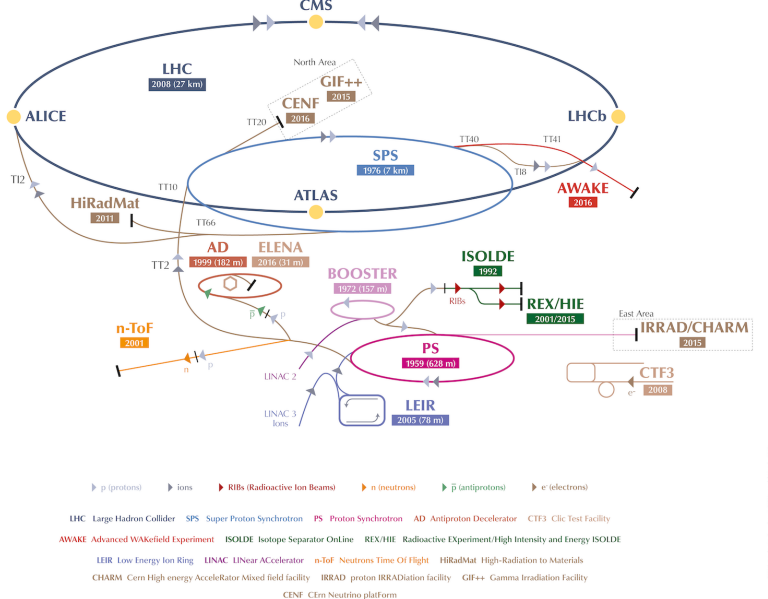


Figure 30: A schematic view of the accelerator complex at CERN. Before particles can be injected into the LHC they require a series of accelerators with increasing size. Until 2018 protons started their journey in LINAC2 (Linear Accelerator) and continue through the Booster, Proton Synchrotron (PS) and Super Proton Synchrotron (SPS). Between 2019 and 2020 LINAC2 will be replaced by LINAC4 [204]

to produce low energy beams of radioactive nuclei. These beams are used to study the properties of even the most exotic of atomic nuclei in a host of experiments.

More information of the various experiments at CERN can be found online in [214].

2.2 Large Hadron Collider

The Large Hadron Collider (LHC) [215, 216] with its circumference of 26.7 km is the largest accelerator at CERN and the largest particle collider ever built. The LHC is designed to accelerate protons up to an energy of 8 TeV and lead ions up to center of mass energies of 5.02 TeV per nucleon. The design luminosity of the LHC is $10^{34} \text{ cm}^{-2}\text{s}^{-1}$. In 2017 it achieved a record peak luminosity of $2 \cdot 10^{34} \text{ cm}^{-2}\text{s}^{-1}$ which was also reached in 2018. For lead beams luminosities of up to $6 \cdot 10^{27} \text{ cm}^{-2}\text{s}^{-1}$ were reached in 2018. All this is achieved with a ring consisting of 1232 superconducting dipole magnets that keep particles in orbit.

The LHC receives beams with energies of 450 GeV from the SPS. In the LHC the particles are accelerated through the use of radio-frequency (RF) cavities. Electromagnetic waves become resonant and build up inside the cavity. As they consist of electromagnetic waves, the field in the RF cavity oscillates. Charges passing through the cavity feel the overall force and are pushed forward along the accelerator. Particles must enter the cavity at the correct phase of oscillation to receive a forward push. When timed correctly, the particles will feel zero accelerating voltage when they have exactly the correct energy. Particles with higher energies will be decelerated and particles with lower energies will be accelerated. This focuses particles in distinct bunches. The RF oscillation frequency at the LHC is 400.8 MHz. Thus RF "buckets" are separated by 2.5 ns. However only 10 % are actually filled with particles, so the bunch spacing in the LHC is 25 ns, at a bunch frequency of 40 MHz. [215]

With 7 TeV proton beams the dipole magnets used to bend the beam must produce a magnetic field of 8.33 T. This can be only achieved through making the magnets superconducting, which requires cooling them down with helium to a temperature of 1.9 K. The 1232 dipole magnets make up roughly 2/3 of the LHC circumference. The remaining part is made up of the RF cavities, various sensors and higher multipole magnets used to keep the beam focused. The most notable of these are the 392 quadrupole magnets. [215]

The LHC is divided into octants, where each octant has a distinct function. Octants 2 and 8 are used to inject beam into the LHC from SPS. The 2 beams are crossed in octants 1,2,5 and 8. The main experiments are built around these crossing points. Octants 3 and 7 are used for beam cleansing. This is achieved through collimators that scatter particles with too high momentum or position offsets off from the beam. The RF cavities used for acceleration are located in octant 4 and octant 6 is used for dumping the beam. The beam dump is made up of two iron septum magnets, one for each beam, that will kick the beam away from machine components into an absorber when needed.

2.2.1 LHC experiments

As of 2018 there are four main experiments at the LHC; ALICE [217], ATLAS [218], CMS [219] and LHCb [220] and three smaller ones LHCf [221], TOTEM [222] and MoEDAL [223]. ALICE will be covered in detail in Section 2.3.

ATLAS (A Toroidal LHC ApparatuS) [218] and CMS (Compact Muon Solenoid) [219] are the two largest experiments at the LHC. They are both multipurpose experiments designed to be sensitive to many different possible new physics signals, such as extra dimensions and dark matter particles. The biggest discovery made by these so far is the discovery of the Standard Model Higgs boson, which was simultaneously published by the experiments in 2012 [224, 225].

The LHCb (LHC beauty) experiment [220] is made for studying the bottom (beauty) quark. Main physics goals of the LHCb include the measurement of the parameters of CP violation with decays of hadrons containing the bottom quark. One of the most important results published by LHCb is the first measurement of $B_s^0 \rightarrow \mu^+ \mu^-$ decay, which was found to be in line with the Standard Model.

In addition to the four large experiments there are three smaller experiments along the LHC ring. LHCf (LHC forward) [221] is located at interaction point 1 with ATLAS. It aims to simulate cosmic rays by the particles thrown forwards by the collisions in ATLAS.

TOTEM (TOTal Elastic and diffractive cross section Measurement) is located near the CMS experiment at point 5. This allows it to measure particles emerging from CMS with small angles. The main goals is to measure the total, elastic and inelastic cross-sections in pp collisions [222].

The MoEDAL (Monopole and Exotics Detector At the LHC) experiment [223] is located at the interaction point 8 together with the LHCb experiment. MoEDAL tries to measure signatures of hypothetical particles with magnetic charge, magnetic monopoles.

2.3 ALICE

ALICE (A Large Ion Collider Experiment) [226] is the dedicated heavy ion experiment at the LHC. ALICE was designed to cope with the expected very high multiplicity environment of heavy ion collisions. The design allows measurement of a large number of low momentum tracks. The different detector subsystems are optimised to provide high momentum resolution and excellent particle identification capabilities over a broad range of momentum.

A schematic view of the ALICE detector in 2018 is presented in Figure 31. This section will go through the composition of ALICE as it has been during run 2 between 2014 and 2018. The detector will go through significant upgrades during Long Shutdown 2 (LS2) in 2019-2020.

As in all the major high energy physics experiments the positioning of the detectors follows a layered structure. Closest to the interaction point are the tracking detectors. The main task of these detectors is to locate the position of the primary interaction vertex accurately and to record the tracks of charged particles. To achieve this they need a very good spatial resolution close to the interaction point. Tracking detectors do not significantly alter the tracks of traversing particles. Thus they can be located in the innermost layers.

Calorimeters are designed to stop particles hitting them and thus use the absorption to measure the energy of the particles. Thus they must be located behind the tracking detectors. ALICE has two separate calorimeter systems, the electromagnetic calorimeters measure mainly electrons and photons, while the muon

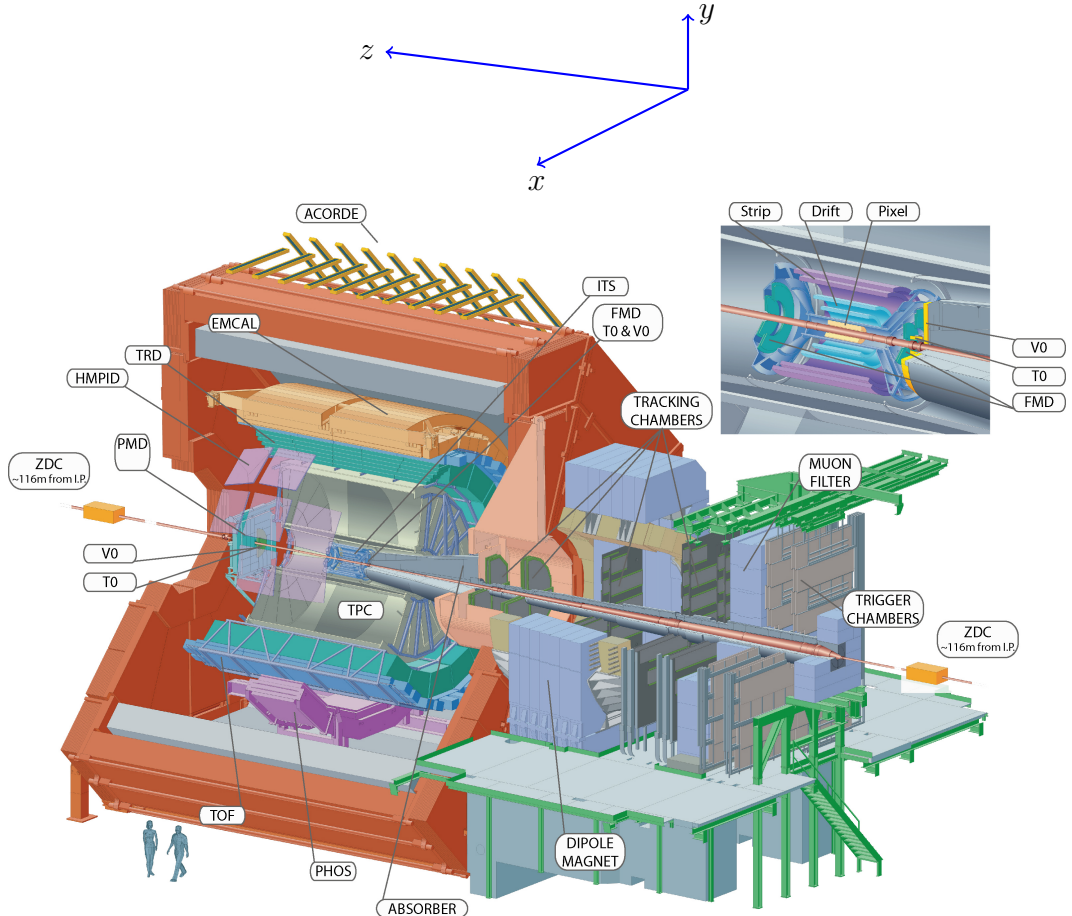


Figure 31: Schematic view of the ALICE detector with the definition of coordinates. The positive direction of *z* is also referred to as the A side and the negative direction as the C side

detection system measures muons.

2.3.1 Tracking

The main design guideline for the tracking detectors in ALICE was the requirement to have good track separation and high granularity in the high multiplicity environment of heavy ion collisions. Before the LHC started heavy ion runs the wildest estimates put the particle density at 8000 charged particles per unit of rapidity [226]. In reality the particle density turned out to be significantly smaller, about 1600 charged particles per rapidity unit [227].

The main tracking detector in ALICE is the Time Projection Chamber (TPC) [228]. TPS is discussed in more detail in Section 2.3.2

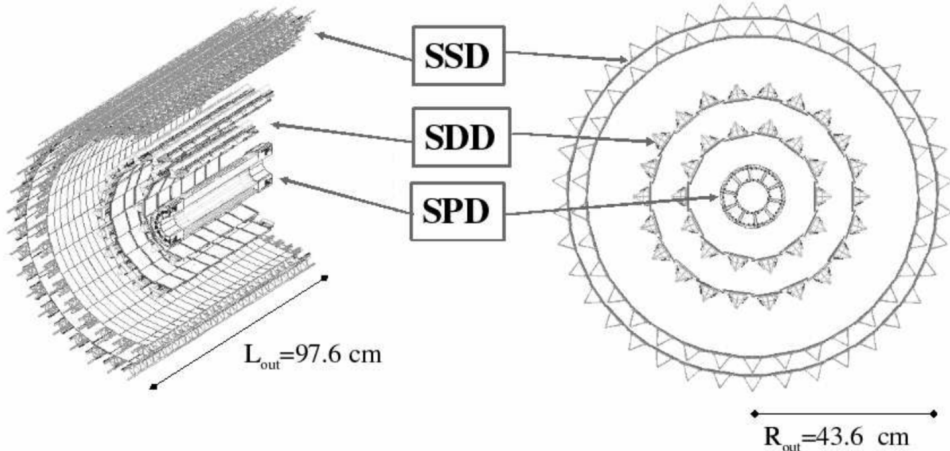


Figure 32: Schematic view of ALICE Inner Tracking System

Between TPC and the beam pipe there is an array of six layers of silicon detectors, called the inner tracking system (ITS) [229]. The main tasks of the ITS are to locate the primary vertex with a resolution better than $100\ \mu m$, to reconstruct the secondary vertices from decaying particles, to track and identify particles with momenta below 200 MeV and to compliment the momentum and angle measurements of TPC. During long shutdown 2 in 2019-2020 the entire ITS will be replaced [230]. As of 2018 the two innermost layers are made of the silicon pixel detector (SPD). As it is the closest detector to the interaction point it requires a very high spatial resolution. Thus the choice of pixel technology is natural. In heavy ion collisions the particle density is around 50 particles per cm^2 .

The next two layers together are the silicon drift detector (SDD). The layers are made out of homogeneous neutron transmutation doped silicon, that is ionized when a charged particle goes through the material. The generated charge then drifts to the collection anodes, where it is measured. The maximum drift time in SDD is about $5\ \mu s$. This design gives very good multi-tracking capabilities and provides two out of the four dE/dx samples in the ITS.

The two remaining layers in the ITS are the silicon strip detector (SSD). The strips work in a similar way as silicon pixels, but by itself one layer only provides good resolution in one direction. Combining two crossing grids of strips provides 2 dimensional detection. Each charged particle will hit two intervening strips. The position of the hit can be deduced from the place where the strips cross each other.

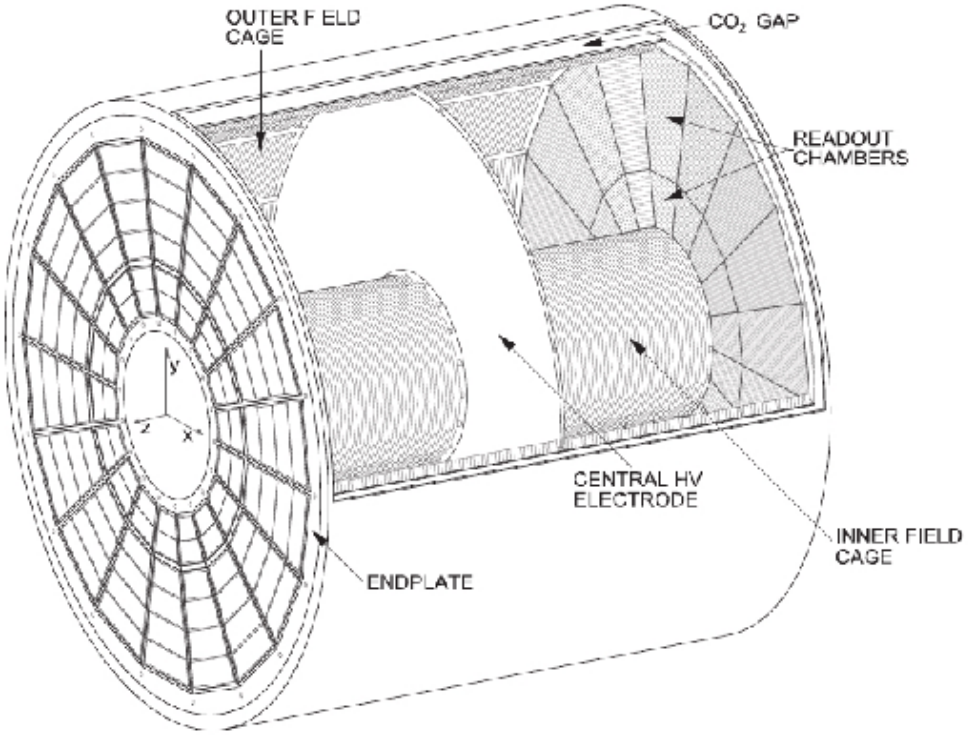


Figure 33: Schematic view of ALICE Time Projection Chamber

2.3.2 TPC

The time projection chamber (TPC) is a cylindrical detector filled with 88 m^3 of Ne – CO₂ (90/10 %) gas mixture. The gas is contained in a field cage that provides an uniform electric field of 400 V/cm along the z-axis. The gas content and field strength have been chosen for optimised charge transport, signal amplification and transparency for traversing particles [231]. Charged particles traversing through the TPC volume will ionise the gas along their path. This liberates electrons that drift towards the end plates of the cylinder. A schematic of the TPC is shown in Figure 33.

The field cage is separated into two detection volumes by the central high voltage electrode. Both sides have a drift length of 2.5 m and inner and outer diameters of 1.2 m and 5 m respectively. To provide the uniform electric field of 400 V/cm the central electrode must provide a potential of 100 kV. The maximum time required for electrons to drift through the chamber is about $90\text{ }\mu\text{s}$.

When electrons reach the end of the main cylinder they enter the readout chambers. The readout section of both sides consists of 18 outer chambers and

18 inner chambers. Each of them is made of multiwire proportional chambers with cathode pad readouts. This design has been used in many TPCs before. During LS2 in 2019-2020, the multiwire chambers will be replaced by Gas Electron Multipliers (GEMs, see Section 2.4).

2.3.3 Particle identification

One guiding principle in the design of ALICE was to achieve good particle identification (PID) over a large part of phases space and for several different particle types. In ALICE there are several detectors taking part in the identification of particles. In addition to the specific particle identification detectors, the general purpose tracking detectors can be used for identification through the use of specific energy loss dE/dx of charged particles traversing through a medium and the transition radiation emitted by charged particles when crossing the boundary between two materials.

Energy loss measurements are provided by the last four layers of the ITS detector, i.e. the SDD and the SSD, thanks to their analog readout [232]. ITS can provide particle identification in the low p_T region, up to 1 GeV, and pions reconstructed in the standalone mode can be identified down to 100 MeV. Similar to ITS the TPC detector provides specific energy loss measurements. TPC can identify charged hadrons up to p_T 1 – 2 GeV as well as light nuclei, He3 and He4, providing the majority of PID information for ALICE.

One of the particle identification detectors is the transition radiation detector (TRD) [233]. Its main task is identifying electors with momenta larger than 1 GeV. Transition radiation is produced when highly relativistic particles traverse the boundary between two media having different dielectric constants. The average energy of the emitted photon is approximately proportional to the Lorentz factor γ of the particle, which provides an excellent way of discriminating between electrons and pion. ALICE TRD is made of a composite layer of foam and fibres. The emitted photons are then measured in six layers of Xe/CO₂ filled time expansion wire chambers.

The time of flight (TOF) detector [234] uses a very simple physics principle, i.e. calculating the velocity of the particle using the time of flight between two points. Combining this with the momentum of particle, obtained from the tracking detectors, one can calculate the mass of the particle, which identifies particles. The TOF detector consists of multigap resistive wire chambers. These are stacks of resistive plates spaced equally. They allow time of flight measurements in large acceptance with high efficiency and with a resolution better than 100 ps.

The third specific particle identification detector is the high momentum particle identification (HMPID) detector [235]. The HMPID uses a ring imaging Cherenkov counter to identify particles with momenta larger than 1 GeV. Particles moving

through a material faster than the speed of light in the material will produce Cherenkov radiation. The velocity of the particle determines the angle at which the radiation is emitted. Measuring this angle gives the velocity of the particle. This can be again used to calculate the mass of the particle, if the momentum is known. In HMPID the material is a liquid radiator and the photons are measured with multiwire proportional chambers in conjunction with photocathodes.

2.3.4 Electromagnetic Calorimeter

Calorimeters are designed to measure the energy of particles. Electromagnetic calorimeters specialise in detecting particles that interact primarily through the electromagnetic interaction, namely photons and electrons. They are required in many neutral meson [236] and direct photon [237] analyses. In addition the energy information enhances jet measurements [238], as some of jet fragments can't be detected with trackers.

ALICE has two electromagnetic calorimeters, the photon spectrometer (PHOS) [239] and the electromagnetic calorimeter (EMCal) [240]. PHOS is a homogeneous calorimeter that consists of scintillating PbWO_4 crystals, which generate a bremsstrahlung shower and produce scintillation light. The energy of the particle determines the amount of light produced. To improve the charged particle rejection, PHOS includes a charged particle veto detector (CPV) [239]. PHOS is built to have a very fine granularity, making it well suited for measuring direct photons and neutral mesons.

In comparison to PHOS, EMCal has coarser granularity, but a significantly larger acceptance, making it suitable for jet physics. The acceptance of EMCal in the azimuthal angle is $80 \text{ deg} < \phi < 187 \text{ deg}$. During long shutdown 1 in 2013-2015, EMCal was extended with the di-jet calorimeter (DCal) [241], giving an additional acceptance region of $260 \text{ deg} < \phi < 320 \text{ deg}$. This provides partial back-to-back coverage.

EMcal is segmented into 10 full size super modules (SM), 5 for A side and 5 for C side, and two 1/3 sized SMs, one for each side. This segmentation can be seen in Figure 34. Each SM is divided into 24 strips, each covering full η (24 towers) and 2 towers in η . Each strip is composed of 2×2 tower modules. Thus each full size super module includes 1152 towers and in total the EMCal is made up of 12288 towers.

The build of individual towers is shown in Figure 35. Each tower is built up from 76 alternating layers of 1.44 mm Pb and 77 layers of 1.76 mm polystyrene base injection moulded scintillator. The lead tiles produce the shower and scintillator tiles the light. Each tower scintillator is equipped with reflectors on all sides to provide better gain and keep the four towers inside one module isolated. The scintillation photons produced in the active volume of the tower are collected by 36

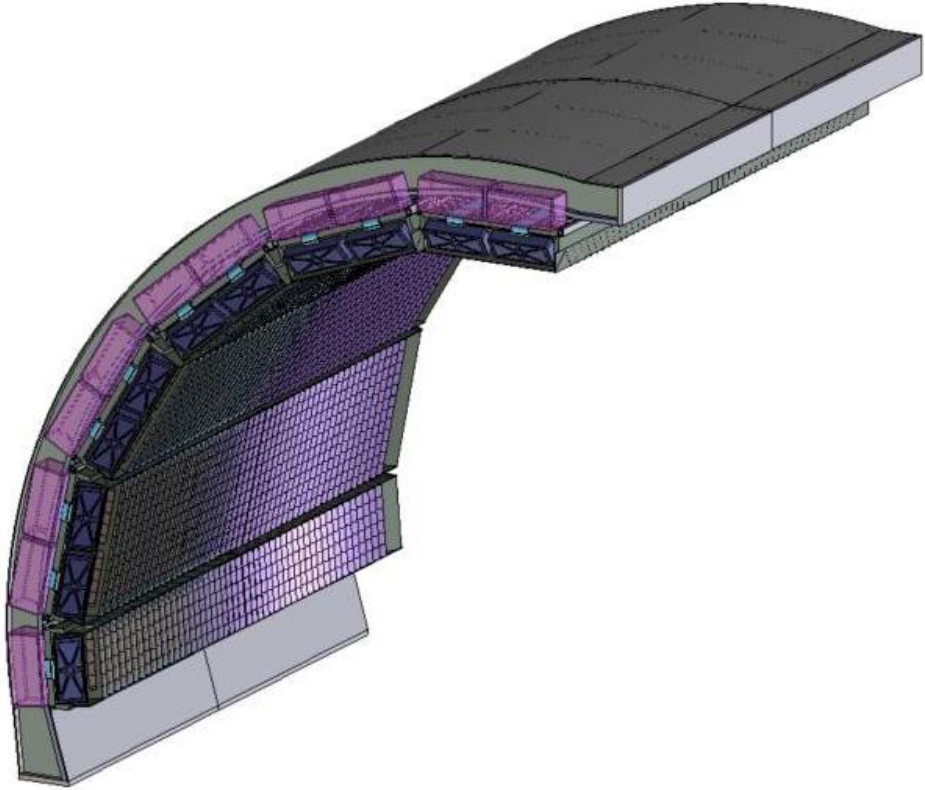


Figure 34: The EMCal detector arc, where the segmentation into 10 full size and 2 $\frac{1}{3}$ -sized (5 and 1 per side) supermodules can be seen.

longitudinally placed wave length shifting light guide fibres. The light is eventually directed to the Avalanche Photo Diodes (APD) for readout.

2.3.5 Forward and trigger detectors

ALICE includes a few small and specialised detectors of importance. The event time is determined with very good precision (< 25 ns) by the T0 detector [242]. T0 consists of two sets of Cherenkov counters that are mounted around the beam pipe on both sides of the interaction point. T0 gives the luminosity measurement in ALICE.

Another small detector in the forward direction is the V0 detector [242]. This consists of two arrays of segmented scintillator counters located at $-3.7 < \eta < -1.7$ and $2.8 < \eta < 5.1$. V0 is used as a minimum bias trigger and for rejection of beam-gas background. Particle multiplicity in the forward direction can be related to the event centrality. Thus V0 is the main detector used in centrality

Containment: 88 parts

- 1) Back (holes: 144 thru for fibers + springs + mech. support), 1
- 2) Compression (holes: 144 thru for fibers + springs), 1
- 3) Front Plate (holes: 144 thru for fibers + springs + mech. support), 1
- 4) 5) Plungers (10)
- 6) Belleville washers (75)

Tensioning and Insulation:**40 parts**

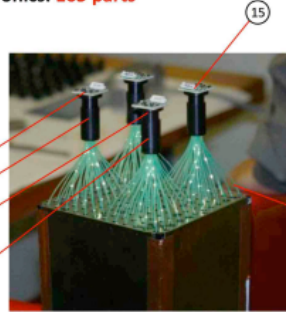
- 7) Stainless steel straps (4)
- 8) Screws (24)
- 9) Flanges (8)
- 10) Light tight stickers (4)

Sandwich:**538 parts**

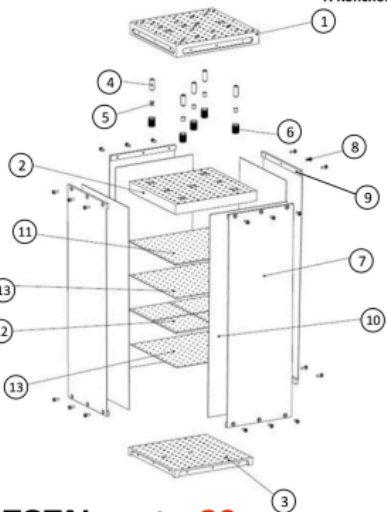
- 11) Lead tiles (76)
- 12) Scintillator tiles (308)
- 13) Bond paper sheets (154)

Readout and Electronics: 165 parts

- 14) WLS fibers (144)
- 15) APD (4)
- 16) CSP (4)
- 17) Light guides (4)
- 18) Mount (4)
- 19) Collars (4)
- 20) Diffuser (1)

**THE EMCAL Module Components**

F. Ronchetti

**TOTAL parts: 20****TOTAL components: 831**

Plus cabling, GMS and mech. supports

Figure 35: The exploded EMCAL tower view

determination in PbPb collisions.

The multiplicity measurement of V0 is complimented by the forward multiplicity detector (FMD) [242]. FMD includes five rings of silicon strip detectors that make up the FMD. FMD gives acceptance in the range $-3.4 < \eta < -1.7$ and $1.7 < \eta < 5.0$.

During long shutdown 2 in 2019-2020, V0 and T0 will be replaced by the Fast Interaction Trigger (FIT) detector [243]. For historical reasons elements of FIT are also referred to as V0+ and T0+. FIT will allow centrality, event plane, luminosity and interaction time determination in the continuous readout mode, that ALICE will operate in after 2020.

For photon multiplicity measurement ALICE has the photon multiplicity detector (PMD) [244]. PMD uses two planes of gas proportional counters with a cellular honeycomb structure. PMD gives the multiplicity and spatial distribution of photons in the region $2.3 < \eta < 3.7$.

On top of the ALICE magnet there is an array of 60 large scintillators called the ALICE cosmic ray detector (ACORDE) [245]. ACORDE is used as a trigger for cosmic rays for calibration and alignment.

The only hadronic calorimeters in ALICE are the zero degree calorimeters

(ZDC) [246], which are located next to the beam pipe in the machine tunnel about 116 m from the interaction point. There are two sets of calorimeters. One is made of tungsten, specialising in measuring neutrons, while the other, made of brass, is specialised in measuring protons. ZDC is meant to detect spectators, i.e. parts of the colliding ions that do not take part in the interaction. If there are more spectators, the collisions is likely to be more peripheral. Thus ZDC gives information about the centrality of the event especially in proton-lead collisions [201], but also in Pb–Pb collisions [86].

A new detector installed during the long shutdown 1 is the ALICE diffractive detector (AD) [247]. AD consists of two assemblies, one in each side of the interaction point, both made of two layers of scintillators. These assemblies are situated about 17 m and 19.5 m away from the interaction points. The pseudorapidity coverage is $-6.96 < \eta < -4.92$ and $4.78 < \eta < 6.31$. AD greatly enhances ALICE’s capability for diffractive physics measurements that require a large pseudorapidity gap. During long shutdown 2 AD will be updated and integrated as a part of the FIT detector.

2.3.6 Muon spectrometer

Outside the main magnet, ALICE has a spectrometer dedicated to measuring muons [248]. In heavy ion physics muons are mainly used to measure the production of the heavy quark resonances J/ψ , Ψ' , Υ , Υ' and Υ'' .

The muon spectrometer consists of three parts, the absorber, the muon tracker and the muon trigger. The absorber is meant to remove the hadronic background as efficiently as possible. After the absorber there are ten plates of thin cathode strip tracking stations with high granularity, the muon tracker. After the muon tracker there is a layer of iron to filter out any remaining particles, other than muons. The muon trigger is located behind this layer. The trigger consists of four resistive plate chambers.

2.3.7 Triggers

High energy physics experiments need triggers to select interesting physics. Experiments such as CMS and ATLAS at CERN look for extremely rare events. To produce these rare events LHC provides up to 40 million events each second. Such amounts can’t be recorded real-time as many detectors require some time for the readout, up to 1 ms/event in ALICE. Thus one uses triggers, i.e. a set of very fast hardware based decisions on which events are to be saved. Additionally one needs some confirmation that an event has even occurred to tell other detectors that the event needs to be recorded.

For ALICE the target event rates are 1 MHz for pp collisions, 0.1-2 kHz for Pb–Pb collisions and 200 kHz for the 2013 p–Pb collisions.

At ALICE the main system responsible for the trigger decisions is the ALICE Central Trigger Processor (CTP) [249]. The CTP generates three levels of hierarchical hardware triggers - Level 0, Level 1 and Level 2, (L0, L1 and L2 respectively) before an event is accepted and transmitted to the Data Acquisition system (DAQ). Afterwards additional software assessments are performed by the High Level Trigger (HLT).

Triggers can be roughly put into two classes, minimum bias triggers that make sure no empty events are recorded, and rare triggers that require specific signatures in ALICE detectors, such as large energy deposits in EMCal or two muons in the muon arm acceptance.

Minimum bias trigger

Several of the ALICE detectors are used to make the initial minimum bias trigger decisions. These include the SPD layers of ITS, V0 and T0. SPD can count the number of hits in the first two layers of ITS. Minimum bias pp collisions typically require at least one hit in either SPD or V0A/V0C. Similarly Pb–Pb triggers look at both V0 and SPD hits. The p–Pb data has been mainly triggered using V0 information.

EMCal trigger

In addition to the minimum bias triggers, the most relevant trigger for this thesis is the EMCal trigger. Parts of the EMCal trigger has been developed at the University of Jyväskylä. Extensive details of the trigger and the development work can be found in the thesis of Jiří Král [250]. Personally I have contributed to the maintenance of the level 0 trigger.

ALICE EMCal provides two levels of trigger signal, L0 and L1, which allows triggering on either single shower deposits or integrated energy deposits in larger areas, i.e. jets [251]. As inputs the trigger gets exclusive sets of 2×2 EMCal towers, to limit the number of channels that need to be processed. The L0 trigger then checks for energy deposits within a rolling window of 2×2 trigger channels (4×4 towers). Areas of 4×4 towers most probably will contain only a single shower or two adjacent showers coming from a single decayed π^0 . Thus the trigger is called the single shower trigger.

For L0 the trigger decision is done in Trigger Region Units (TRU) that each cover 4×42 channels (8×48 towers). The amplitude from the sliding window is compared to a constant threshold. Additionally a peak finding algorithm is implemented to define correctly the time of the signal maximum. A single bit OR

decision of all individual TRUs is forwarded to the CTP as the EMCAL L0 trigger decision.

The L0 information is additionally forwarded to the L1 trigger, which recomputes similar 2×2 channel decisions to produce the single shower trigger, but L1 can perform the calculation also on the borders between trigger units. In addition the L1 trigger can check for energy deposits inside a larger 16×16 channel (32×32 towers) window, which is considered to be the jet trigger.

The L1 trigger can compare up to two thresholds for each single shower and jet trigger. There is a dedicated link in between the V0 detector and EMCAL STU, which can provide centrality information that is used to compute a dynamical threshold as a function of the V0 multiplicity.

The trigger subsystem provides both the L0 and L1 decisions to the CTP and DAQ.

2.4 TPC upgrade

2.4.1 ALICE upgrade during LS2

During LS2 in 2019-2020 ALICE will go through significant modifications. The goal is to be able have continuous readout [252] in heavy ion collisions at an interaction rate of 50 kHz. ALICE will add a new Forward Interaction trigger (FIT) [253] to provide trigger and timing replacing the V0 and T0 detectors. Also the current FMD and AD detectors will be dismantled and their roles will be taken over by FIT.

Additionally the current inner tracking system (ITS) will be completely replaced. The current layered structure with three different technologies will be replaced by a detector that uses pixel technology in all layers and with significantly reduced pixel size. Additionally the first layer will be brought closer to the beam pipe. The new ITS will have better tracking efficiency and better impact parameter resolution [230].

The muon detection will be complimented by the Muon Forward Tracker (MFT) [254]. Based on the same technology as the new ITS, MFT will be placed before the hadron absorber that sits in front of the existing muon spectrometer. MFT should significantly increase the signal/background ratio in heavy quark measurements [254].

2.4.2 TPC upgrade

Many subdetectors will make small improvements to enhance the readout rate. The central trigger processor will be replaced and ALICE will introduce a new framework O^2 that combines both online data acquisition and offline analysis.

The detector restricting the readout the most at the moment is the TPC. The current wire chamber based system limits the readout rate to 3.5 kHz. To achieve the 50 kHz readout rate goal the wire chambers will be replaced by a Gas Electron Multiplier (GEM) based system. The GEMs are designed to minimise ion backflow to allow continuous, ungated and untriggered readout. I have made a personal contribution to the quality assurance of the new GEM readout of TPC.

TPC has a total of 36 inner and 36 outer readout chambers. Each of these will consist of 4 layers of GEM foils. The inner chambers will only have one foil for each layer. The outer chambers are separated into three sections, each with its own layer of foils. Each GEM foil is made up of a 50 μm thick resistive capton layer, coated on both sides by 5 μm thick layers of copper. Each foils is separated into a number (20-24 depending on the size of the foil) of distinct active areas. The active areas are pierced densely with holes. They have 50-100 holes in the area of a single mm^2 . The density of holes changes from layer to layer. The two middle layers of foils have a larger (double) pitch (smaller hole density) while the top and bottom layers have a smaller (normal) pitch (larger hole density).

The purpose of the multilayered structure is to reduce the ion backflow [255, 256]; not only one layer of GEM foils will be installed, but a 4 layer stack. In the stack there are 2 standard pitch GEM foils, where the pitch size, i.e. the separation of the holes inside a foil is around 140 μm , and 2 large pitch GEM foils, where the hole spacing is two times larger, 280 μm . The two outer layers will have standard pitch and the two middle layers have large pitch. The middle layers with large pitch serve as extra insulator against the ion backflow. Additionally the setup allows operating individual GEM foils at lower voltages and still have an increase in the gain of a few orders of magnitude [257].

The holes have a conical shape which they acquire during a two step chemical etching process. The designed inner and outer diameters of the holes are $50 \pm 5\mu\text{m}$ and $70 \pm 5\mu\text{m}$ respectively. Figure 36 shows the cross-section of a hole alongside with the operation principle of a GEM foil.

The working principle of these foils is based on the Townsend avalanche phenomenon [258], which is also used in proportional counters such as Geiger counters. There is a large potential difference (140-400 V) applied to the two sides of the foil, which results in large field in each hole. Electrons gain energy in the field and if the electric field is strong enough, the free electron can gain sufficient velocity (energy) to liberate another electron when it next collides with a molecule. The two free electrons then travel along the electric field and can gain sufficient energy from the electric field to cause further impact ionisations, and so on, leading to a chain reaction. Under the right conditions a single electron entering any hole will create an avalanche containing 100–1000 electrons; this is the gain of the GEM foil.

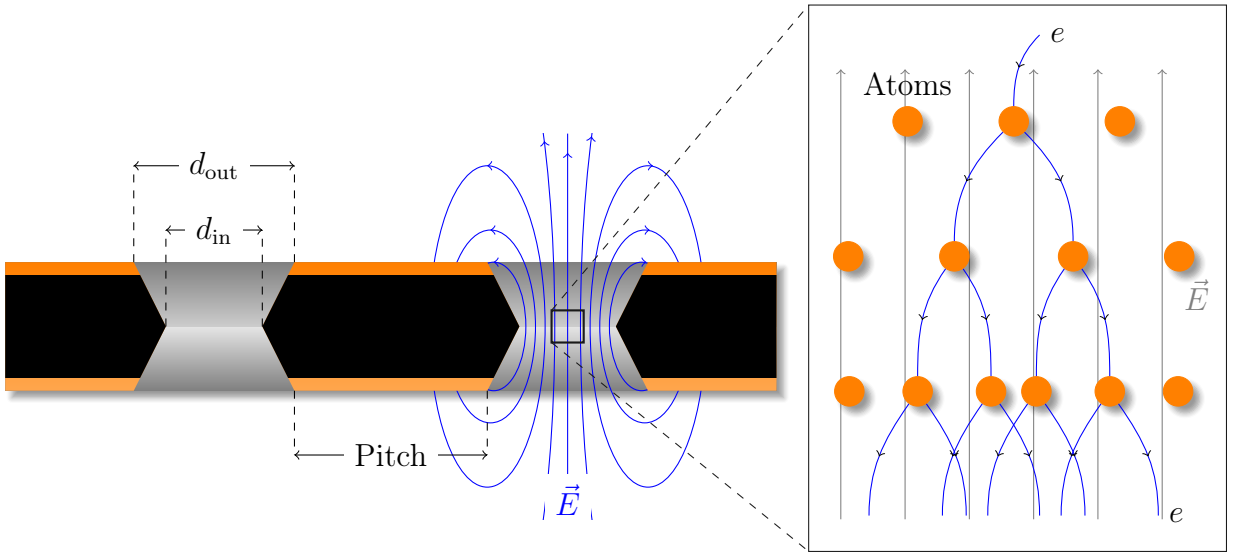


Figure 36: *left* Cross-section of a GEM foil. (Not to scale). The hole diameters are $d_{in} = 50 \pm 5 \mu\text{m}$ and $d_{out} = 70 \pm 5 \mu\text{m}$ and pitch is either 140 or 280 μm . *right* The amplification of a GEM foil is based on the Townsend avalanche phenomenon [258]. Electrons entering the electric field inside the hole are accelerated. If they gain enough energy before colliding with atoms they can liberate additional electrons, which are further accelerated leading to a chain reaction.

As opposed to wire chambers, which typically have one voltage setting, a GEM-based detector requires several independent voltage settings: there is a drift voltage which drives the electrons from the ionisation point to the GEM, an amplification voltage, and an extraction voltage that brings electrons from the GEM exit to the readout plane. In a multilayer system this is further complicated. The voltages between layers of foils can be tuned individually optimising amplification and preventing ion backflow.

Quality Assurance of the GEM foils

The GEM foils are produced at CERN, where they will undergo a basic QA (QA-B) procedure, that includes a coarse optical inspection for any large defects ($\gtrsim 1 \text{ mm}$) and a short term high voltage measurement. Afterwards the foils are sent for an advanced quality assurance (QA-A) procedure which is performed in one of the two QA-A centers, one in the Helsinki Institute of Physics (HIP) and one in the Wigner Research Centre in Budapest. Details of the QA-A procedure can be found in the thesis of Márton Vargyas [259] and in [260]. In the QA-A centers all foils are put through a detailed optical scanning process and a long term high voltage measurement. I was personally performing the QA production in Helsinki for the

final 6 months of the project.

The optical scan is performed with the help of a scanning robot. The setup along with most of the software was developed at the Detector Laboratory of the Helsinki Institute of Physics [261]. The optical scan is able to distinguish every single hole on the GEM foil and measure their properties. The purpose of the scan is two-fold; to catch defects that could affect the performance and classify the foils based on their hole parameters. It is expected that these are connected with the foil's electric properties [261]. For example, smaller holes create more intense and focused fields, which would result in larger amplification of their avalanche electrons, i.e. the local gain is expected to be larger.

After the optical scanning, the foils are subjected to a long term (5-12 hours) high voltage leakage current measurement. Each segment of the GEM foil is connected to a high voltage of 500 V and the leakage current is measured separately for each segment. The accepted leakage current in each segment is 0.16 nA. Foils that fail the criteria are sent to CERN for recleaning or repairing, after which they will go through the QA pipeline again.

Additionally some foils will be put through a gain mapping procedure. This process is time consuming and can only be performed in the QA-A center in Budapest. Thus it was done for only a small subset of foils. However, by measuring the gain in some foils the gain can be correlated with foil properties. Thus the single foil gain can be predicted based on the results of the optical scan. Details can be found in [259].

3 Event and track selection

The $\sqrt{s_{\text{NN}}} = 5.02$ TeV p–Pb ($1.3 \cdot 10^8$ events, $\mathcal{L}_{\text{int}} = 62 \text{ nb}^{-1}$) collisions were recorded in 2013 by the ALICE detector [217]. The details of the performance of the ALICE detector during LHC Run 1 (2009–2013) are presented in Ref. [262].

3.1 Event selection

This analysis uses both a minimum bias trigger and an EMCal based trigger to select the analysed events. For the 2013 p–Pb collisions minimum bias events are required to have signals in both V0A and V0C. The timing difference between the two stations is also used to reduce the contamination of the data sample from beam-gas events [262].

EMCal is used to provide the jet trigger used in triggered datasets. EMCal can be used to trigger on single shower deposits or energy deposits integrated over a larger area. Latter case is used for jet triggers. The EMCal trigger definition in the 2013 p–Pb collisions requires an energy deposit of either 10 GeV for the low threshold trigger or 20 GeV for the high threshold trigger in a 32×32 patch size. Triggers, V0 and EMCal are discussed in more detail in sections 2.3.5, 2.3.7 and 2.3.4.

3.2 Track reconstruction

The analysis uses charged tracks that are reconstructed with the Inner Tracking System (ITS) [263] and the Time Projection Chamber (TPC) [231]. These are discussed in sections 2.3.1 and 2.3.2. A detailed overview of track reconstruction in ALICE can be found from [262].

The track reconstruction procedure is shown in Figure 37. The figure shows only one track, but in reality the reconstruction has to deal with many tracks. The main reconstruction of tracks starts in TPC. There are 159 tangential pad rows in the TPC readout chambers. The track reconstruction starts from the outermost layer and the hits are paired with hits in the next layer inwards, taking into account a proximity cut. When this track finding procedure hits the innermost pad row in TPC, this information is used as an initial seed for the track finding in ITS. Similar procedure of pairing adjacent layers with a proximity cut is repeated in ITS.

After the reconstruction of tracks in ITS is completed, all the tracks are extrapolated to their point of closest approach to the preliminary interaction vertex. Then the second track fitting step begins, this time starting from the interaction point and proceeding outwards. A Kalman filter [264] technique is used to do the new fit using the hits found in the previous stage. This time the tracks are matched

also to the other detectors in the central barrel beyond TPC. When this step is complete, a final refit from the outermost TPC pad rows towards the interaction point is performed. The final track parameters come from this refit.

With the final track parameters the primary vertex can be determined with better accuracy than with only SPD information. The tracks are extrapolated to the nominal beam line and a weighted average of the points of closest approach determines the accurate primary vertex position.

The final step of the track reconstruction is the determination of the secondary vertices. For this, all the tracks whose distance of closest approach (DCA) to the primary vertex is larger than a defined minimum value are selected. For these tracks, points of closest approaches are determined for pairs of tracks. If the tracks are sufficiently close to each other and show characteristics of short lived particle decays, these points are identified as secondary vertices.

Combining the information from the ITS and the TPC provides a resolution ranging from 1 to 10 % for charged particles with momenta from 0.15 to 100 GeV/c. For tracks without the ITS information, the momentum resolution is comparable to that of ITS+TPC tracks below transverse momentum $p_T = 10$ GeV/c, but for higher momenta the resolution reaches 20 % at $p_T = 50$ GeV/c [262, 266].

Track selection

In p–Pb collisions the tracks are selected following the hybrid approach [267] which ensures a uniform distribution of tracks as a function of azimuthal angle (φ). The parameters in the approach are summarised in Table 2.

The first requirements are on the quality of the track fit in ITS and TPC. The ITS requirement only removes tracks that are clear outliers. For TPC the requirement is much more strict. For step 1 it is required that a track has 3 out of the 6 possible hits in ITS, one of which must be in the SPD. In step 2 this is replaced by an additional vertex constraint, where the primary vertex itself is added as a point to the track to improve the momentum resolution.

For the TPC, 70 crossed pad rows out of the maximum 159 is required. This measures the effective track length inside the TPC. This takes into account the possibility of having pad rows missing in the middle of the track due to charge in these clusters being below the threshold for some reason. Additionally it is required that the ratio between crossed rows and findable clusters is at least 0.8. Findable clusters are defined as the number of geometrically possible clusters which can be assigned to a track, taking into account dead zones due to chamber boundaries and limited η -acceptance. For both steps of the hybrid cut it is required that the fraction of clusters shared with several tracks is less than 40%.

The remaining cuts are meant to make sure that the measured tracks are really produced in the primary collision. A track might gain a kink due to a particle

Table 2: Parameters in the hybrid track cut

Track Cut	Step 1	Step 2
$\chi^2 / \text{ITS cluster}$	< 36	< 36
$\chi^2 / \text{ITS cluster}$	< 4	< 4
Hits in ITS	3	0
ITS hit requirements	1 in SPD	No requirement
Vertex constraint	No	Yes
Number of crossed rows in TPC	70	70
TPC crossed rows over findable clusters	> 0.8	> 0.8
Fraction of shared TPC clusters	< 0.4	< 0.4
Kink daughters	Rejected	Rejected
DCA_{xy}	< 3.2 cm	< 3.2 cm
DCA_z	< 2.4 cm	< 2.4 cm
Other		Rejected by step 1

scattering decay. The particle after such a kink, a kink daughter, is rejected in the cuts, as it no longer describes the properties of the primary collisions. The final cuts are on the distance of closest approach (DCA) of the track to primary vertex. To have confidence that the track comes from the primary collision, the track must be close enough to the primary vertex. The cuts are different for the distance along (DCA_z) and perpendicular to (DCA_{xy}) the beam axis.

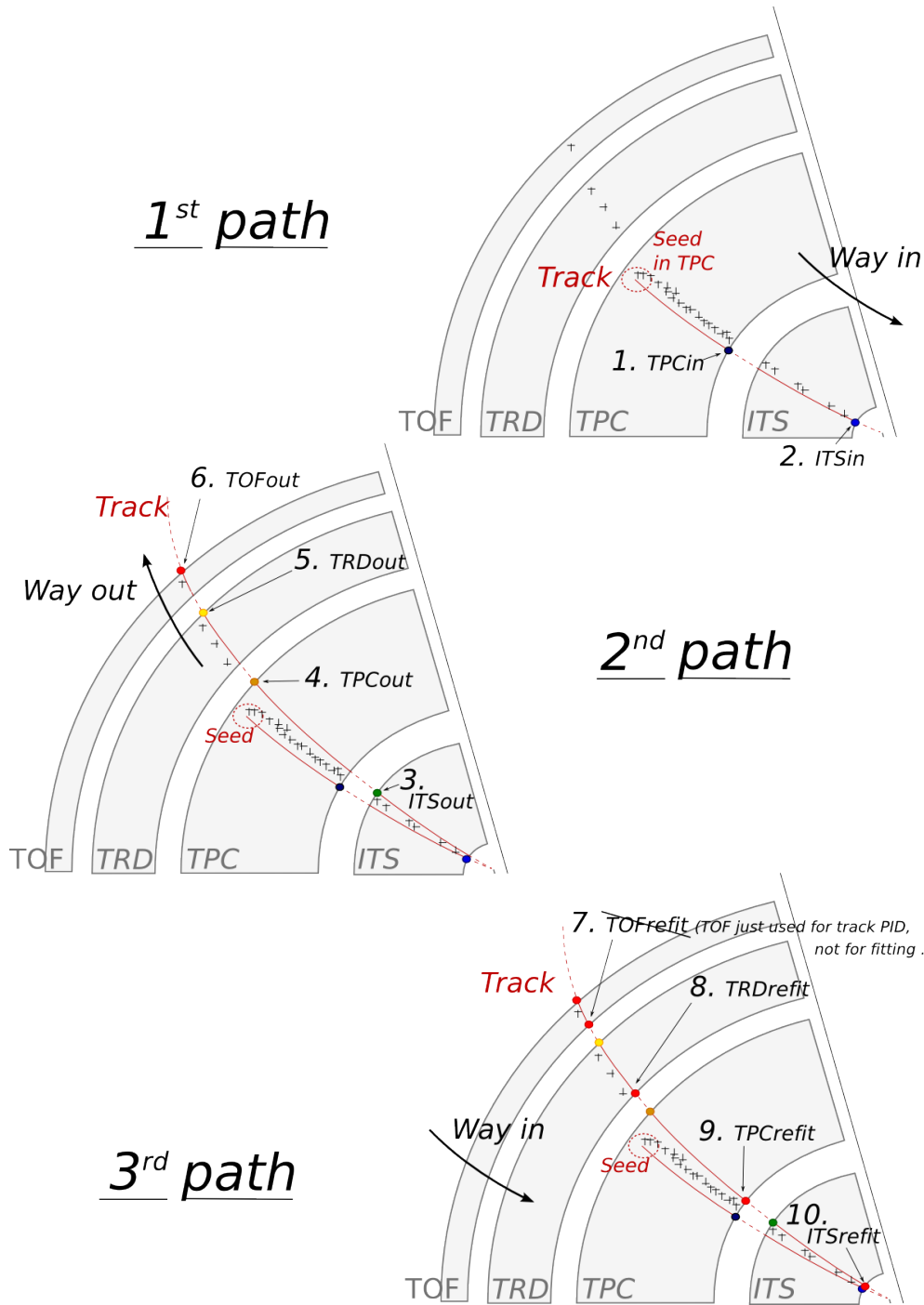


Figure 37: Principles of tracking in the ALICE experiment, showing the three successive paths allowing to build a track and refine its parameters. Numbers ranging from 1 to 10 mention the bits that are activated in case of success during the propagation of the Kalman filter at the considered stage. Figure from [265]

3.3 Cluster selection

Neutral particles used in jet reconstruction are reconstructed by the Electromagnetic Calorimeter (EMCal) [240]. The EMCal covers an area with a range of $|\eta| < 0.7$ in pseudorapidity and 100 deg in azimuth. EMCal is complimented with the Dijet Calorimeter (DCal) [241] and Photon Spectrometer (PHOS) [239] that are situated opposite of the EMCal in azimuth. PHOS covers 70 degrees in azimuth and $|\eta| < 0.12$. The DCal is technologically identical to EMCal. The DCal coverage spans over 67 degrees in azimuth, but in pseudorapidity the mid region is occupied by the PHOS. In between PHOS and DCal active volumes, there is a gap of 10 cm. DCal is fully back-to-back with EMCal.

The clusters used in the analysis were obtained from the EMCal clusteriser. The parameters used in the clusteriser are summarised in Table 3. The clusteriser searches for a tower with energy deposit greater than a defined seed energy and merges all surrounding (sharing a side) towers with energy deposit higher than a defined threshold. In the next step all towers sharing a side with already included towers are added, again requiring that the energy deposits exceeds the threshold. The algorithm can identify local minima and halts the clustering in case that the neighbouring tower energy is higher. Already clustered towers are removed from the pool, so one tower can only be clustered once.

Highly energetic calorimeter hits should spread into several towers as the electromagnetic shower evolves. However, some clusters with high energy have their energy located in a single tower. These are believed to come from a slow neutron hitting the APD readout of the towers. They are referred to as exotic clusters. The measure of exotoxicity is denoted as

$$1 - \frac{E_{\text{cross}}}{E_{\text{max}}}, \quad (42)$$

where E_{max} is the energy in the most energetic tower and E_{cross} is the sum of the four towers neighbouring the most energetic one. The closer this is to 1, the more

Table 3: Parameters used in the EMCal clusteriser

Setting	Value
Clusteriser seed	0.2 MeV
Clusteriser cutoff	0.05 MeV
Cells in cluster	> 1
Track matching radius	0.025
Fiducial cut	1 tower
Exotic cut	0.97
Minimal cluster Energy	0.3 GeV

exotic the cluster is and the larger the probability that it is fake. Cut of 0.97 has been adopted as default for analyses using EMCal, including the one presented in this thesis. Any clusters above this cut are removed.

A method of matching the cluster position to TPC track extrapolation is used to suppress charged hadron contribution to hits in EMCal. Tracks identified by the tracking detectors are extrapolated close to the EMCal surface, where the closest cluster is found and the track extrapolation is continued until reaching the same depth as the cluster. The remaining distance in between the extrapolated track and the cluster is then used to reject hadronic hits. Clusters matched to charged tracks are removed from the analysis as well as clusters being identified as fake.

4 Analysis method

4.1 Jet Finding

The analysis uses reconstructed jets as estimates of the original parton. Jet reconstruction essentially combines nearby tracks into jets.

Collisions between hadrons are never as clean as electron-electron collisions. Even for a proton-proton collision there are participant partons, that will produce a soft background in addition to the hard scattering products. Jet reconstruction must deal with this soft background. The reconstruction is never perfect, one can have uncorrelated tracks that get included in the jet and some tracks originating from the parton are missed by the reconstruction. There are several methods to perform the reconstruction, all of which require some kind of size parameter, which cuts out jet participants too far from the jet axis. The tracks that are grouped into a jet are referred to as jet constituents.

In each collision event, the jets are reconstructed using FastJet [268] with the anti- k_T algorithm [269]. Jets for $R=0.4$ are selected in $|\eta| < 0.25$ to satisfy the fiducial acceptance of the EMCAL. In jet reconstruction both charged tracks with $p_T > 0.15 \text{ GeV}/c$ and neutral clusters with $p_T > 0.30 \text{ GeV}/c$ are considered. Clusters that match charged tracks are removed before jet reconstruction. The analysis is then performed by analysing the charged jet constituents and results are presented in terms of the jet transverse momentum $p_{T,\text{jet}}$.

4.1.1 Anti k_T algorithm

Jets are reconstructed using the anti- k_T algorithm [269]. The algorithm works by trying to undo the splittings through combining protojets. First the algorithm creates a list of protojets. At the beginning the list is populated by converting each track in the event into a protojet. Then the algorithm proceeds by combining these protojets. A simplified picture of the process for a limited number of tracks is shown in Figure 38

The algorithm calculates distance measures for each individual protojet and for each possible pair of protojets. For individual protojets this depends on the transverse momentum of the track.

$$k_{T,i}^2 = p_{T,i}^{2p} \quad (43)$$

For each pair of protojets the distance measure is calculated as

$$k_{Ti,j}^2 = \min(p_{Ti}^{2p}, p_{Tj}^{2p}) \frac{\Delta R_{i,j}^2}{D^2}, \quad (44)$$

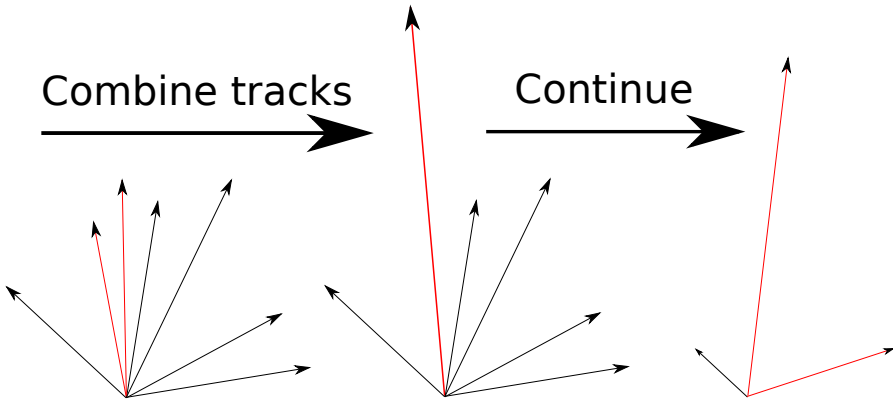


Figure 38: A simple example of the antil- k_{T} algorithm in progress. The red tracks in the leftmost figure are identified to have the smallest $k_{T,i}$ in the event and are combined into the red track of the middle figure. As this continues the remaining tracks are added to this or other jets. One track was deemed to be isolated enough to be counted as a protojet by itself. Note that the rightmost figure is zoomed out.

where

$$R_{i,j} = (\phi_i - \phi_j)^2 + (y_i - y_j)^2. \quad (45)$$

If k_{Ti} is the smallest quantity then the protojet is a jet and it is removed from further consideration. If $k_{Ti,j}$ is the smallest quantity the two protojets i and j are merged. This is repeated until no protojets are left.

The choice of the power p in the distance measure depends on the algorithm used

- $p = 1$: k_{T} algorithm
- $p = 0$: Cambridge Aachen algorithm
- $p = -1$: anti- k_{T} algorithm

With the choice $p = -1$ in anti- k_{T} algorithm, the softest splittings are undone first. One consequence of the power choice in the anti- k_{T} algorithm is that reconstructed jets have a shape close to circular.

4.2 Definition of j_{T}

The reconstructed jet axis is used for j_{T} reference. Any charged track within a fixed cone with radius R is taken as a jet constituent, as opposed to using the constituent list provided by the jet algorithm. Anti- k_{T} produces jets that are

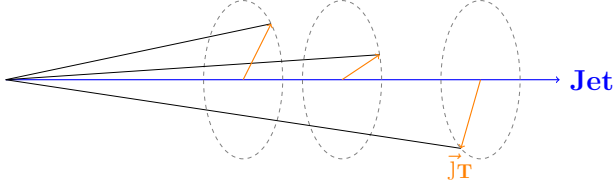


Figure 39: Illustration of \vec{j}_T . The jet fragmentation transverse momentum, \vec{j}_T , is defined as the transverse momentum component of the track momentum, \vec{p}_{track} , with respect to the jet momentum, \vec{p}_{jet} .

very circular in shape. Thus this doesn't change the constituent list considerably. Calorimeter clusters are used only in jet reconstruction.

The jet fragmentation transverse momentum, \vec{j}_T , is defined as the component of the constituent track momentum, \vec{p}_{track} , transverse to the jet momentum, \vec{p}_{jet} . It represents the transverse kick with respect to the initial hard parton momentum that is given to a fragmenting particle during the fragmentation process, which is a measure of the momentum spread of the jet fragments.

The resulting \vec{j}_T is illustrated in Fig. 39. The length of the \vec{j}_T vector is

$$j_T = \frac{|\vec{p}_{\text{jet}} \times \vec{p}_{\text{track}}|}{|\vec{p}_{\text{jet}}|}. \quad (46)$$

Resulting j_T distributions are shown as

$$\frac{1}{j_T} \frac{dN}{dj_T} \quad (47)$$

distributions. The logic behind this is that j_T is inherently a two-dimensional observable, comprised of j_{Tx} and j_{Ty} components. So the actual physical observable would be

$$\frac{d^2N}{d j_{Tx} d j_{Ty}} \quad (48)$$

Changing into polar coordinates with $j_{Tr} = j_T$ and θ gives

$$\frac{d^2N}{j_T d j_T d \theta}, \quad (49)$$

where j_T over the azimuth θ should stay constant and it can be integrated over, which gives

$$\frac{1}{2\pi} \frac{dN}{j_T d j_T}. \quad (50)$$

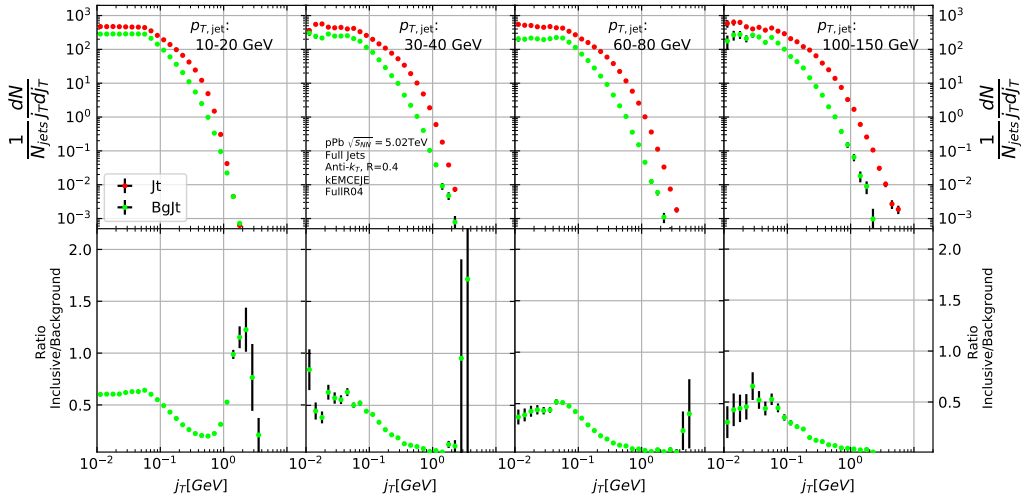


Figure 40: Inclusive j_T with background

Results of the raw inclusive j_T distribution in four $p_{T,jet}$ bins with background are shown in Figure 40. Background, i.e. the contribution from the underlying event, is further discussed in Section 4.4

4.3 Unfolding detector effects

The raw inclusive j_T distributions are corrected for the detector inefficiency with an unfolding procedure. The procedure uses response matrices obtained from a PYTHIA [270] simulation.

Measured distributions are affected by two main factors; Limited acceptance - The probability to observe a given event is less than one and limited resolution - Quantity x cannot be determined exactly, but there is a measurement error. True $f(x)$ and measured $g(y)$ distributions are connected by a convolution integral. Including statistical fluctuations this becomes

$$\hat{g}(y) = \int_a^b A(y, x) f(x) dx + \epsilon(y), \quad (51)$$

where A is the detector response obtained by (for example) Monte Carlo simulations and $\epsilon(y)$ is the term coming from statistical fluctuations. If x and y are discrete variables we have

$$\hat{g}_i = \sum_{j=1}^m A_{ij} f_j + \epsilon_i, \quad (52)$$

where i and j give the j_T bins in the true and measured distributions. f_j and g_i give the counts in these bins. Or in matrix form

$$\hat{g} = Af + \epsilon, \quad (53)$$

where \hat{g} and f are vectors corresponding to the measured and true histograms. If the only detector effect is limited acceptance, A is a diagonal matrix, i.e. $A_{ij} = 0$ for $i \neq j$. We want to deduce the true distribution f , when the measured distribution g is known. In a general discrete case the (naive) solution is obtained by the inverse matrix

$$\hat{f} = A^{-1}\hat{g} \quad (54)$$

However this usually leads to oscillating solutions and determining the inverse matrix can be difficult.

Two common methods to perform this inversion are Bayesian and SVD unfolding methods. Often the solution requires some additional *a priori* information. For example the solution should be smooth in most cases.

4.3.1 Bayesian unfolding

The bayesian (iterative) method is based on the Bayes formula [271].

$$P(C_i|E_j) = \frac{P(E_j|C_i) P_0(C_i)}{\sum_{l=1}^{n_C} P(E_j|C_l) P_0(C_l)}, \quad (55)$$

i.e. the probability of Cause C_i ("truth") given Effect E_j ("observed") is proportional to the probability of observing E_j given C_i , $P(E_j|C_i)$ (response matrix) and the true distribution $P_0(C_i)$.

In the unfolding procedure P_0 is given some starting distribution, either a uniform distribution or some guess of the final distribution. Taking into account the inefficiency this gives

$$\hat{n}(C_i) = \frac{1}{\epsilon_i} \sum_{j=1}^{n_E} n(E_j) P(C_i|E_j), \quad (56)$$

where

$$P(C_i|E_j) = \frac{P(E_j|C_i) P_0(C_i)}{\sum_{l=1}^{n_C} P(E_j|C_l) P_0(C_l)}, \quad (57)$$

and $n(E_j)$ are the observed frequencies. First $P(C_i|E_j)$ is calculated with the uniform distribution or best guess of the shape of the distribution. This is then used to calculate the new distribution $\hat{P}(C_i)$

$$\hat{N}_{true} = \sum_{i=1}^{n_C} \hat{n}(C_i), \quad \hat{P}(C_i) = P(C_i|\hat{n}(E)) = \frac{\hat{n}(C_i)}{\hat{N}_{true}} \quad (58)$$

P_0 is then replaced with \hat{P} and the procedure is repeated until an acceptable solution is found. One way to gauge the acceptability is measuring the change between iterations. Initially there is a large change between iterations, but it should get small when close to the final distribution. The number of iterations should be as low as possible, as the errors increase when going further in the iterations, but the number of iterations must be high enough so that the correct distribution is extracted.

The bayesian procedure alongside with the SVD unfolding method are implemented in the RooUnfold package [272], which is used to perform the unfolding in practice. SVD unfolding is another procedure that utilises the Singular Value Decomposition (SVD) of the response matrix to find the inverse of the response matrix [273].

Error propagation in the Bayesian procedure

The measured distribution has some statistical uncertainty, this should be reflected in the unfolded distribution. Additionally the response matrix may have some uncertainty if the statistics used in the Monte Carlo simulation were limited.

For errors originating from the measured distribution RooUnfold uses the error propagation matrix

$$\frac{\partial \hat{n}(C_i)}{\partial n(E_j)} = M_{ij} + \frac{\hat{n}(C_i)}{n_0(C_i)} \frac{\partial n_0(C_i)}{\partial n(E_j)} - \sum_{k=1}^{n_E} \sum_{l=1}^{n_C} \frac{n(E_k) \epsilon_l}{n_0(C_l)} M_{ik} M_{lk} \frac{\partial n_0(C_l)}{\partial n(E_j)}, \quad (59)$$

where $\hat{n}(C_i)$ is the unfolded result from Eq. 58. This depends upon the matrix $\frac{\partial n_0(C_i)}{\partial n(E_j)}$, which is $\frac{\partial \hat{n}(C_i)}{\partial n(E_j)}$ from the previous iteration. In the first iteration, $\frac{\partial n_0(C_i)}{\partial n(E_j)} = 0$ and $\frac{\partial \hat{n}(C_i)}{\partial n(E_j)} = M_{ij}$.

The error propagation matrix V is used to obtain the covariance matrix on the unfolded distribution

$$V(\hat{n}(C_k), \hat{n}(C_l)) = \sum_{i,j=1}^{n_E} \frac{\partial \hat{n}(C_k)}{\partial n(E_i)} V(\hat{n}(E_i), \hat{n}(E_j)) \frac{\partial \hat{n}(C_l)}{\partial n(E_j)}, \quad (60)$$

where $V(\hat{n}(E_i), \hat{n}(E_j))$ is the covariance matrix of the measurements. In counting experiments common in particle physics, each bin is independently Poisson distributed, with

$$V(\hat{n}(E_i), \hat{n}(E_j)) = n(E_i) \delta_{ij} \quad (61)$$

The error propagation matrix for the response matrix is

$$\begin{aligned} \frac{\partial \hat{n}(C_i)}{\partial P(E_j|C_k)} &= \frac{1}{\epsilon_i} \left(\frac{n_0(C_i) n(E_j)}{f_j} - \hat{n}(C_i) \right) \delta_{ik} - \frac{n_0(C_k) n(E_j)}{f_j} M_{ij} + \\ &\quad \frac{\hat{n}(C_i)}{n_0(C_i)} \frac{\partial n_0(C_i)}{\partial P(E_j|C_k)} - \frac{\epsilon_i}{n_0(C_i)} \sum_{l=1}^{n_E} \sum_{r=1}^{n_C} n(E_l) M_{il} M_{rl} \frac{\partial n_0(C_r)}{\partial P(E_j|C_k)}, \end{aligned} \quad (62)$$

where $\frac{\partial n_0(C_i)}{\partial P(E_j|C_k)}$ is the error propagation matrix from the previous iteration, $\frac{\hat{n}(C_i)}{\partial P(E_j|C_k)}$. For the first iteration, this is zero and the final two terms in Eq. 62 disappear.

The covariance matrix due to these errors is given by

$$V(\hat{n}(C_k), \hat{n}(C_l)) = \sum_{j,s=1}^{n_E} \sum_{i,r=1}^{n_C} \frac{\partial \hat{n}(C_k)}{\partial P(E_j|C_i)} V(P(E_j|C_i), P(E_s|C_r)) \frac{\partial \hat{n}(C_l)}{\partial P(E_s|C_r)}, \quad (63)$$

where $V(P(E_j|C_i), P(E_s|C_r))$ can be taken as multinomial, Poisson or other distribution.

4.3.2 Toy Monte Carlo

A toy Monte Carlo simulation was performed to see the performance of unfolding in an ideal case. The simulations samples jet p_T values from the observed p_T distribution. Starting from this p_T the simulations starts creating tracks with

$$p_{\text{track}} = z_{\text{track}} p_{T,\text{jet}} \quad (64)$$

where z_{track} is sampled from the observed z distribution. Tracks are given random η and ϕ values from uniform distributions centred at 0. All tracks below 0.15 GeV are discarded. Sampling is continued until the sum of the track transverse momenta exceeds the jet transverse momentum. The sum of all the track momenta is calculate. This is sum is then defined to be the jet.

Simultaneously a p_T dependant observation efficiency is applied to the tracks and a separate observed jet is calculated using only the observed tracks. Additionally a set of fake tracks is added to the observed jet. Fake tracks are generated identically to normal tracks, except for $p_{T,\text{track}}$, which is taken from an uniform distribution between 0.15 GeV and 1 GeV. Tracks are always either observed or not at the true momentum. No smearing is added to the observed momentum.

Afterwards the tracks are looped over for j_T calculation. For observed tracks we calculate j_T with respect to both the true jet axis and the observed jet. 2D Response matrix is filled with

$$(j_T^{\text{obs}}, p_{T,\text{jet}}^{\text{obs}}, j_T^{\text{true}}, p_{T,\text{jet}}^{\text{true}}) \quad (65)$$

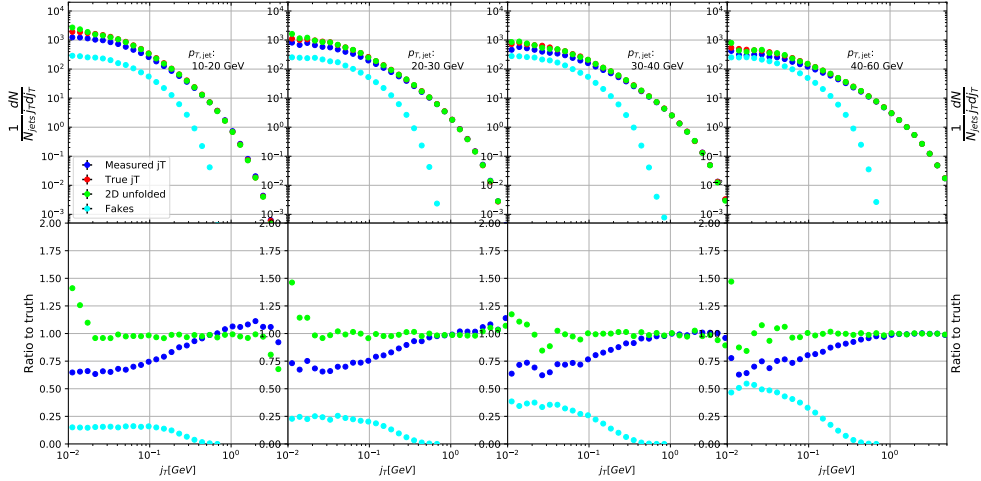


Figure 41: Results from unfolding in Toy Monte Carlo

In practice this is done with a set of 3D histograms, where $p_{T,\text{jet},\text{true}}$ determines the histogram index and the remaining three values the bin in the 3D histogram.

After creating the response matrices, an identical procedure is carried out to the create testing data. Now instead of filling response matrices, 2D histograms are filled with $(j_T^{\text{obs}}, p_{T,\text{jet}}^{\text{obs}})$ and $(j_T^{\text{true}}, p_{T,\text{jet}}^{\text{true}})$

The observed distributions are unfolded using the 2D Bayesian (iterative) algorithm of RooUnfold. Results are shown in Figure 41. Aside from some discrepancy at very low j_T the true distribution is retrieved well.

4.3.3 Pythia Response matrices

A PYTHIA 6 simulation was carried out to determine the response matrices. The simulation used the Perugia 2011 [274] tune with $\sqrt{s_{NN}}=5.02$ TeV. The detector response of the particle level tracks was simulated using GEANT3 [275, 276].

Response matrices are filled through correlation between MC detector and particle level jets and tracks. When creating the response matrices detector level tracks in each event are first analysed using the same procedure as for data, but their j_T values are stored in an array. This is only done for tracks that are closer than the cone size, R , to a jet. Thus most tracks in the event will not have their j_T values calculated. The analysis then moves to particle level (MC) tracks. There are analysed similarly, but for each track the code checks whether a corresponding detector level track existed and if that track had a j_T value. Finally the code checks for detector level tracks that don't have corresponding particle level track with a j_T value.

There are several possibilities that have to be taken into account:

- We find a corresponding track with a j_T value. Response matrix is filled normally with $(j_T^{\text{obs}}, p_{T,\text{jet}}^{\text{obs}}, j_T^{\text{true}}, p_{T,\text{jet}}^{\text{true}})$
- We don't find a corresponding track. Record $(j_T^{\text{true}}, p_{T,\text{jet}}^{\text{true}})$ as a miss
- We find a corresponding track, but it didn't have j_T value. Most likely because it was not part of a jet in the detector level set. Similary record $(j_T^{\text{true}}, p_{T,\text{jet}}^{\text{true}})$ as a miss
- For detector level tracks that have no correspondence in particle level set the code records $(j_T^{\text{obs}}, p_{T,\text{jet}}^{\text{obs}})$ as a fake

In the analysis code the response matrix is made of an array of 3 dimensional histograms, with $(j_T^{\text{obs}}, p_{T,\text{jet}}^{\text{obs}}, j_T^{\text{true}})$ as axes. The histogram index gives the $p_{T,\text{jet}}^{\text{true}}$ value. The ranges in the response matrices of both j_T and $p_{T,\text{jet}}$ match the ranges used for the end results. For j_T the range is between 0.01 GeV and 20 GeV and $p_{T,\text{jet}}$ between 5 GeV and 500 GeV. The ranges are the same in detector and particle level.

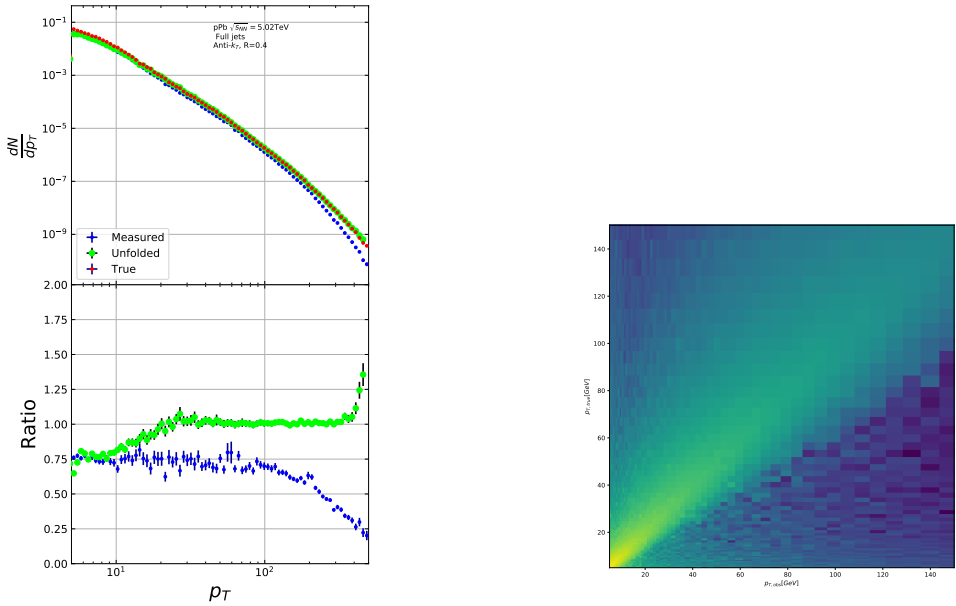
As a primary method unfolding is performed with an iterative (bayesian) algorithm using the RooUnfold [272] package. The number of iterations used is 4. As a default the true j_T distribution from the PYTHIA simulation is used as the prior.

4.3.4 Unfolding closure test

The PYTHIA set is divided into 2 halves. First is used to fill the response matrices, as well as record missed and fake tracks. Second half is used to test the effectiveness of the unfolding method. Jet p_T distributions are shown in Figure 42a and response matrix are shown in Figure 42b. For the range where this analysis is performed, $40 \text{ GeV} < p_{T,\text{jet}} < 150 \text{ GeV}$, the $p_{T,\text{jet}}$ distribution is recovered well. At low $p_{T,\text{jet}}$ the true distribution can't be recovered. The primary reason is that jet with $p_{T,\text{obs}} < 5 \text{ GeV}$ are not considered, although $p_{T,\text{true}}$ would have been above 5 GeV. Thus these are missing from the response matrix and their contribution can't be unfolded. At high $p_{T,\text{jet}}$ the situation is opposite. Jets with $p_{T,\text{true}} > 500 \text{ GeV}$ are lost due to histogram limits. Thus jets just below this limit are overrepresented in the response matrix for $p_{T,\text{obs}} \approx 500 \text{ GeV}$.

Response matrices within single jet p_T bins are shown in Figure 43. Results from the closure test are shown in Figure 44. In the lowest jet p_T bins unfolding fails to recover the true distribution. The lowest jet p_T bins are dominated by combinatorial jets and thus the true detector response is likely not retrieved.

Above $30 \text{ GeV} < p_{T,\text{jet}} < 40 \text{ GeV}$ the distribution is recovered well in the mid j_T region. At $j_T < 0.1 \text{ GeV}$ there is clear discrepancy and hence the final results are shown only for $j_T > 0.1 \text{ GeV}$. Additionally there is some discrepancy at very high j_T . This is taken into account in the unfolding systematics.



(a) Unfolded jet p_T distribution in PYTHIA closure test
(b) Jet p_T response matrix from unfolding closure test

Figure 42: Jet p_T in unfolding closure test

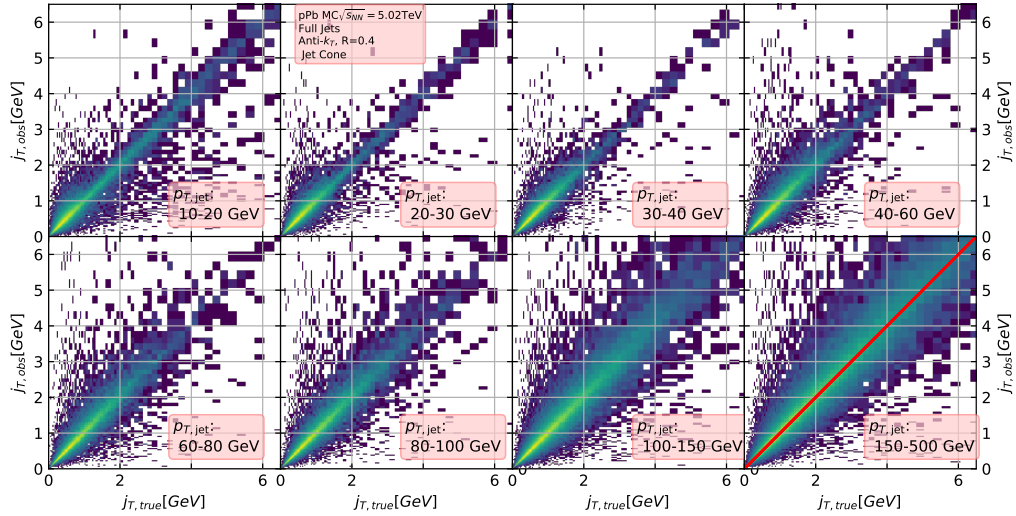


Figure 43: j_T Response matrices in individual $p_{T,jet}$ bins

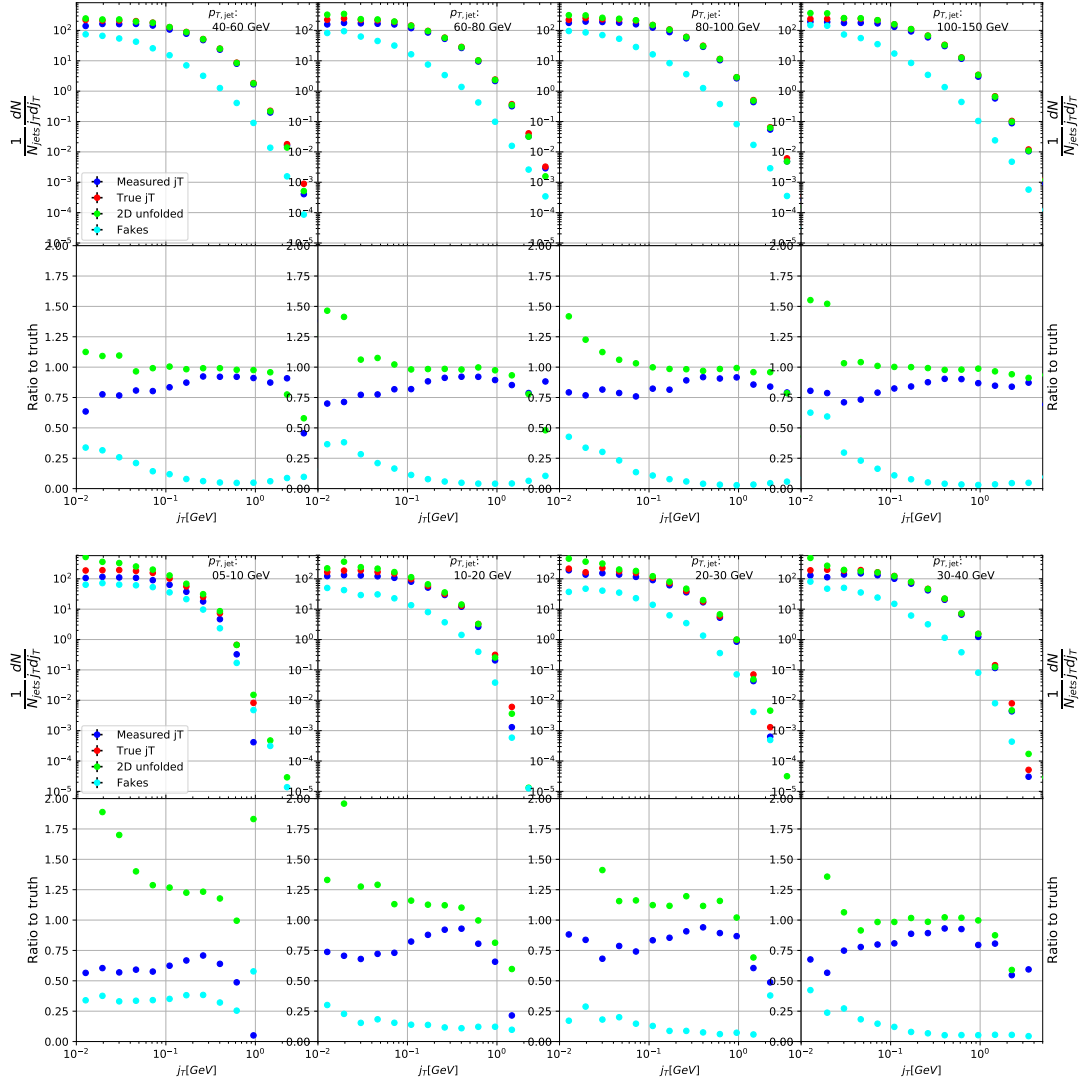


Figure 44: Pythia closure test results. Fake tracks include also tracks that do exist in the true dataset, but for one reason or another were not given j_T values. j_T is only calculated for tracks that are associated with jets

4.4 Background

When calculating j_T distributions for jet constituents there is a contribution from the underlying event (UE), i.e. tracks that just happen to be close to the jet axis. To find the signal coming from the actual jet we need to subtract the background (UE) contribution. On a jet-by-jet basis this is difficult to achieve reliably, so one must estimate the background contribution in the inclusive distribution. A schematic view of the background contribution is shown in Figure 45.

We have two methods for background estimation. In the first we look at the direction perpendicular to the jet. This is assumed to be the region least likely to contain jet contributions. In the second method we randomly assign the tracks of event new ϕ and η values. The result is thus guaranteed to be uncorrelated.

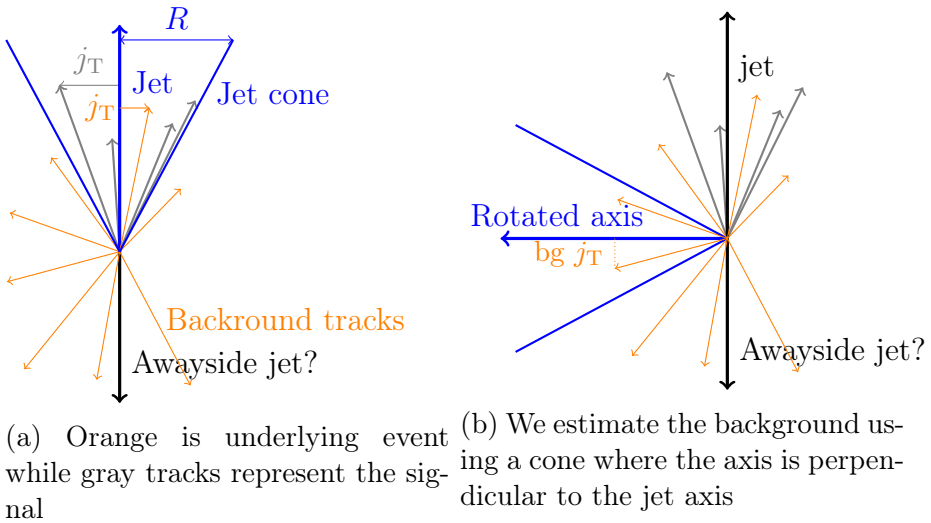


Figure 45: Background estimation

4.4.1 Perpendicular cone background

As a primary method to estimate the background we look at regions of the detector where there are no tracks from jets, but only uncorrelated tracks from the underlying event. The underlying event is thus estimated by looking at an imaginary jet cone perpendicular to the observed jet axis ($\frac{\pi}{2}$ Rotation in ϕ).

After calculating the j_T values for tracks in the jet, we rotate the jet axis by $\frac{\pi}{2}$ in positive ϕ direction. We check that there are no other jets closer than $2R$ to the rotated axis. Otherwise background calculation is skipped for this jet. Probability of this happening is 1-2% depending on the jet p_T bin.

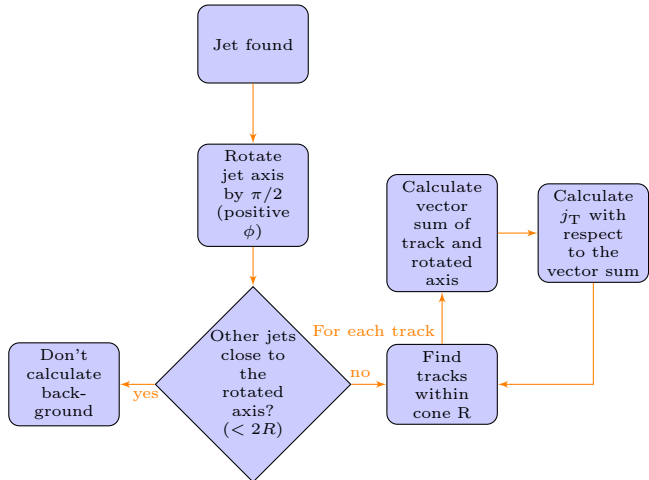


Figure 46: Flowchart representation of the perpendicular cone background procedure

If we don't find other jets in the vicinity we move on to estimate the background. We find all tracks within a cone of radius R around the rotated axis and calculate j_T of these tracks with respect to the rotated axis.

This background procedure is a part of the reason for using charged tracks inside a fixed size cone, instead of jet constituents. To be representative of the actual underlying event contribution the size and shape of the background estimation region should match the area where j_T is calculated. The irregular shape of a jet would be hard to take into account when calculating background. Thus the regions are made to match by considering fixed size cones for j_T .

One additional consideration is the issue of auto-correlations as the jet axis is simply a vector sum of all its constituents. Thus having an additional track in the jet from the underlying event moves the jet axis towards this track. Since the axis is now closer to the track, it has a smaller j_T value. Assuming a 1 GeV background track at the edge of a $R = 0.4$ cone the j_T value would be 0.4 GeV. If this is added to a 5 GeV jet, the j_T value becomes 0.33 GeV after the jet axis moves. In a 50 GeV jet it would be 0.39 GeV. This is a region where the inclusive j_T distribution is dominated by background. The distribution is also steeply falling. Overestimating the background can lead to a situation where the background estimation exceeds the inclusive distribution.

To take this effect into account we can't use a fixed axis for background, but it has to behave like a jet would when additional tracks are added. Thus before calculating j_T values we make a vector sum of the track and the axis used for background, which is either the perpendicular cone axis or the random axis depending on the background method. In each case the momentum of this background axis

is assumed to be the same as the jet which initiated the background estimation.

In pPb data there is on average about one underlying event track in a $R = 0.4$ cone. If there would be more, one should consider taking the vector sum of all tracks inside the cone. As there is usually only one track and if there are more it's unlikely that more than one has high momentum, taking the vector sum track-by-track should be enough.

4.4.2 Random background

In the random background method we look at all tracks in the event, except for tracks close to jets found by the jet algorithm. We randomly assign new η and ϕ values to all tracks using uniform distributions with $|\eta| < 1.0$. p_T values are kept the same. To increase statistics there is a possibility to create a number of random tracks for each actual track. In the analysis we do this 10 times for each track. Again the track p_T value is kept the same.

We create a random jet cone from uniform η and ϕ distributions. Here $|\eta| < 0.25$. Now we calculate j_T of the random tracks with respect to the random cone axis. As in the perpendicular cone method auto-correlations are added before calculating j_T .

Comparison between perpendicular cone and random background in Figure 47. The advantage of the random background method is that the procedure can be repeated several times for each event, which allows producing additional statistics. However, it seems that, especially in the highest $p_{T,jet}$ bins there is some jet contribution left at the high end. Naturally there is no correlation between the tracks and the background axis, but if some high momentum tracks originating from jets were not subtracted and happen to hit the edge of the background cone, they can increase the high j_T yield in the background estimation.

We observe that the results from perpendicular cone background show no observable change between $p_{T,jet}$ bins. It is a good indication that the background is actually dominated by the underlying event over the entire j_T region.

Thus as a primary method of background estimation the perpendicular cone method is used. The random background method is used to estimate systematic contributions by comparing the final results obtained with this method to the results obtained from the perpendicular cone method.

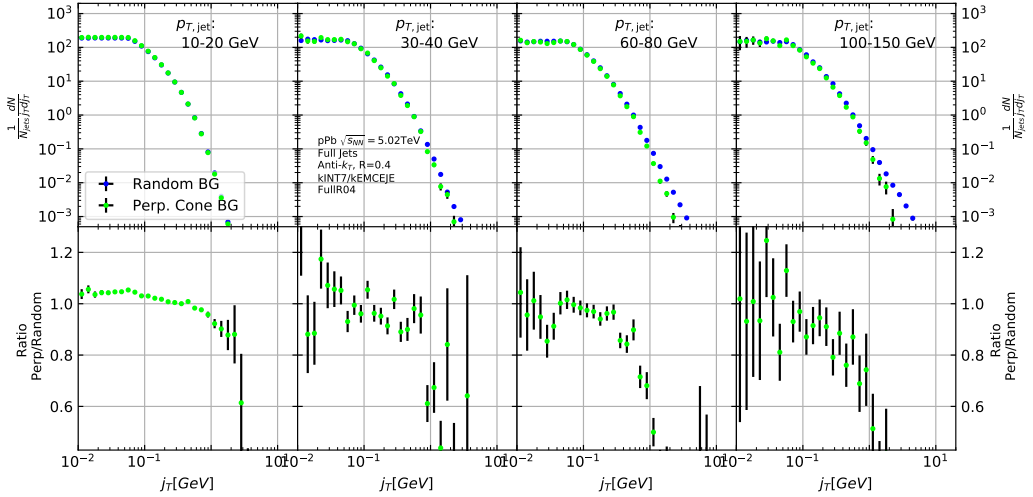


Figure 47: j_T background with two different methods

4.5 Fitting

After unfolding and background subtraction the resulting signal distributions are fitted with a 2 component function shown in Eq. 66. Gaussian distribution is used for low j_T and an inverse gamma function is used for high j_T . The Gaussian is taken to have the center at $j_T = 0$. In total this gives 5 parameters. The fitting procedure was inspired by the dihadron j_T analysis by ALICE [277]. The complete fitting function is

$$\frac{1}{N_{\text{jets}} j_T d j_T} \frac{dN}{d j_T} = \frac{B_2}{B_1 \sqrt{2\pi}} e^{-\frac{j_T^2}{2B_1^2}} + \frac{B_3 B_5^{B_4}}{\Gamma(B_4)} e^{-\frac{B_5}{j_T}}. \quad (66)$$

To achieve stable results the fitting is performed in two steps. First both components are fitted separately. Gaussian component is fitted to the low end of j_T . Inverse gamma component is fitted to j_T above 1 GeV/c. After getting the results from the individual fits they are combined into a single function with initial values from the individual results and an additional fit is performed.

After getting the fit function $\sqrt{\langle j_T^2 \rangle}$ (RMS) and yield values are extracted separately from each component. The narrow component RMS is

$$\sqrt{\langle j_T^2 \rangle} = \sqrt{2} B_1, \quad (67)$$

and the wide component RMS value is calculated as

$$\sqrt{\langle j_T^2 \rangle} = \frac{B_5}{\sqrt{(B_4 - 2)(B_4 - 3)}}, \quad (68)$$

where it is required that $B_4 > 3$.

The statistical errors can be calculated with the general error propagation formulas. As a result one gets errors for the narrow component RMS

$$\delta \sqrt{\langle j_T^2 \rangle} = \sqrt{2} \delta B_1 \quad (69)$$

and for the wide component RMS

$$\delta \sqrt{\langle j_T^2 \rangle} = \sqrt{\left(\frac{(5 - 2B_4) B_5 \delta B_4}{(2(B_4 - 2)(B_4 - 3))^{\frac{3}{2}}} \right)^2 + \left(\frac{\delta B_5}{\sqrt{(B_4 - 2)(B_4 - 3)}} \right)^2} \quad (70)$$

5 Systematic errors

The main systematic uncertainties in this analysis come from the background estimation, the unfolding procedure and uncertainty in the tracking efficiency. The systematics in background estimation were studied using an alternative method to extract the background, the random background method and the uncertainty in tracking was studied by varying tracking efficiencies in a PYTHIA simulation.

The systematic uncertainty that arises from the unfolding procedure is estimated by performing the unfolding with two separate methods. Data corrected by the iterative unfolding method are used as the results and the SVD unfolding method is employed to estimate the uncertainty. In a PYTHIA closure test the true distribution was in general found to be between the unfolded distributions from the iterative and SVD method. The difference between the methods when unfolding data should give a reasonable estimate of the unfolding uncertainty. The resulting uncertainty is below 8% for both wide and narrow component RMS.

5.1 Background

The uncertainty coming from background calculation is estimated by subtracting the background separately for the perpendicular cone and random background methods. Comparisons of the resulting signal distributions are shown in Figure 48.

Fits are then performed on both perpendicular cone and random background signals. Difference between them is taken as the systematic uncertainty. The fits for individual bins from the random background method are shown in Figure 49. Resulting differences between the methods for different components are shown in Figure 50. The dotted lines are put at $\pm 5\%$ for the narrow component and at $\pm 8\%$ for the wide component. These are taken as systematic estimates for the entire $p_{T,jet}$ range.

5.2 Unfolding

Unfolding is the second major source of systematic uncertainty. To estimate the uncertainty related to the unfolding procedure several checks are performed. The main systematic uncertainty estimation comes from comparing results performed using both SVD and Bayesian unfolding. Difference between the methods is taken as the systematic uncertainty. Since SVD unfolding does not have a two dimensional option, the unfolding is done bin by bin.

As in the background systematic estimation, fits are performed for both cases separately. Resulting differences between the methods for different components are shown in Figure 51. The dotted lines are at $\pm 8\%$ for both components. These are taken to be the systematic uncertainty related to unfolding.

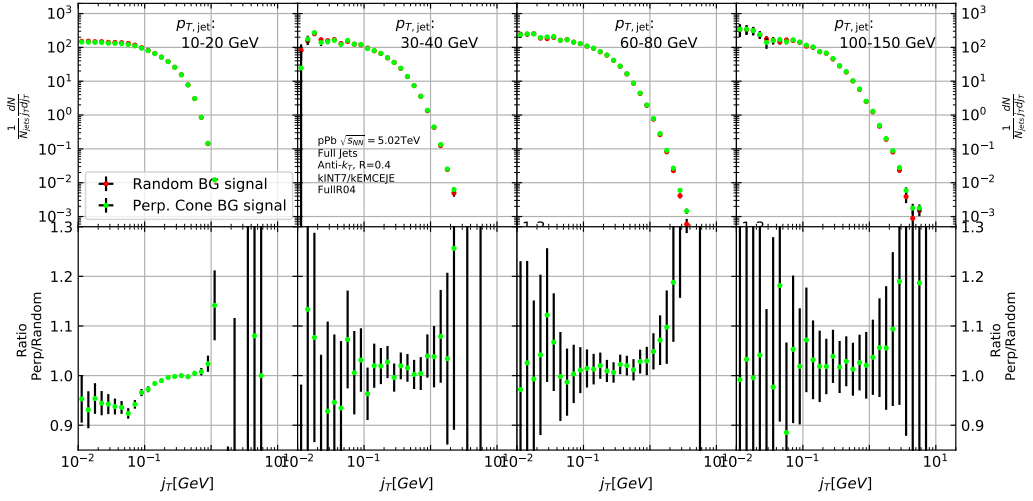


Figure 48: Comparison of the effect of background method on j_T signal.

Several other systematic checks were performed with the Bayesian unfolding procedure. They are described in the following sections. As these are small compared to the main uncertainty they are not included separately.

5.2.1 Effect of number of iterations

The iterative unfolding algorithm permits the change of number of iterations. The unfolding procedure was carried out using different numbers of iterations. The results from these different cases are shown in Figure 52. The results are compared to the default unfolding algorithm with 4 iterations. The difference in results between the different cases is mostly less than 2.5%.

5.2.2 Effect of different prior

The iterative algorithm requires a prior estimate of the shape of the distribution. As a default prior the truth (particle level) distribution is used. To test the effect of changing the prior we instead use the unfolded j_T distribution as prior. The results are compared to the unfolding algorithm with the default prior. This is shown in Figure 53. The difference in results between the different cases is mostly less than 2.5%.

5.2.3 Effect of p_T truncation

As an additional check the unfolding is carried out with different $p_{T,\text{jet}}$ truncation values. By default the full range of $p_{T,\text{jet}} > 5\text{GeV}$ is used. We test the unfolding

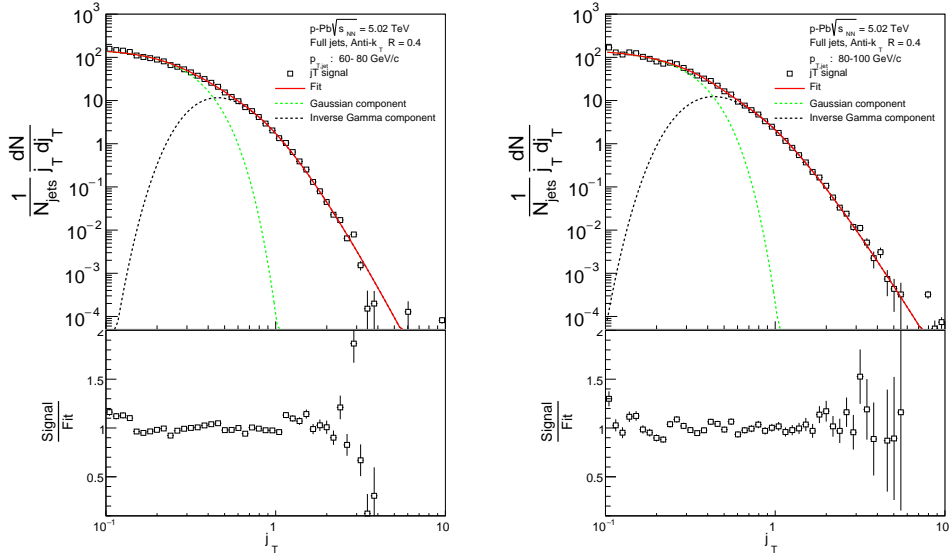


Figure 49: j_T signal with random background subtraction fits in different jet p_T bins

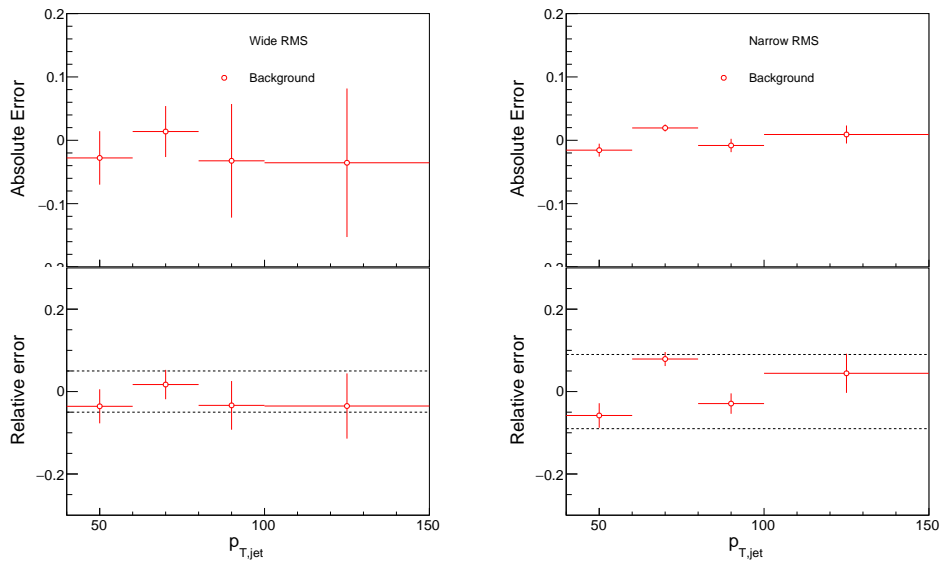


Figure 50: Differences between perpendicular cone and random background subtraction in the resulting RMS values.

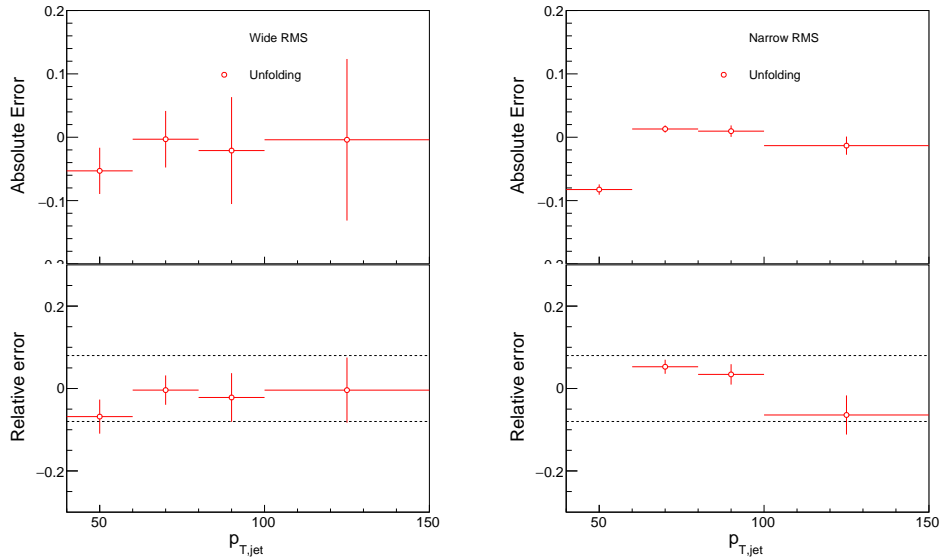


Figure 51: Differences between Bayesian and SVD unfolding in the resulting RMS values

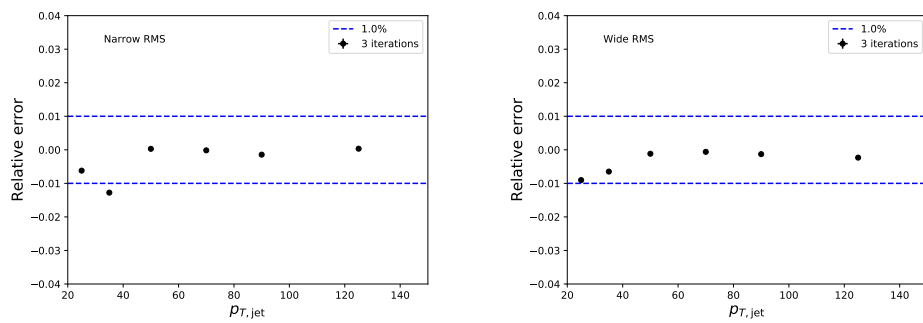


Figure 52: Unfolding with different number of iterations

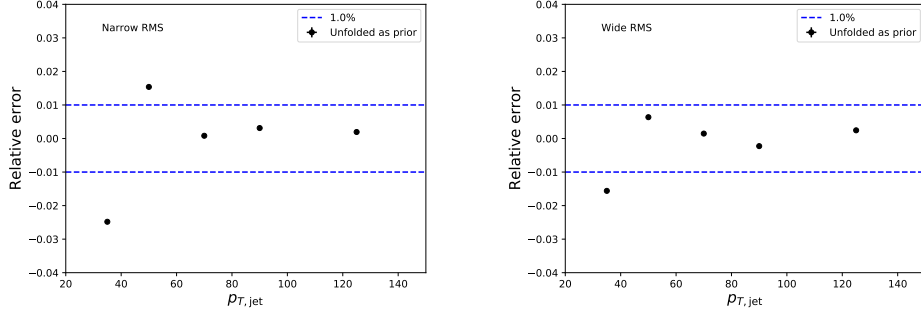


Figure 53: Effect of changing prior from true distribution in PYTHIA to the unfolded distribution.

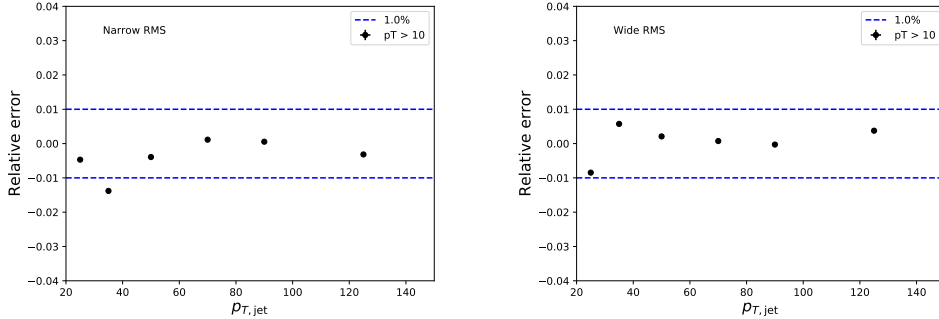


Figure 54: Effect of changing minimum jet p_T used in unfolding from 5 to 10 GeV

by only using the response matrix for $p_{T,\text{jet}} > 10 \text{ GeV}$. The results of this test are shown in Figure 54. The effects are strongest in the lower $p_{T,\text{jet}}$ bins. Also in this case the difference is less than 2.5 % in all $p_{T,\text{jet}}$ bins.

5.3 Tracking

Systematic effects originating from uncertainty in the tracking efficiency are estimated through a PYTHIA simulation, where an artificial inefficiency of 3% is introduced i.e. 3 % of tracks are randomly removed from each event. The effect of this artificial inefficiency is shown in Figure 55. The systematic uncertainties assigned to tracking efficiency are 4% for the narrow component and 5% for the wide component.

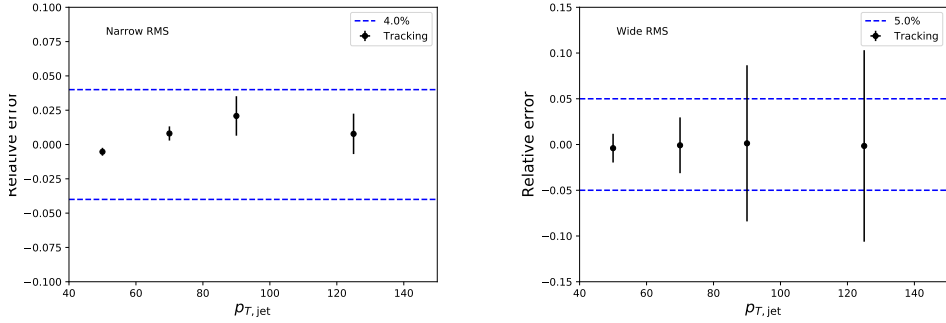


Figure 55: Relative systematic uncertainties resulting from tracking efficiency uncertainty.

5.4 EMCAL clusters

The analysis uses EMCAL clusters only in the reconstruction of jets. Thus the only way uncertainty in EMCAL performance can affect the results is through modification of jet momentum or axis.

Uncertainty related to the EMCAL energy scale was estimated by scaling cluster energies up and down by 2 % in a PYTHIA particle level simulation. Similarly the jet momentum was scaled by $\pm 2\%$ when determining the jet p_T bin. In this analysis EMCAL is used only in jet reconstruction, not for calculating j_T . The only ways EMCAL uncertainty can affect the analysis are changes in jet energy and jet axis. Jet axis shouldn't significantly change, so the main contribution should be changes in jet p_T bin.

The resulting differences in the inclusive j_T distributions are shown in Figure 56. Qualitatively the effect of scaling cluster energies is the same as scaling the jet energies.

Like in the previous cases fits are performed for the unscaled case and for cases with $\pm 2\%$ scaling. The resulting systematic uncertainties are shown in Figure 57. The uncertainty is taken to be 1% for both components.

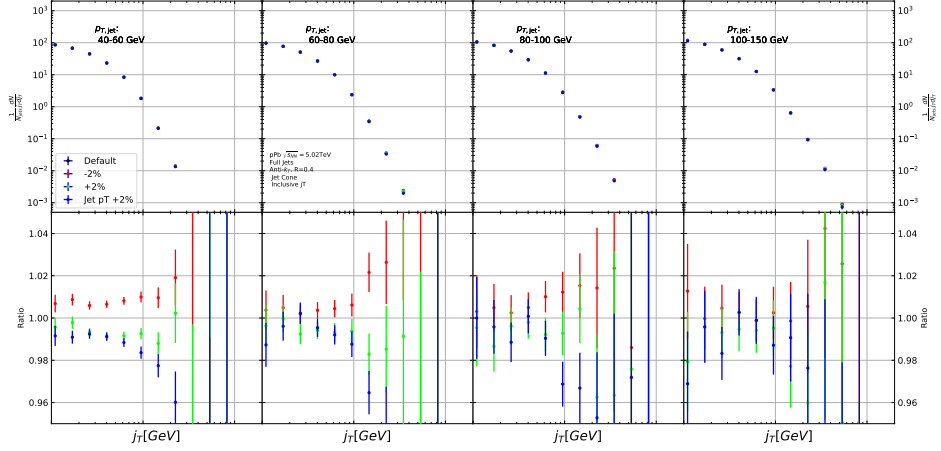


Figure 56: Results from PYTHIA simulations with Cluster energies scaled up and down by 2 %. Additionally jet momenta were scaled by 2 % when determining the jet p_T bin.

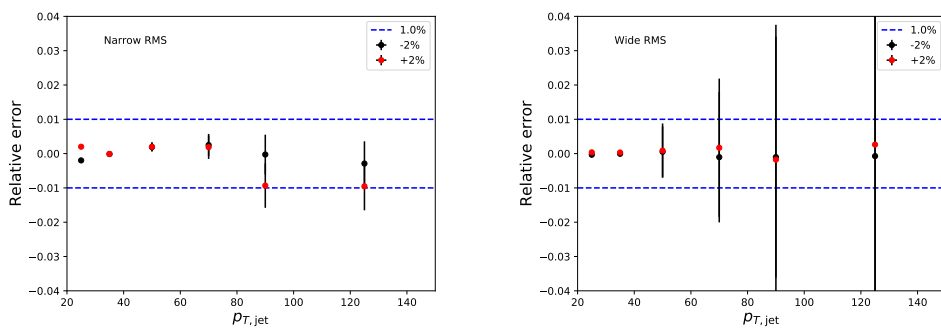


Figure 57: Relative systematic uncertainties resulting from cluster energy uncertainty.

5.5 Summary of systematic uncertainties

The different source of the systematic uncertainty are considered as uncorrelated and the values of each source are summed in quadrature. Resulting systematic uncertainties are shown in Table 4. The different source of the systematic uncertainty are considered to be uncorrelated and are thus combined bin-by-bin in quadrature to get the total systematic uncertainties. The resulting uncertainty is approximately 10 % for the wide component RMS and 13 % for the narrow component RMS.

Table 4: Summary of systematic uncertainties

Systematic	Wide RMS	Narrow RMS
Background	5 %	9 %
Unfolding	8 %	8 %
Tracking	4 %	5 %
EMCal	1 %	1 %
Total	10 %	13%

6 Results

In this section I present the final results for j_T signals. After unfolding and subtracting the background contribution we get the final j_T distributions. Figure 58 shows j_T distributions for two different $p_{T,jet}$ bins with $60 \text{ GeV} < p_{T,jet} < 80 \text{ GeV}$ and $100 \text{ GeV} < p_{T,jet} < 150 \text{ GeV}$. The distributions get wider with increasing $p_{T,jet}$. In part this is explained by kinematics; In a jet cone the cone size sets limits on the possible j_T values. For a given $p_{T,track}$ the maximum j_T value is approximately

$$j_{T\max} \approx R \cdot p_{T,track}, \quad (71)$$

using the small angle approximation.

We fit the distribution using the two component fit function presented in Section 4.5. These are also shown in Figure 58. Fitting a Gaussian alone to the entire j_T distribution will produce a similar result as the Gaussian component in the two component fit. Thus the gaussian fit alone can't describe the full jet j_T distribution.

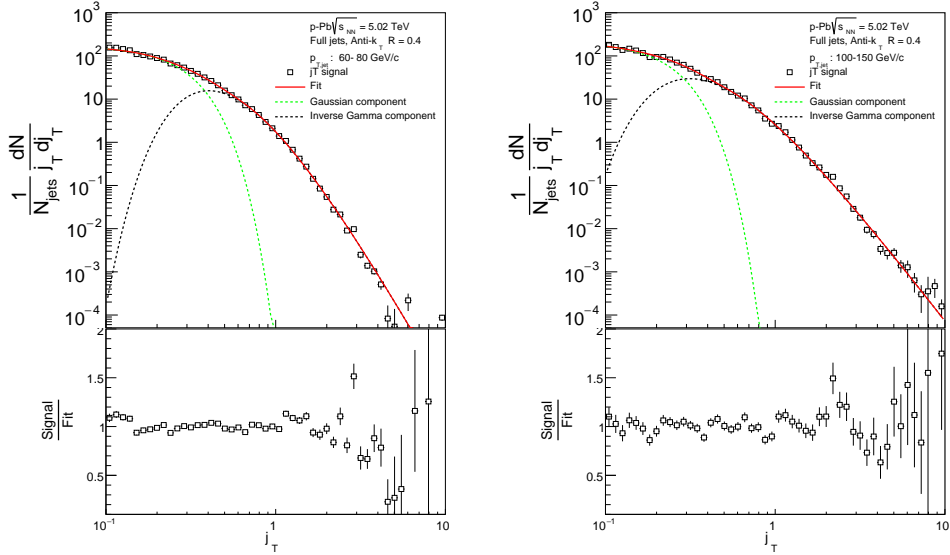


Figure 58: j_T signal distributions fitted with the two component model are shown in different jet p_T bins.

To characterise the widening of the j_T distribution we can then extract the RMS, i.e. $\sqrt{\langle j_T^2 \rangle}$, values of the fits. Resulting RMS values with systematic errors are shown separately for the two components in Figure 59. Here it is seen that the width of the narrow component shows only a weak dependence on the transverse

momentum of the jet, $p_{\text{T,jet}}$. The RMS value of the wide component on the other hand increases with increasing $p_{\text{T,jet}}$.

The RMS values for both components are compared to PYTHIA and Herwig simulations as shown in Figure 60. All the PYTHIA models reproduce the data well, both the wide and narrow component. For the narrow component Herwig gives RMS values comparable to the data. On the other hand, Herwig produces larger wide component $\sqrt{\langle j_{\text{T}}^2 \rangle}$ values than data and PYTHIA, and this difference seems to get larger with increasing $p_{\text{T,jet}}$.

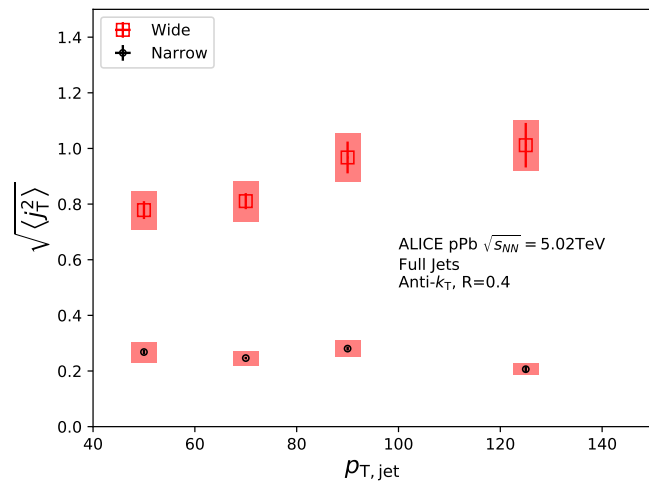


Figure 59: RMS values extracted from the fits are shown for the Gaussian (narrow) and inverse gamma (wide) components.

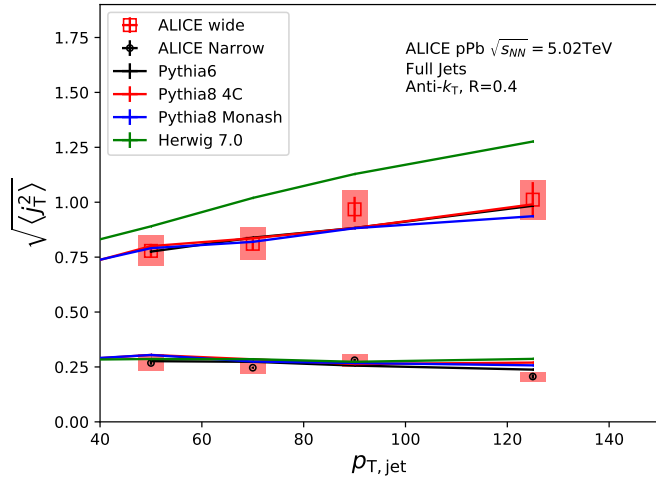


Figure 60: RMS values extracted from the fits are compared to Monte Carlo models. PYTHIA reproduces the data well for both the narrow and wide components. Herwig produces wider distributions.

6.1 High multiplicity events

The analysis was repeated taking only events with high multiplicity. Three different multiplicity percentile cuts were used; 10 %, 1 % and 0.1 %. The centrality estimations were given by V0A. Resulting j_T signal distributions are shown in Figure 61. From the figure one can observe no modification within the errors when tighter multiplicity cuts are introduced.

As described in Section 1.5 no conclusive evidence of jet modification in p–Pb collisions has been observed. However, all previous observations have been done for minimum bias events. Most observables are based on measuring yield instead of jet shape and are thus sensitive to biases in the centrality selection. No previous jet shape measurements have been performed in high multiplicity p–Pb events, where collective motion was observed.

As the statistics are limited in the high multiplicity runs, it was hard to achieve stable fits to the distributions. Thus the RMS values are not shown.

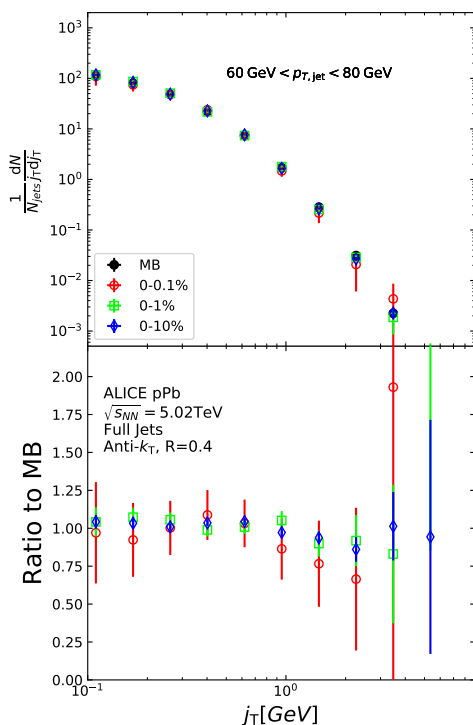


Figure 61: j_T distributions are shown for various multiplicity bins in p–Pb collisions.

7 Discussion

7.1 Comparing dihadron and jet j_T results

The jet fragmentation transverse momentum j_T has been studied previously at ALICE using dihadron correlations [277]. The study took the leading hadron in each event and calculated j_T for any near-side tracks with respect to the leading hadron. Thus there is no kinematical limit to j_T from the jet cone. In the analysis the background shape is estimated using pairs with large $\Delta\eta$. The normalisation of the background is done when fitting the j_T distribution. The inclusive distribution is fitted with a three component function, where one of the components is the background contribution. After subtracting the background, what remains is the signal distribution characterised by the two components. The resulting signal distribution from the analysis is shown in Figure 62. The analysis was the first to introduce this factorisation of j_T into components.

To constrain the effects from kinematical differences between $p_{T,\text{trigger}}$ bins the analysis used bins of the fragmentation variable x_{\parallel} , which is the projection of the associated particle momentum to the trigger particle normalised by the trigger particle momentum

$$x_{\parallel} = \frac{\vec{p}_t \cdot \vec{p}_a}{\vec{p}_t^2}. \quad (72)$$

The RMS results from the fitting in both pp and p–Pb collisions are shown in Figure 63. Qualitatively the results are similar to jet j_T results. The RMS value of the wide component has an increasing trend with respect to $p_{T,\text{t}}/p_{T,\text{jet}}$, while the RMS value of the narrow component stays constant. Both components are well described by PYTHIA simulations. As seen in the figures there is no difference between minimum bias pp and p–Pb results in the dihadron analysis.

Comparison between RMS values in dihadron j_T [277] and jet j_T is shown in Figure 64. The dihadron trigger p_T bins are converted to jet p_T bins and vice versa. Bin-by-bin comparison is still not possible, but general features can be identified.

The trends are similar in dihadron and jet j_T results. Wide component RMS values tend to increase with increasing $p_{T,\text{trigger}}/p_{T,\text{jet}}$. For $x_{\parallel} < 0.4$ Narrow component RMS increases slightly at low $p_{T,\text{trigger}}$ in dihadron analysis. This trend changes between x_{\parallel} bins; In larger x_{\parallel} bins the narrow component RMS is closer to constant as is the case for jet j_T .

The most striking difference is that dihadron j_T gives wider distributions with larger RMS values. There are several possible causes for this difference. First, in jet analysis the cone size limits width and thus the RMS values. The effect of this limitation can be studied by changing the cone size as is described in Section 7.1.1.

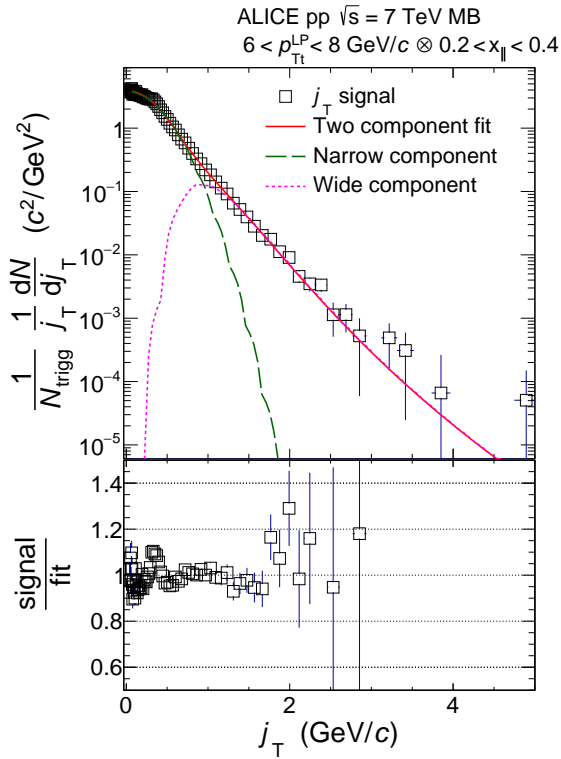


Figure 62: Measured j_T signal distribution using dihadron correlations is shown for $6 < p_{Tt} < 8$ and $0.2 < x_{||} < 0.4$. The distribution is fitted with the same two component model used in this thesis.

Second, the leading track is an imperfect estimate of the jet/original parton. Because the leading track in general is at an angle compared to the jet axis, the resulting j_T values are different. In practice the jet axis found by the jet finding algorithm tends to minimize the average j_T of jet constituents. Thus the yield at high j_T is limited and the RMS values are smaller. The effect of having the leading hadron as reference instead of the jet axis is discussed in Section 7.1.2

Third, the results from the dihadron analysis are done in $p_{T,\text{trigger}}$ bins. This favours hard jets, i.e. jets where the leading hadron carries a large momentum fraction and the jet multiplicity is small. In $p_{T,\text{jet}}$ bins jets are more likely to be soft, i.e. they have a small leading momentum fraction and high multiplicity jets.

7.1.1 Different R parameters

The size of the jet cone gives a limit for j_T . For a track with a fixed momentum p this is a hard limit. This is conveniently seen as $j_{T,\text{max}}$ can be given in terms of cone size R and momentum p . In the small angle approximation limit

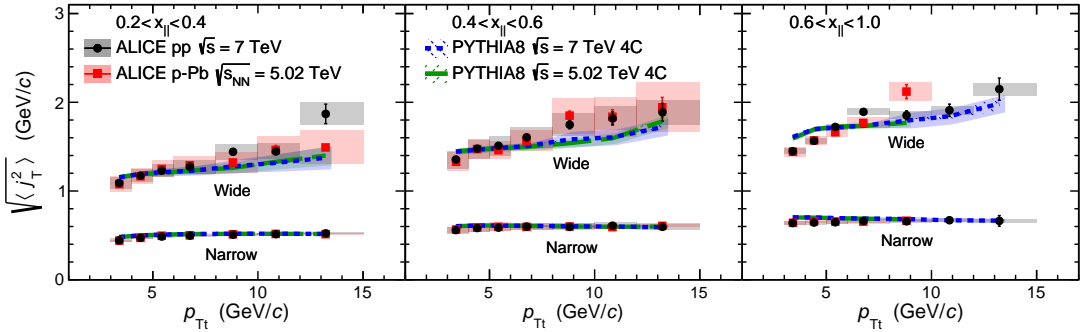


Figure 63: RMS values of the narrow and wide j_T components in the dihadron correlation analysis. Results from pp collisions at $\sqrt{s} = 7$ TeV (circular symbols) and from p–Pb collisions at $\sqrt{s_{NN}} = 5.02$ TeV (square symbols) are compared to PYTHIA 8 tune 4C simulations at $\sqrt{s} = 7$ TeV (short dashed line) and at $\sqrt{s} = 5.02$ TeV (long dashed line). Different panels correspond to different x_{\parallel} bins with $0.2 < x_{\parallel} < 0.4$ on the left, $0.4 < x_{\parallel} < 0.6$ in the middle, and $0.6 < x_{\parallel} < 1.0$ on the right. The statistical errors are represented by bars and the systematic errors by boxes. [277]

$$j_{T,\max} \approx p \cdot R. \quad (73)$$

Thus for tracks with $p_{T,\text{track}} < p_{T0}$, must be $j_T < p_{T0} \cdot R$. This is illustrated in Figure 65.

We studied the effect of cone sizes on j_T distribution with a PYTHIA simulation. Distributions with different cone sizes in different $p_{T,\text{jet}}$ bins are shown in Figure 66. The increase of high j_T with increasing cone size, R , is clearly seen in the individual j_T distributions. At low j_T there is no change within the errors.

When looking at the RMS values from wide component we see an increase or decrease of about 10% when going from $R = 0.4$ to $R = 0.5$ or $R = 0.3$, respectively. This is seen in Figure 67. The message from narrow component RMS values is less clear. At low jet p_T the behaviour is similar, but at high p_T the order is reversed.

7.1.2 Leading tracks versus jet

In comparison to the leading hadron the jet axis from jet reconstruction should provide a better estimate of the original parton. The assumption is that because the leading hadron is an imperfect estimate of the jet axis, low j_T tracks should on average be shifted to higher j_T .

Because the leading track is at an angle compared to the jet axis, the resulting j_T values are different. In practice the jet axis found by the jet finding algorithm

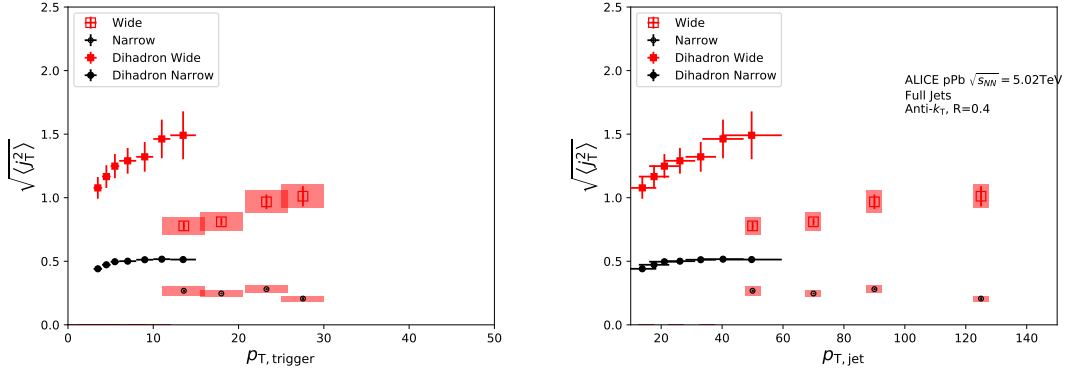


Figure 64: Jet j_T results are compared to results obtained in the dihadron analysis. Dihadron trigger p_T bins are converted to jet p_T bins using observed mean $p_{T,\text{jet}}$ values in $p_{T,\text{trigger}}$ bins. Dihadron results are for $0.2 < x_{||} < 0.4$

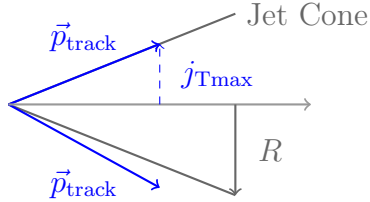


Figure 65: j_T has maximum value defined by the cone size and track momentum \vec{p}_{track}

tends to minimise the average j_T of jet constituents, as at least the hardest constituents should be close to the jet axis. Thus the yield at high j_T is reduced and the RMS values get smaller. On the other hand, when using the leading hadron as a reference, it is naturally missing from the set of tracks for which j_T is calculated. This causes a decrease in the yield at low j_T .

We performed a PYTHIA study where j_T was calculated with respect to the leading track momentum, instead of the jet axis. The results are shown in Figure 68. The resulting j_T distributions are significantly wider than j_T distributions from using the jet axis as reference. The effect seems to be larger than that seen in comparing different R values.

A direct comparison between jet and dihadron j_T measurements is not possible. But combined with the R dependence of $\sqrt{\langle j_T^2 \rangle}$ the difference between $\sqrt{\langle j_T^2 \rangle}$ values in jet and dihadron analyses can be quantitatively understood.

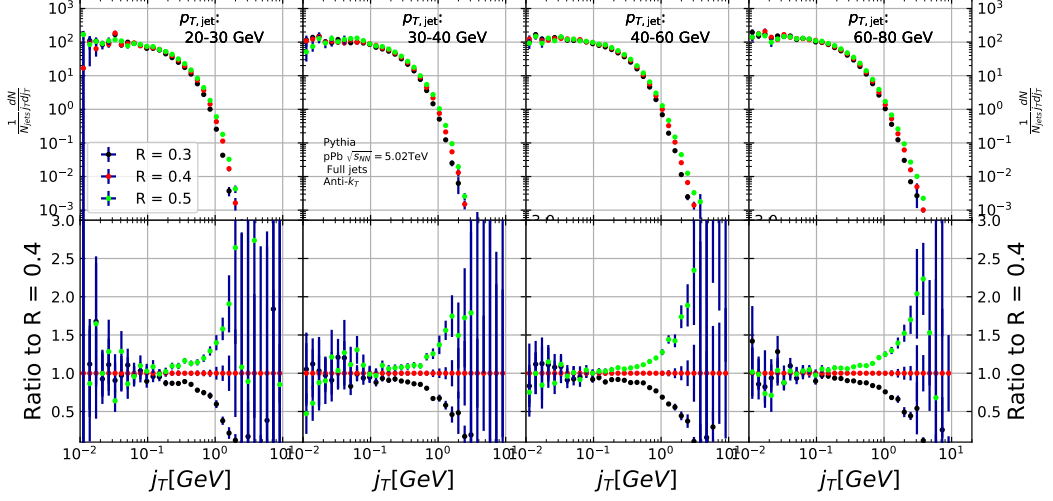


Figure 66: Effect of changing cone size on j_T distributions. The change is done both for the R parameter in the anti- k_T algorithm, and for the size of the cone where j_T is calculated.

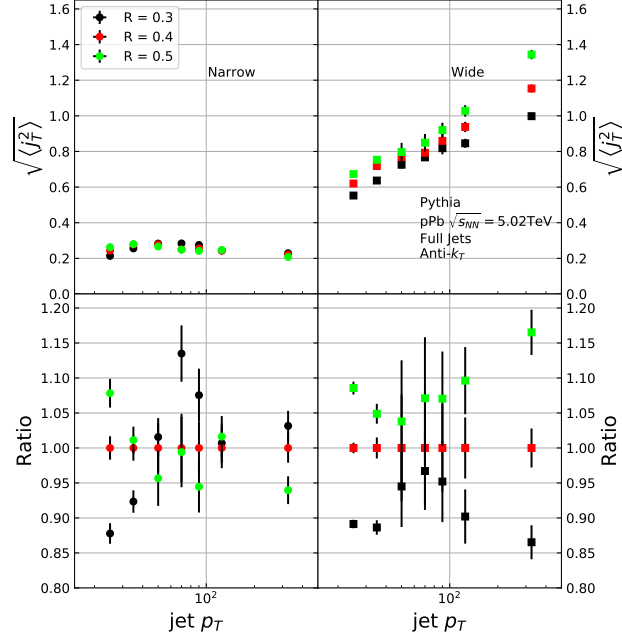


Figure 67: Effect of changing R parameter in jet finding on narrow and wide component RMS values. Wide component RMS values increase with increasing cone size.

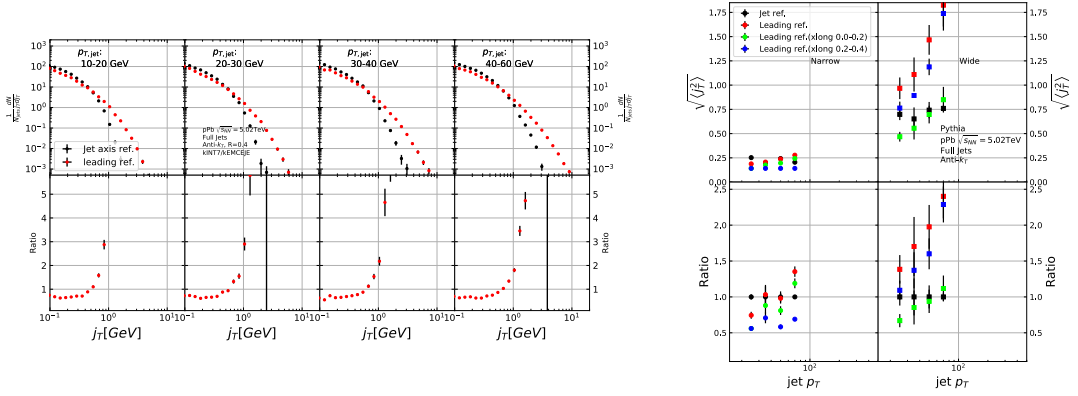


Figure 68: Results of calculating j_T with respect to the leading hadron, instead of the jet axis in a PYTHIA simulation are shown.

8 Summary

In this thesis I have studied the jet fragmentation transverse momentum at $\sqrt{s_{NN}} = 5.02$ TeV in p–Pb collisions. The analysis was performed using jets reconstructed with the anti- k_T algorithm. The resulting j_T distributions were fitted with a two component model, which allows us to separate two distinct components. The width of the narrow component was found to depend weakly on jet p_T . The narrow component has been associated with the non-perturbative hadronisation process. This is consistent with the assumption that hadronisation is universal, i.e. it doesn't depend on the hard scattering.

The width of the wide component was found to get larger with increasing $p_{T,jet}$. This is in part explained by the changing kinematical limits when going to higher $p_{T,jet}$ which allows higher $p_{T,track}$. Additionally the larger phase space allows stronger parton splitting.

Both the narrow and wide component RMS values were well described by PYTHIA , but Herwig gave larger RMS values for the wide component than data. In the narrow component there was no difference between the models. Both describe the data well. This component was associated with hadronisation. At least in this context the different hadronisation algorithms of PYTHIA (string model) and Herwig (cluster model) give similar results.

Similar analysis has been performed with dihadron correlations [277]. Although a direct comparison between the results is not possible, they are qualitatively compatible with each other. The difference is understood to come from the different j_T reference, the cone size limitation in jet j_T analysis and the kinematical bias that arises from using $p_{T,\text{trigger}}$ bins which favours harder jets than using $p_{T,\text{jet}}$ bins. The dihadron analysis saw no difference between results in pp and p–Pb datasets and concluded that there were no cold nuclear matter effects. The same is expected to be true for the jet j_T . This is further supported by the agreement between PYTHIA and data as PYTHIA results are for pp collisions.

To study possible QGP effects in high multiplicity p–Pb collisions the analysis was repeated using different multiplicity selections. So far no jet observables have shown conclusive evidence of modification in p–Pb events. However these are primarily based on measuring yield, which makes them vulnerable to biases when selecting for multiplicity. Thus these measurements have been only performed in minimum bias events. As j_T is based on shape on a per-jet basis, it should not be sensitive to these selection biases. No effect was seen in any of the multiplicity selections. However, with the statistics available, the effect should be quite large ($\gtrsim 20\%$) to be visible.

Naturally the next step would be extending the analysis to Pb–Pb data to gain better understanding of jet modification. Jet analysis in a heavy-ion collision with significant contributions from the underlying event has proved challenging [6]. However, experimental methods have improved in recent years. For the j_T analysis presented in this thesis the main challenge would be the background subtraction method. Because of anisotropic flow in heavy ion collisions the background inside the jet cone and a cone perpendicular to it would be different. It's unclear if the perpendicular cone method can be modified or if a completely new approach is required.

It has been shown that in Pb–Pb collisions jets become softer and wider because of medium-induced radiation [6]. On the other hand, the hot medium suppresses gluon jets more than quark jets. This has the opposite effect, narrowing jets, as gluon jets are naturally wider than quark jets [278]. How these different effects combine in j_T needs to be studied.

References

- [1] D. J. Gross and F. Wilczek, Physical Review D **8**, 3633 (1973).
- [2] Particle Data Group, M. Tanabashi *et al.*, Phys. Rev. **D98**, 030001 (2018).
- [3] M. L. Perl, E. R. Lee, and D. Loomba, Mod. Phys. Lett. **A19**, 2595 (2004).
- [4] E. Shuryak, Phys. Reps. **61**, 71 (1980).
- [5] D. H. Perkins, *Introduction to high energy physics* (, 1982).
- [6] M. Connors, C. Nattrass, R. Reed, and S. Salur, Rev. Mod. Phys. **90**, 025005 (2018), 1705.01974.
- [7] J. L. Nagle and W. A. Zajc, Ann. Rev. Nucl. Part. Sci. **68**, 211 (2018), 1801.03477.
- [8] E. S., Monatshefte für Mathematik und Physik **26**, A38 (1915).
- [9] P. A. M. Dirac and N. H. D. Bohr, Proceedings of the Royal Society of London. Series A, Containing Papers of a Mathematical and Physical Character **114**, 243 (1927), <https://royalsocietypublishing.org/doi/pdf/10.1098/rspa.1927.0039>.
- [10] S. Tomonaga, Prog. Theor. Phys. **1**, 27 (1946).
- [11] J. S. Schwinger, Phys. Rev. **75**, 651 (1948), [,59(1948)].
- [12] J. S. Schwinger, Phys. Rev. **74**, 1439 (1948), [,36(1948)].
- [13] R. P. Feynman, Phys. Rev. **74**, 1430 (1948).
- [14] M. L. Krauss, *The Greatest Story Ever Told—So Far: Why Are We Here?* (, 2017).
- [15] S. L. Glashow, J. Iliopoulos, and L. Maiani, Phys. Rev. **D2**, 1285 (1970).
- [16] A. Salam and J. C. Ward, Phys. Lett. **13**, 168 (1964).
- [17] S. Weinberg, Phys. Rev. Lett. **19**, 1264 (1967).
- [18] G. P. S. Occhialini and C. F. Powell, (1987), [Nature159,186(1947)].
- [19] C. M. G. Lattes, G. P. S. Occhialini, and C. F. Powell, Nature **160**, 453 (1947), [,99(1947)].

- [20] R. Bjorklund, W. Crandall, B. J. Moyer, and H. York, Phys. Review **77**, 213 (1950).
- [21] O. Chamberlain, E. Segre, C. Wiegand, and T. Ypsilantis, Phys. Rev. **100**, 947 (1955).
- [22] B. Cork, G. R. Lambertson, O. Piccioni, and W. A. Wenzel, Phys. Rev. **104**, 1193 (1957).
- [23] L. W. Alvarez *et al.*, Phys. Rev. Lett. **2**, 215 (1959).
- [24] R. Armenteros, K. Barker, C. Butler, A. Cachon, and C. York, The London, Edinburgh, and Dublin Philosophical Magazine and Journal of Science **43**, 597 (1952), <https://doi.org/10.1080/14786440608520216>.
- [25] A. Bonetti, R. L. Setti, M. Panetti, and G. Tomasini, Il Nuovo Cimento (1943-1954) **10**, 1736 (1953).
- [26] R. Plano, N. Samios, M. Schwartz, and J. Steinberger, Il Nuovo Cimento (1955-1965) **5**, 216 (1957).
- [27] W. B. Fowler, R. P. Shutt, A. M. Thorndike, and W. L. Whittemore, Phys. Rev. **91**, 1287 (1953).
- [28] W. Heisenberg, Zeitschrift für Physik **77**, 1 (1932).
- [29] M. Gell-Mann, Phys. Rev. **125**, 1067 (1962).
- [30] V. E. Barnes *et al.*, Phys. Lett. **12**, 134 (1964).
- [31] M. Gell-Mann, Phys. Lett. **8**, 214 (1964).
- [32] G. Zweig, An SU(3) model for strong interaction symmetry and its breaking. Version 2, in *DEVELOPMENTS IN THE QUARK THEORY OF HADRONS. VOL. 1. 1964 - 1978*, edited by D. Lichtenberg and S. P. Rosen, pp. 22–101, 1964.
- [33] O. Greenberg, Phys. Rev. Lett. **13**, 598 (1964).
- [34] H. Fritzsch and M. Gell-Mann, eConf **C720906V2**, 135 (1972), hep-ph/0208010.
- [35] Crystal Ball Collaboration, D. Williams *et al.*, Phys. Rev. **D38**, 1365 (1988).
- [36] W. Krolikowski, Nuovo Cim. **A27**, 194 (1975).

- [37] E. D. Bloom *et al.*, Phys. Rev. Lett. **23**, 930 (1969).
- [38] M. Breidenbach *et al.*, Phys. Rev. Lett. **23**, 935 (1969).
- [39] The nobel prize in physics 1990, <https://www.nobelprize.org/prizes/physics/1990/summary/>, Accessed: Mon. 8 Apr 2019.
- [40] J. D. Bjorken, Phys. Rev. **179**, 1547 (1969).
- [41] J. D. Bjorken and E. A. Paschos, Phys. Rev. **185**, 1975 (1969).
- [42] R. P. Feynman, Phys. Rev. Lett. **23**, 1415 (1969), [,494(1969)].
- [43] D. J. Gross and F. Wilczek, Physical Review Letters **30**, 1343 (1973).
- [44] H. D. Politzer, Physical Review Letters **30**, 1346 (1973).
- [45] D. J. Gross and F. Wilczek, Physical Review D **9**, 980 (1974).
- [46] H. Georgi and H. D. Politzer, Physical Review D **9**, 416 (1974).
- [47] The nobel prize in physics 2004, <https://www.nobelprize.org/prizes/physics/2004/summary/>, Accessed: Mon. 8 Apr 2019.
- [48] H. Fritzsch, M. Gell-Mann, and H. Leutwyler, Physics Letters B **47**, 365 (1973).
- [49] SLAC-SP-017, J. E. Augustin *et al.*, Phys. Rev. Lett. **33**, 1406 (1974), [Adv. Exp. Phys.5,141(1976)].
- [50] E598, J. J. Aubert *et al.*, Phys. Rev. Lett. **33**, 1404 (1974).
- [51] C. Bacci *et al.*, Phys. Rev. Lett. **33**, 1408 (1974), [Erratum: Phys. Rev. Lett.33,1649(1974)].
- [52] The nobel prize in physics 1976, <https://www.nobelprize.org/prizes/physics/1976/summary/>, Accessed: Mon. 8 Apr 2019.
- [53] J. D. Bjorken and S. L. Glashow, Phys. Lett. **11**, 255 (1964).
- [54] I. Flegel and P. Söding, CERN courier (2004).
- [55] R. Brandelik *et al.*, Physics Letters B **86**, 243 (1979).
- [56] J. K. L. MacDonald, Phys. Rev. **43**, 830 (1933).
- [57] C. Berger *et al.*, Physics Letters B **86**, 418 (1979).

- [58] M. Kobayashi and T. Maskawa, Prog. Theor. Phys. **49**, 652 (1973).
- [59] The nobel prize in physics 2008, <https://www.nobelprize.org/prizes/physics/2008/summary/>, Accessed: Mon. 8 Apr 2019.
- [60] S. W. Herb *et al.*, Phys. Rev. Lett. **39**, 252 (1977).
- [61] CDF, F. Abe *et al.*, Phys. Rev. Lett. **74**, 2626 (1995), hep-ex/9503002.
- [62] D0, S. Abachi *et al.*, Phys. Rev. Lett. **74**, 2422 (1995), hep-ex/9411001.
- [63] J. Collins and M. Perry, Phys. rev. Lett. **34**, 1353 (1975).
- [64] K. Rajagopal, SLAC Beam Line **31-2**, 9 (2001).
- [65] P. Kovtun, D. Son, and A. Starinets, Phys.Rev.Lett. **94**, 111601 (2005), hep-th/0405231.
- [66] R. A. Lacey *et al.*, Phys. Rev. Lett. **98**, 092301 (2007).
- [67] E. Lofgren, *ACCELERATOR DIVISION ANNUAL REPORTS, 1 JULY 1972 12/31/1974* (, 1975).
- [68] D. S. Barton, Heavy ion program at bnl: Ags, rhic, in *Proc. 1987 Particle Accelerator Conference, Washington, D.C., March, 1987*, 1987.
- [69] I. Vitev and M. Gyulassy, Phys.Rev.Lett. **89**, 252301 (2002), hep-ph/0209161.
- [70] A. Kovalenko *et al.*, Status of the nuclotron, in *Proceedings of EPAC Vol. 94*, pp. 161–164, 1994.
- [71] New state of matter created at cern, <https://home.cern/news/press-release/cern/new-state-matter-created-cern>, Accessed: Sat. 6 Apr 2019.
- [72] NA61/SHINE, K. Grebieszkow, PoS **CPOD2013**, 004 (2013).
- [73] PHENIX Collaboration, K. Adcox *et al.*, Nucl.Phys. **A757**, 184 (2005), nucl-ex/0410003.
- [74] STAR Collaboration, J. Adams *et al.*, Nucl.Phys. **A757**, 102 (2005), nucl-ex/0501009.
- [75] BRAHMS Collaboration, I. Arsene *et al.*, Nucl.Phys. **A757**, 1 (2005), nucl-ex/0410020.
- [76] B. Back *et al.*, Nucl.Phys. **A757**, 28 (2005), nucl-ex/0410022.

- [77] LHCb, E. Maurice, Fixed-target physics at LHCb, in *5th Large Hadron Collider Physics Conference (LHCP 2017) Shanghai, China, May 15-20, 2017*, 2017, 1708.05184.
- [78] S. A. Voloshin, A. M. Poskanzer, and R. Snellings, (2008), 0809.2949.
- [79] S. A. Voloshin, A. M. Poskanzer, A. Tang, and G. Wang, Phys.Lett. **B659**, 537 (2008), 0708.0800.
- [80] H. Holopainen, H. Niemi, and K. J. Eskola, Phys.Rev. **C83**, 034901 (2011), 1007.0368.
- [81] ALICE Collaboration, Phys. Rev. C **88**, 044909 (2013).
- [82] M. L. Miller, K. Reygers, S. J. Sanders, and P. Steinberg, Ann.Rev.Nucl.Part.Sci. **57**, 205 (2007), nucl-ex/0701025.
- [83] R. Glauber, Lectures in theoretical physics, 1959.
- [84] A. Białłas, M. Błeszyński, and W. Czyż, Nuclear Physics B **111**, 461 (1976).
- [85] H. De Vries, C. W. De Jager, and C. De Vries, Atom. Data Nucl. Data Tabl. **36**, 495 (1987).
- [86] ALICE, B. Abelev *et al.*, Phys. Rev. **C88**, 044909 (2013), 1301.4361.
- [87] PHENIX Collaboration, S. Afanasiev *et al.*, Phys.Rev. **C80**, 054907 (2009), 0903.4886.
- [88] D. Kharzeev, E. Levin, and M. Nardi, Nucl. Phys. **A747**, 609 (2005), hep-ph/0408050.
- [89] W.-T. Deng, X.-N. Wang, and R. Xu, Phys. Rev. **C83**, 014915 (2011), 1008.1841.
- [90] TOTEM, G. Antchev *et al.*, Eur. Phys. J. **C79**, 103 (2019), 1712.06153.
- [91] B. Alver, M. Baker, C. Loizides, and P. Steinberg, (2008), 0805.4411.
- [92] P. Romatschke, Int.J.Mod.Phys. **E19**, 1 (2010), 0902.3663.
- [93] K. A. *et al.* [ALICE Collaboration], Phys. Rev. Lett **106** (2011), 032301.
- [94] J.-Y. Ollitrault, Phys. Rev. D **46**, 229 (1992).
- [95] J.-Y. Ollitrault, Phys.Rev. D **48**, 1132 (1993), hep-ph/9303247.

- [96] U. Heinz and P. Kolb, Nucl. Phys. **A702**, 269 (2002).
- [97] S. Voloshin and Y. Zhang, Z.Phys. **C70**, 665 (1996), hep-ph/9407282.
- [98] B. Alver and G. Roland, Phys.Rev. **C81**, 054905 (2010), 1003.0194.
- [99] A. Mocsy and P. Sorensen, (2010), 1008.3381.
- [100] A. P. Mishra, R. K. Mohapatra, P. Saumia, and A. M. Srivastava, Phys.Rev. **C77**, 064902 (2008), 0711.1323.
- [101] T. Abbott *et al.*, Phys. Rev. Lett. **70**, 1393 (1993).
- [102] B. Schenke, S. Jeon, and C. Gale, Phys.Lett. **B702**, 59 (2011), 1102.0575.
- [103] K. A. *et al.* [ALICE Collaboration], Phys. Rev. Lett. **107** (2011), 032301.
- [104] K. Aamodt *et al.*, Physics Letters B **708**, 249 (2012).
- [105] L. LD, Izv. Akad. Nauk Ser. Fiz. **17**, 51 (1953).
- [106] J. D. Bjorken, Phys. Rev. D **27**, 140 (1983).
- [107] G. Baym, B. L. Friman, J. P. Blaizot, M. Soyeur, and W. Czyz, Nucl. Phys. **A407**, 541 (1983).
- [108] H. von Gersdorff, L. McLerran, M. Kataja, and P. V. Ruuskanen, Phys. Rev. D **34**, 794 (1986).
- [109] H. Niemi, K. J. Eskola, and R. Paatelainen, Phys. Rev. **C93**, 024907 (2016), 1505.02677.
- [110] R. Paatelainen, K. J. Eskola, H. Holopainen, and K. Tuominen, Phys. Rev. **C87**, 044904 (2013), 1211.0461.
- [111] R. Paatelainen, K. J. Eskola, H. Niemi, and K. Tuominen, Phys. Lett. **B731**, 126 (2014), 1310.3105.
- [112] ALICE, J. Adam *et al.*, Phys. Rev. Lett. **117**, 182301 (2016), 1604.07663.
- [113] J. E. Bernhard, J. S. Moreland, S. A. Bass, J. Liu, and U. Heinz, Phys. Rev. C **94**, 024907 (2016).
- [114] ALICE, S. Acharya *et al.*, Phys. Rev. **C97**, 024906 (2018), 1709.01127.
- [115] ALICE, S. Acharya *et al.*, Phys. Lett. **B773**, 68 (2017), 1705.04377.

- [116] A. Metz and A. Vossen, Prog. Part. Nucl. Phys. **91**, 136 (2016), 1607.02521.
- [117] R. Placakyte, Parton Distribution Functions, in *Proceedings, 31st International Conference on Physics in collisions (PIC 2011): Vancouver, Canada, August 28-September 1, 2011*, 2011, 1111.5452.
- [118] V. N. Gribov and L. N. Lipatov, Sov. J. Nucl. Phys. **15**, 438 (1972), [Yad. Fiz.15,781(1972)].
- [119] G. Altarelli and G. Parisi, Nucl. Phys. **B126**, 298 (1977).
- [120] Y. L. Dokshitzer, Sov. Phys. JETP **46**, 641 (1977), [Zh. Eksp. Teor. Fiz.73,1216(1977)].
- [121] J. Pumplin *et al.*, JHEP **07**, 012 (2002), hep-ph/0201195.
- [122] ZEUS, H1, A. M. Cooper-Sarkar, PoS **EPS-HEP2011**, 320 (2011), 1112.2107.
- [123] J. Butterworth *et al.*, J. Phys. **G43**, 023001 (2016), 1510.03865.
- [124] T. Sjöstrand and P. Z. Skands, Eur. Phys. J. **C39**, 129 (2005), hep-ph/0408302.
- [125] T. Sjöstrand *et al.*, Comput. Phys. Commun. **191**, 159 (2015), 1410.3012.
- [126] M. Bahr *et al.*, Eur. Phys. J. **C58**, 639 (2008), 0803.0883.
- [127] A. Buckley *et al.*, Phys. Rept. **504**, 145 (2011), 1101.2599.
- [128] Y. L. Dokshitzer, V. A. Khoze, A. H. Müller, and S. I. Troian, *Basics of Perturbative QCD* (Editions Frontières, Gif-sur-Yvette, France, 1991).
- [129] Y. I. Azimov, Y. L. Dokshitzer, V. A. Khoze, and S. I. Trovan, Zeitschrift für Physik C Particles and Fields **27**, 65 (1985).
- [130] B. Andersson, G. Gustafson, G. Ingelman, and T. Sjöstrand, Physics Reports **97**, 31 (1983).
- [131] ALICE Collaboration, K. Aamodt *et al.*, Phys.Lett. **B696**, 30 (2011), 1012.1004.
- [132] WA98 Collaboration, M. Aggarwal *et al.*, Eur.Phys.J. **C23**, 225 (2002), nucl-ex/0108006.
- [133] D. G. d'Enterria, Phys.Lett. **B596**, 32 (2004), nucl-ex/0403055.

- [134] PHENIX Collaboration, A. Adare *et al.*, Phys.Rev.Lett. **101**, 232301 (2008), 0801.4020.
- [135] STAR Collaboration, J. Adams *et al.*, Phys.Rev.Lett. **91**, 172302 (2003), nucl-ex/0305015.
- [136] A. Dainese, C. Loizides, and G. Paic, Eur.Phys.J. **C38**, 461 (2005), hep-ph/0406201.
- [137] I. Vitev, J.Phys. **G30**, S791 (2004), hep-ph/0403089.
- [138] C. A. Salgado and U. A. Wiedemann, Phys.Rev. **D68**, 014008 (2003), hep-ph/0302184.
- [139] N. Armesto, A. Dainese, C. A. Salgado, and U. A. Wiedemann, Phys.Rev. **D71**, 054027 (2005), hep-ph/0501225.
- [140] T. Renk, H. Holopainen, R. Paatelainen, and K. J. Eskola, Phys.Rev. **C84**, 014906 (2011), 1103.5308.
- [141] CMS Collaboration, S. Chatrchyan *et al.*, Eur.Phys.J. **C72**, 1945 (2012), 1202.2554.
- [142] PHENIX, S. S. Adler *et al.*, Phys. Rev. **C76**, 034904 (2007), nucl-ex/0611007.
- [143] PHENIX, A. Adare *et al.*, Phys. Rev. **C88**, 064910 (2013), 1309.4437.
- [144] ALICE, B. Abelev *et al.*, Phys. Lett. **B719**, 18 (2013), 1205.5761.
- [145] CMS, S. Chatrchyan *et al.*, Phys. Rev. Lett. **109**, 022301 (2012), 1204.1850.
- [146] W. H. H. Bethe and, Proc.Roy.Soc.Lond. **A146** (1934).
- [147] L. D. Landau and I. Pomeranchuk, Dokl. Akad. Nauk Ser. Fiz. **92**, 535 (1953).
- [148] A. B. Migdal, Phys. Rev. **103**, 1811 (1956).
- [149] P. Bosted *et al.*, Quantum-mechanical suppression of bremsstrahlung*, 1993.
- [150] R. Baier, Y. L. Dokshitzer, A. H. Mueller, S. Peigne, and D. Schiff, Nucl. Phys. **B484**, 265 (1997), hep-ph/9608322.
- [151] A. Majumder and M. Van Leeuwen, Prog.Part.Nucl.Phys. **A66**, 41 (2011), 1002.2206.

- [152] F. Dominguez, C. Marquet, A. Mueller, B. Wu, and B.-W. Xiao, Nucl.Phys. **A811**, 197 (2008), 0803.3234.
- [153] M. Gyulassy, P. Levai, and I. Vitev, Nucl.Phys. **B571**, 197 (2000), hep-ph/9907461.
- [154] U. A. Wiedemann, Nucl.Phys. **B588**, 303 (2000), hep-ph/0005129.
- [155] P. B. Arnold, G. D. Moore, and L. G. Yaffe, JHEP **0112**, 009 (2001), hep-ph/0111107.
- [156] X.-N. Wang and X.-f. Guo, Nucl.Phys. **A696**, 788 (2001), hep-ph/0102230.
- [157] T. Sjostrand, S. Mrenna, and P. Z. Skands, Comput.Phys.Commun. **178**, 852 (2008), 0710.3820.
- [158] I. Lokhtin and A. Snigirev, Eur.Phys.J. **C45**, 211 (2006), hep-ph/0506189.
- [159] N. Armesto, L. Cunqueiro, and C. A. Salgado, Nucl.Phys. **A830**, 271C (2009), 0907.4706.
- [160] K. Zapp, G. Ingelman, J. Rathsman, J. Stachel, and U. A. Wiedemann, Eur.Phys.J. **C60**, 617 (2009), 0804.3568.
- [161] T. Renk, Phys.Rev. **C79**, 054906 (2009), 0901.2818.
- [162] ALICE, J. Adam *et al.*, Phys. Lett. **B746**, 1 (2015), 1502.01689.
- [163] ATLAS, G. Aad *et al.*, Phys. Rev. Lett. **114**, 072302 (2015), 1411.2357.
- [164] CMS, V. Khachatryan *et al.*, Phys. Rev. **C96**, 015202 (2017), 1609.05383.
- [165] STAR, L. Adamczyk *et al.*, Phys. Rev. Lett. **112**, 122301 (2014), 1302.6184.
- [166] CMS, V. Khachatryan *et al.*, JHEP **02**, 156 (2016), 1601.00079.
- [167] A. Kurkela and U. A. Wiedemann, Phys. Lett. **B740**, 172 (2015), 1407.0293.
- [168] JETSCAPE, Y. Tachibana *et al.*, Jet substructure modification in a QGP from a multi-scale description of jet evolution with JETSCAPE, 2018, 1812.06366.
- [169] P. Aurenche and B. G. Zakharov, Eur. Phys. J. **C71**, 1829 (2011), 1109.6819.
- [170] A. Beraudo, J. G. Milhano, and U. A. Wiedemann, Phys. Rev. **C85**, 031901 (2012), 1109.5025.

- [171] A. Beraudo, J. G. Milhano, and U. A. Wiedemann, JHEP **07**, 144 (2012), 1204.4342.
- [172] J. Casalderrey-Solana, Y. Mehtar-Tani, C. A. Salgado, and K. Tywoniuk, Phys. Lett. **B725**, 357 (2013), 1210.7765.
- [173] F. D'Eramo, M. Lekaveckas, H. Liu, and K. Rajagopal, JHEP **05**, 031 (2013), 1211.1922.
- [174] A. Ayala, I. Dominguez, J. Jalilian-Marian, and M. E. Tejeda-Yeomans, Phys. Rev. **C94**, 024913 (2016), 1603.09296.
- [175] G. Moliere, Z. Naturforsch. **A2**, 133 (1947).
- [176] CMS, S. Chatrchyan *et al.*, Phys. Rev. **C84**, 024906 (2011), 1102.1957.
- [177] C. Aidala *et al.*, Phys. Rev. **C95**, 034910 (2017), 1609.02894.
- [178] PHENIX, S. S. Adler *et al.*, Phys. Rev. Lett. **91**, 072303 (2003), nucl-ex/0306021.
- [179] BRAHMS, I. Arsene *et al.*, Phys. Rev. Lett. **91**, 072305 (2003), nucl-ex/0307003.
- [180] PHOBOS, B. B. Back *et al.*, Phys. Rev. Lett. **91**, 072302 (2003), nucl-ex/0306025.
- [181] STAR, J. Adams *et al.*, Phys. Rev. Lett. **91**, 072304 (2003), nucl-ex/0306024.
- [182] PHENIX, A. Adare *et al.*, Phys. Rev. Lett. **115**, 142301 (2015), 1507.06273.
- [183] E735, T. Alexopoulos *et al.*, Phys. Rev. **D48**, 984 (1993).
- [184] MiniMax, T. C. Brooks *et al.*, Phys. Rev. **D61**, 032003 (2000), hep-ex/9906026.
- [185] C. Shen, Z. Qiu, and U. Heinz, Phys. Rev. **C92**, 014901 (2015), 1502.04636.
- [186] PHENIX, A. Adare *et al.*, Phys. Rev. **C94**, 064901 (2016), 1509.07758.
- [187] CMS, V. Khachatryan *et al.*, JHEP **09**, 091 (2010), 1009.4122.
- [188] C. A. Salgado and J. P. Wessels, Ann. Rev. Nucl. Part. Sci. **66**, 449 (2016).
- [189] ATLAS, G. Aad *et al.*, Phys. Rev. Lett. **116**, 172301 (2016), 1509.04776.
- [190] ALICE, S. Acharya *et al.*, JHEP **09**, 032 (2017), 1707.05690.

- [191] C. Shen, J.-F. Paquet, G. S. Denicol, S. Jeon, and C. Gale, Phys. Rev. **C95**, 014906 (2017), 1609.02590.
- [192] H. Niemi and G. S. Denicol, (2014), 1404.7327.
- [193] PHENIX, C. Aidala *et al.*, Nature Phys. **15**, 214 (2019), 1805.02973.
- [194] CMS, C. Collaboration, (2018).
- [195] CMS, V. Khachatryan *et al.*, JHEP **04**, 039 (2017), 1611.01664.
- [196] ATLAS, G. Aad *et al.*, Phys. Rev. **C90**, 044906 (2014), 1409.1792.
- [197] X. Zhang and J. Liao, (2013), 1311.5463.
- [198] C. Park, C. Shen, S. Jeon, and C. Gale, Nucl. Part. Phys. Proc. **289-290**, 289 (2017), 1612.06754.
- [199] K. Tywoniuk, Nucl. Phys. **A926**, 85 (2014).
- [200] CMS, A. M. Sirunyan *et al.*, Phys. Lett. **B776**, 195 (2018), 1702.00630.
- [201] ALICE, J. Adam *et al.*, Phys. Rev. **C91**, 064905 (2015), 1412.6828.
- [202] F. Sikler, (2003), hep-ph/0304065.
- [203] Cern, <https://home.cern/>, Accessed: Wed. 17 Apr 2019.
- [204] 2019.
- [205] P. M. Watkins, Contemp. Phys. **27**, 291 (1986).
- [206] NA61/SHINE, A. Laszlo, Nucl. Phys. **A830**, 559C (2009), 0907.4493.
- [207] NA62 Collaboration, F. Hahn *et al.*, CERN Report No. NA62-10-07, 2010 (unpublished).
- [208] NA63 Collaboration, R. Mikkelsen, U. Uggerhoj, and T. Wistisen, CERN Report No. CERN-SPSC-2014-033. SPSC-SR-146, 2014 (unpublished).
- [209] AWAKE, S. Döbert, p. TH1A04. 5 p (2018).
- [210] R. Losito, E. Laface, and W. Scandale, p. 3 p (2009).
- [211] DIRAC, C. P. Schuetz, The Dirac experiment at CERN, in *Proceedings, 38th Rencontres de Moriond on QCD and High-Energy Hadronic Interactions: Les Arcs, France, March 22-29, 2003*, 2003, hep-ph/0305121.

- [212] E. M. Dunne *et al.*, Science **354**, 1119 (2016), <https://science.sciencemag.org/content/354/6316/1119.full.pdf>.
- [213] n_TOF, P. M. Milazzo *et al.*, AIP Conf. Proc. **1109**, 84 (2009).
- [214] Cern experiments, 2019.
- [215] O. S. Brüning *et al.*, *LHC Design Report*CERN Yellow Reports: Monographs (CERN, Geneva, 2004).
- [216] L. Evans and P. Bryant, JINST **3**, S08001 (2008).
- [217] ALICE, K. Aamodt *et al.*, JINST **3**, S08002 (2008).
- [218] ATLAS, G. Aad *et al.*, JINST **3**, S08003 (2008).
- [219] CMS, S. Chatrchyan *et al.*, JINST **3**, S08004 (2008).
- [220] LHCb, A. A. Alves, Jr. *et al.*, JINST **3**, S08005 (2008).
- [221] LHCf, O. Adriani *et al.*, JINST **3**, S08006 (2008).
- [222] TOTEM, G. Anelli *et al.*, JINST **3**, S08007 (2008).
- [223] MoEDAL, B. Acharya *et al.*, JHEP **08**, 067 (2016), 1604.06645.
- [224] ATLAS, G. Aad *et al.*, Phys. Lett. **B716**, 1 (2012), 1207.7214.
- [225] CMS, S. Chatrchyan *et al.*, Phys. Lett. **B716**, 30 (2012), 1207.7235.
- [226] T. ALICE Collaboration *et al.*, Journal of Instrumentation **3**, S08002 (2008).
- [227] ALICE, K. Aamodt *et al.*, Phys. Rev. Lett. **105**, 252301 (2010), 1011.3916.
- [228] ALICE, G. Dellacasa *et al.*, (2000).
- [229] ALICE, G. Dellacasa *et al.*, (1999).
- [230] ALICE, I. Belikov, EPJ Web Conf. **125**, 01004 (2016), 1607.01171.
- [231] J. Alme *et al.*, Nucl. Instrum. Meth. **A622**, 316 (2010), 1001.1950.
- [232] for the ALICE, C. Zampolli, Particle Identification with the ALICE detector at the LHC, in *Proceedings, PLHC2012: Physics at the LHC 2012 (PLHC2012): Vancouver, BC, Canada, June 4-9, 2012*, 2012, 1209.5637.

- [233] ALICE Collaboration, P. Cortese, *ALICE transition-radiation detector: Technical Design Report*Technical Design Report ALICE (CERN, Geneva, 2001).
- [234] ALICE, G. Dellacasa *et al.*, (2000).
- [235] ALICE, S. Beole *et al.*, (1998).
- [236] ALICE, B. Abelev *et al.*, Phys. Lett. **B717**, 162 (2012), 1205.5724.
- [237] ALICE, J. Adam *et al.*, Phys. Lett. **B754**, 235 (2016), 1509.07324.
- [238] ALICE, R. Reed, J. Phys. Conf. Ser. **446**, 012006 (2013), 1304.5945.
- [239] ALICE, G. Dellacasa *et al.*, (1999).
- [240] ALICE, P. Cortese *et al.*, (2008).
- [241] J. Allen *et al.*, Report No. CERN-LHCC-2010-011. ALICE-TDR-14-add-1, 2010 (unpublished).
- [242] ALICE, P. Cortese *et al.*, (2004).
- [243] ALICE, A. I. Maevskaya, (2018), 1812.00594.
- [244] ALICE Collaboration, *ALICE Photon Multiplicity Detector (PMD): Technical Design Report*Technical Design Report ALICE (CERN, Geneva, 1999).
- [245] ACORDE, A. Fernández *et al.*, Nucl. Instrum. Meth. **A572**, 102 (2007), physics/0606051.
- [246] ALICE, G. Dellacasa *et al.*, (1999).
- [247] A. Villatoro Tello, AIP Conference Proceedings **1819** (2017).
- [248] ALICE, S. Beole *et al.*, (1996).
- [249] ALICE, M. Krivda *et al.*, JINST **11**, C03051 (2016).
- [250] J. Král, *Intrinsic transverse momentum distribution of jet constituents in p-Pb collisions at ALICE*, PhD thesis, University of Jyväskylä, 2014.
- [251] J. Kral, T. Awes, H. Muller, J. Rak, and J. Schambach, Nuclear Instruments and Methods in Physics Research Section A: Accelerators, Spectrometers, Detectors and Associated Equipment **693**, 261 (2012).

- [252] ALICE Collaboration, B. Abelev *et al.*, CERN Report No. CERN-LHCC-2012-012. LHCC-I-022. ALICE-UG-002, 2012 (unpublished).
- [253] A. Maevskaya, EPJ Web Conf. **204**, 11003 (2019).
- [254] Report No. CERN-LHCC-2015-001. ALICE-TDR-018, 2015 (unpublished).
- [255] F. Sauli, L. Ropelewski, and P. Everaerts, Nucl. Instrum. Meth. **A560**, 269 (2006).
- [256] ALICE TPC, M. Ball, K. Eckstein, and T. Gunji, JINST **9**, C04025 (2014).
- [257] The ALICE Collaboration, Report No. CERN-LHCC-2013-020. ALICE-TDR-016, 2013 (unpublished).
- [258] P. F. Little, *Secondary Effects* (Springer Berlin Heidelberg, Berlin, Heidelberg, 1956), pp. 574–662.
- [259] M. Vargyas, *Jet shape modification in Pb-Pb collisions at $\sqrt{s_{NN}} = 2.76 \text{ TeV}$ using two-particle correlations*, PhD thesis, University of Jyväskylä, 2018.
- [260] ALICE TPC upgrade, J. E. Brücke and T. E. Hildén, The GEM QA Protocol of the ALICE TPC Upgrade Project, in *5th International Conference on Micro Pattern Gas Detectors (MPGD2017) Temple University, Philadelphia, USA, May 22-26, 2017*, 2018, 1811.07043.
- [261] T. Hildén *et al.*, Nucl. Instrum. Meth. **A770**, 113 (2015), 1704.06691.
- [262] ALICE, B. B. Abelev *et al.*, Int. J. Mod. Phys. **A29**, 1430044 (2014), 1402.4476.
- [263] ALICE, K. Aamodt *et al.*, JINST **5**, P03003 (2010), 1001.0502.
- [264] R. Fruhwirth, Nucl. Instrum. Meth. **A262**, 444 (1987).
- [265] A. Maire, Track reconstruction principle in ALICE for LHC run I and run II. Principes de reconstruction de traces dans ALICE pour les runs I et II du LHC, General Photo, 2011.
- [266] ALICE, B. Abelev *et al.*, JHEP **03**, 053 (2012), 1201.2423.
- [267] ALICE, B. Abelev *et al.*, Phys. Lett. **B719**, 29 (2013), 1212.2001.
- [268] M. Cacciari, G. P. Salam, and G. Soyez, Eur. Phys. J. **C72**, 1896 (2012), 1111.6097.

- [269] M. Cacciari, G. P. Salam, and G. Soyez, JHEP **04**, 063 (2008), 0802.1189.
- [270] T. Sjöstrand, S. Mrenna, and P. Z. Skands, Comput. Phys. Commun. **178**, 852 (2008), 0710.3820.
- [271] G. Upton and I. Cook, *A Dictionary of Statistics* (, 2008).
- [272] Roounfold: Root unfolding framework, <http://hepunx.rl.ac.uk/~adye/software/unfold/RooUnfold.html>, 2013.
- [273] A. Hocker and V. Kartvelishvili, Nucl. Instrum. Meth. **A372**, 469 (1996), hep-ph/9509307.
- [274] P. Z. Skands, Phys. Rev. **D82**, 074018 (2010), 1005.3457.
- [275] R. Brun, R. Hagelberg, M. Hansroul, and J. C. Lassalle, *Simulation program for particle physics experiments, GEANT: user guide and reference manual* (CERN, Geneva, 1978).
- [276] R. Brun *et al.*, (1994).
- [277] ALICE, S. Acharya *et al.*, JHEP **03**, 169 (2019), 1811.09742.
- [278] Y.-T. Chien and I. Vitev, JHEP **05**, 023 (2016), 1509.07257.